Molecular Design of Therapeutics for the Treatment of Type II Diabetes and Cardiovascular Disease

Senior Honors Thesis

Submitted by

Jasper Du

May 2017

Chemistry Department

Advisor: Krishna Kumar

Abstract

Part I:

Glucose-dependent insulinotropic peptide (GIP) is a 31-amino acid peptide hormone that is secreted by K-cells to regulate postprandial glucose levels. By binding to its receptor, GIPR, GIP mediates several beneficial effects such as improved insulin sensitivity, increased β-cell mass, and increased energy consumption. However, dipeptidyl peptidase-4 (DPP-4) rapidly inactivates GIP, within 5-7 min. Efforts to extend DPP-4 targeted peptides have included inhibition of DPP-4 and lipidation of peptides. Here, synthesis of a *N*-trifluoroethyl and lipidated GIP was completed. The *N*-trifluoroethyl alkylation of GIP confers proteolytically resistant properties *in vitro*, providing complete resistance to overnight incubations with DPP-4. Compared to native GIP *in vivo*, the N-terminally protected and lipidated GIP remained in circulation at 800x and 80x higher concentrations, owing to the DPP-4 resistance and lipidiation.

Part 2:

Estradiol (E2) in the form of hormone replacement therapy can reduce cardiovascular disease by up to 50%. E2 and other estrogens signal through the classical nuclear estrogen receptor (ER) pathway to mediate many atheroprotective effects such as upregulation of inducible nitric oxide synthase and prostacyclin. E2 can also signal at a rapid alternative pathway through the plasma membrane (mER). mER

stimulates nitric oxide production through various kinases, and selective signaling has shown previously to be atheroprotective. Here, three distinct E2 conjugates were synthesized: a membrane tethered E2 (MT-E2), a transthyretin binding conjugate (TB-E2), and an E2-GLP-1 conjugate. Preliminary *in vitro* studies have shown increased phosphorylation of rapid signaling effector proteins Akt, Erk, and eNOS upon MT-E2 treatment.

Part 3:

Low density lipoproteins (LDLs) are essential for cholesterol transport to various tissues. However, oxidation of LDLs initiates atherosclerosis, leading to the production of plaque. These oxLDLs contain many antigens that can be presented to B-cells for antibody production. Antibodies, namely IgM class antibodies, can be produced against the antigen phosphorylcholine to reduce atherosclerotic lesion progression. Here, phosphatidylcholine is employed in the form of liposomes for the immunization of mice. Preliminary immunizations of mice have shown that these liposomal formulations are capable of eliciting a phosphorylcholine directed IgM response.

Table of Contents

Part I. Lipidation and Stabilization of Glucose-dependent Insulinotropic Peptide for the Treatment of Type II Diabetes

Part II. Targeting the Membrane Estrogen Receptor for the Treatment of Cardiovascular Diseases

Part III. Development of Liposomes as Potential Vaccines for Atherosclerosis

Part I:

Chapter 1. Introduction

1.1 Type II Diabetes: Impact and Pathophysiology

1.1.1 Global Impact of Type II Diabetes

Type II diabetes is a permanent global burden in present day society, afflicting 380 million adults (as of 2014) worldwide.[1] Since 1980, there are nearly four times as many people living with T2D. As of 2016, the global cost of diabetes is 825 billion, and since 90% of all diabetic patients have T2D, most of the diabetic costs derive from T2D.[2]

1.1.2 Insulin Resistance and Hyperglycemia

Individuals with T2D have an increased risk of heart and kidney disease, stroke, blindness, and amputations. All of these risks are linked to hyperglycemia, the hallmark of T2D, and requires significant therapeutic intervention for reversal.[3] The main culprit of hyperglycemia is insulin resistance. Insulin is a 51 amino acid peptide hormone produced by pancreatic β-cells and targets insulin receptors in various tissues such as the liver, adipose tissue, and skeletal muscle.[4] Insulin receptors are tyrosine kinase receptor dimers consisting of an α and β subunit. Upon binding to insulin, a phosphorylation cascade ensues, leading to the activation of the PI3K/Akt pathway. Activation of these kinases such as Akt induces increased glucose transporter type 4 (GLUT4) vesicle transportation and expression at the plasma membrane while attenuating GLUT4 degradation.[4,5] GLUT4

reduces circulating glucose by passive transport through a concentration gradient, where it is immediately phosphorylated by hexokinase and can be further acted upon for glycogen synthesis.

Insulin also prevents hyperglycemia by reducing glycogen breakdown through the activation of protein phosphatase 1 (PP1), dephosphorylating glycogen phosphorylase a to form glycogen phosphorylase b, a less active phosphorylase (Fig. 1).[6] Activation of phosphodiesterase occurs simultaneously, generating adenosine monophosphate AMP from cAMP and inhibiting protein kinase A (PKA).[7,8] Inhibition of PKA precludes phosphorylation of glycogen phosphorylase b to the more active glycogen phosphorylase a. Glycogen phosphorylases are necessary to catalyze the breakdown of glycogen into glucose-1-phosphate for conversion to glucose-6-phosphate, dephosphorylation of glucose-6-phosphate, and ultimate glucose efflux. As glycogenolysis is inhibited, glycogenesis is enhanced. The activation of PP1 results in the dephosphorylation and inactivation of glycogen synthase kinase 3 (GSK-3).[6] GSK-3 is required for converting active glycogen synthase a to the inactive form, glycogen synthase b. Through the inhibition of GSK-3, glycogen synthase a activity increases, augmenting glycogen synthesis.

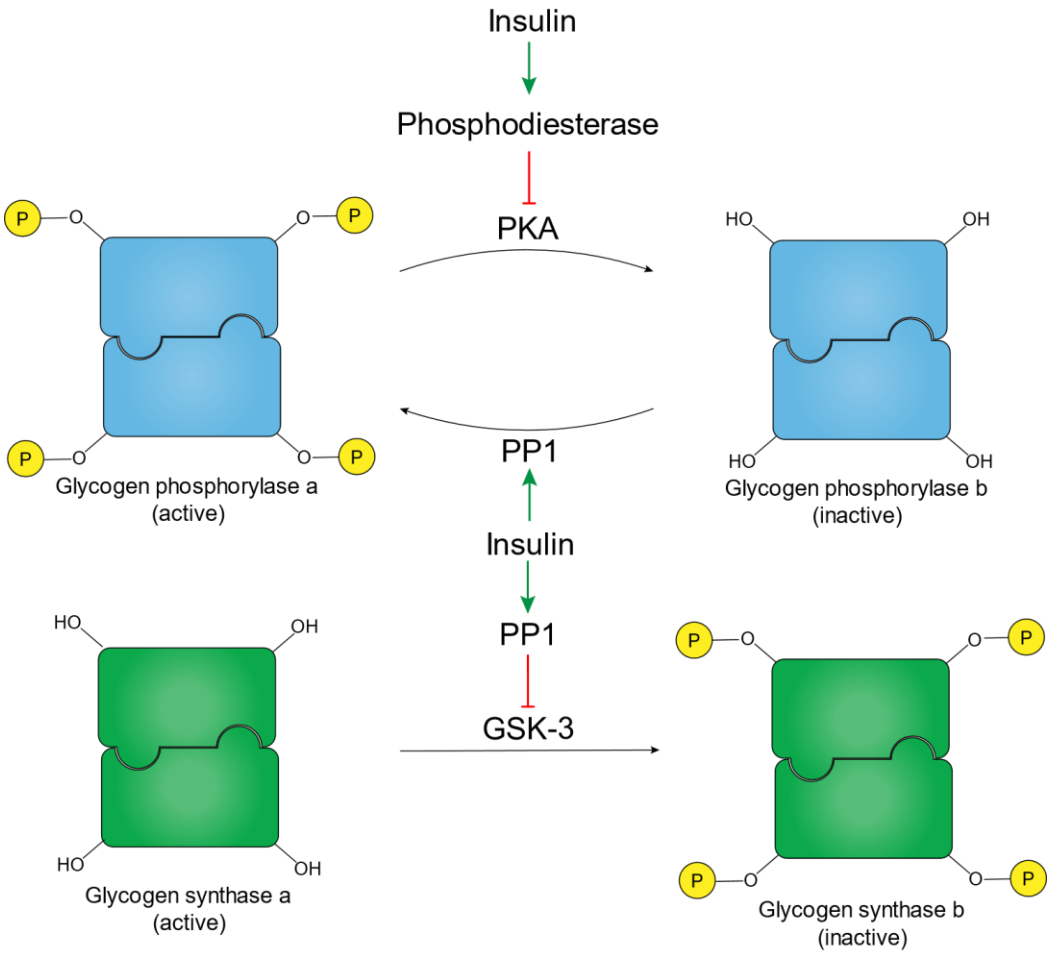

Figure 1. Insulin actions on improving glycogen storage in adipocytes, hepatocytes and myocytes. Insulin activates phosphodiesterase and PP1 to inactivate glycogen phosphorylase b and preserve glycogen synthase a activity.

In T2D, β-cell function is significantly impaired due to insulin resistance, a phenomenon when insulin action on various tissues is diminished. Thus, blood sugar levels remain elevated, and β-cell secretion of insulin surges eventually leading to β-cell dysfunction and defective secretion of insulin.[9] Insulin resistance can be attributed to several mechanisms including lipid accumulation, widespread inflammation and endoplasmic reticulum stress. Further, the consequences of insulin resistance stretch to organs such as the brain, kidney, and intestine. In the liver, muscle, and adipose tissue,

insulin resistance and defective insulin secretion clearly prevents transport of glucose through GLUT4, contributing to hyperglycemia.[5] Impaired insulin signaling also leads to an increase in hepatic glucose production (HGP) as a result of increased gluconeogenesis.[9] The fasting glucose production rate in the liver is approximately 2 mg/kg per min in non-diabetic patients.[9] Yet in diabetic patients the production rate is approximately 2.5 mg/kg per min, resulting in the liver injecting an additional 25-30 g into circulation in an 80 kg individual every night.[10]

Insulin resistance influences the activity of fat cells as well. Insulin generally has anti-lipolytic effects, preventing the breakdown of lipids into fatty acids. Yet in T2D, fat cells become resistant to these anti-lipolytic effects, increasing fatty acid plasma concentration, contributing to increased hepatic gluconeogenesis and sustaining hyperglycemia.[11] Secretion of fatty acids and pro-inflammatory adipokines such as TNFα rather than anti-inflammatory adipokines such as adiponectin, contribute to insulin resistance.[12] In addition, in T2D individuals, adipocytes become engorged with lipids due to their markedly lower storage capabilities, leading to overflow, exacerbating insulin resistance in muscle and liver while decreasing β-cell insulin secretion.[12]

Insulin functions in the brain after crossing the blood-brain barrier through insulin receptor mediated transport.[13] Within the brain, insulin signals at the hypothalamus to increase expression of α-melanocyte stimulating hormone, specifically in the upper and

lower posterior hypothalamus, for the suppression of appetite.[13] Insulin may play a role in stimulating glucose uptake, as GLUT-4 channel expression in the cerebellum of mice can be increased by insulin in a dose dependent manner.[14] Further, insulin directs its regulation of glucose homeostasis in the hypothalamus. It is postulated that insulin induces hyperpolarization of hypothalamic neurons by opening K_{ATP} channels. Hyperpolarization initiates signals that travel through the vagus nerve to hepatocytes, inhibiting HGP.[15]

The filtration property of the kidney is imperative for the reabsorption of glucose by sodium-glucose co-transporters (SGLT) back into circulation. However, in T2D, this reabsorption is intensified, and increased levels of SGLT2 is observed in renal cells of T2D individuals.[16] This suggests that the kidney plays a large role in hyperglycemia, promoting reabsorption of glucose into circulation through the upregulation of SGLT2, rather than preventing reabsorption and eliciting excretion of glucose through urine.

1.1.3 Glucagon Dysfunction in T2D

Insulin is not the sole peptide hormone to play a central role in glucose homeostasis and regulation of hyperglycemia. The secretin family of hormones and receptors have stimulated scientific interest for their roles in T2D. Pancreatic α-cells secrete the 29-amino acid secretin peptide hormone glucagon in response to hypoglycemic conditions. In the absence of disease insulin levels suppresses glucagon activity and release. In the case of non-diabetic patients, sufficient levels of insulin are produced and the glucagon response

is inhibited.[17] Interestingly, this inhibited glucagon response is independent of glucagon plasma concentrations. Further, when rats were treated with insulin, the increased glucagon gene expression was attenuated in a PI3K dependent manner, confirming the role of insulin in controlling glucagon expression.[18,19]

To alleviate low blood sugar levels, glucagon signals at the glucagon receptor in liver cells to release glucose from their glycogen stores (glycogenolysis) as well as increase gluconeogenesis.[20] However in T2D, glucagon signaling is altered, and pancreatic α-cell is non-responsive to hyperglycemia, sustaining glucagon production.[21] Indeed, diabetic individuals have fasting serum glucagon levels that are twice as high compared to their non-diabetic counterparts.[22] Insulin resistance also augments the role of glucagon in hyperglycemia. The development of insulin resistance prevents the uptake of glucose and glycogen synthesis, but glucagon signaling remains uninhibited. Thus, concomitant with glucagon increase is HGP increase; with the doubling of glucagon levels, fasting serum glucose levels nearly tripled.[22] Indeed, HGP depends heavily on glucagon production as >50% glucagon inhibition by somatostatin reduced glucose production by >75%.[23] Taken together, the data surrounding glucagon point to the major role that the secretin family hormones play in hyperglycemia and T2D.

1.2 Incretins and their Origin

1.2.1 Discovery of the Incretins

Although glucagon contributes greatly to T2D pathophysiology, other secretin family hormones act to reverse the complications associated with T2D. In addition to glucagon, glucagon like peptide-1 (GLP-1) and glucose-dependent insulinotropic peptide (GIP) combat hyperglycemia and are known as incretins. The term “incrétine” was first coined by Jean La Barre of Belgium in 1932, when he discovered that these peptides extracted from upper gut mucosa were capable of lowering blood glucose levels.[24] The discovery of the incretins GLP-1 and GIP elucidated the phenomenon known as the incretin effect. In normal human individuals, oral delivery of glucose resulted in improved insulin secretion when compared to intravenous delivery of glucose. An estimated 50-70% of glucose stimulated insulin production can be attributed to the release of incretins after oral glucose administration.[25,26] These gut-originating incretins are not unlike glucagon produced by pancreatic α-cells, despite having contrasting functions. Indeed, both glucagon and GLP-1 are derived from the same precursor, proglucagon.[27]

1.2.2 GLP-1 Biosynthesis and Processing

Initially, proglucagon is cleaved from preproglucagon in either pancreatic α-cells or enteroendocrine L-cells (Fig. 2). Prohormone convertase (PC) 2 is necessary to cleave proglucagon to form glucagon, while PC 1/3 is necessary to cleave proglucagon to form

GLP-1[30,31]. Lys[70]-Arg[71] of pro-glucagon serves as the initial cleavage site for PC1/3 to form glicentin and the major proglucagon fragment (MPGF).[30,31] MPGF is subsequently cleaved by PC1/3 once more at Arg[77] and Arg[109]-Arg[110] forming GLP-1. Glicentin and MPFF can be differentially processed to form the peptide hormones: oxyntomodulin, glucagon, and GLP-2. GLP-1 is a 30 or 31 amino acid long peptide, biologically active in two forms: GLP-1-(7-36) amidated and GLP-1-(7-37). GLP-1 production is mostly accounted for by intestinal epithelial endocrine L-cells as well as neurons in the brainstem, namely the solitary nucleus. Studies in rats have shown that GLP-1 processing and secretion is elicited after meal ingestion through neurotransmitters that induce electrical stimulation of intestinal celiac branches of the subdiaphragmatic vagus nerve.[28] Leptin, a hormone produced in white adipose tissue, is also implicated to have a role in GLP-1 secretion. In both human enteroendocrine L-cells and in mice, leptin stimulated GLP-1 secretion in a dose dependent manner.[29] Overall, the activity of incretins has applications in diseases such as Alzheimer's and Parkinson's, but the following review of incretin signaling will address the role of them in T2D and closely related diseases.

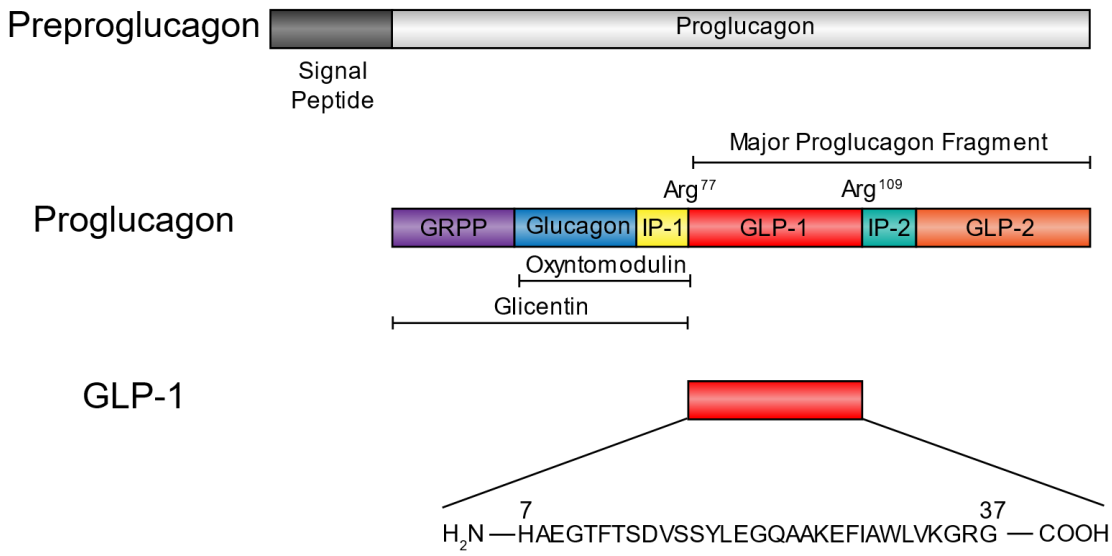

Figure 2. Preproglucagon is cleaved to form proglucagon which can be further differentially cleaved to afford several peptides. PC1/3 cleaves at Arg77 and Arg109 to generate GLP-1. Adapted from Seino et al., 2010.[32] Figure reprinted with permission.

1.2.3 GIP Biosynthesis and Processing

Despite similar post-prandial beneficial outcomes, the 42-amino acid peptide GIP production and secretion is accomplished by enteroendocrine intestinal K-cells rather than L-cells.[33] GIP was originally named gastric inhibitory peptide for its prohibitive effects on stomach acid secretion. With the advent of research elucidating its role in post-prandial effects on insulin secretion, researchers began adopting the name glucose-dependent insulinotropic peptide. The 153 amino acid preproGIP is the precursor of GIP and is subjected to PC1/3 cleavage (similar to GLP-1) at Arg^{22} and Arg^{65} (Fig. 3).[34] An additional carboxypeptidase, unknown currently, is necessary for further post-translational cleavage of Arg^{65} to result in native GIP(1-42). The localization of K-cells in the duodenum and

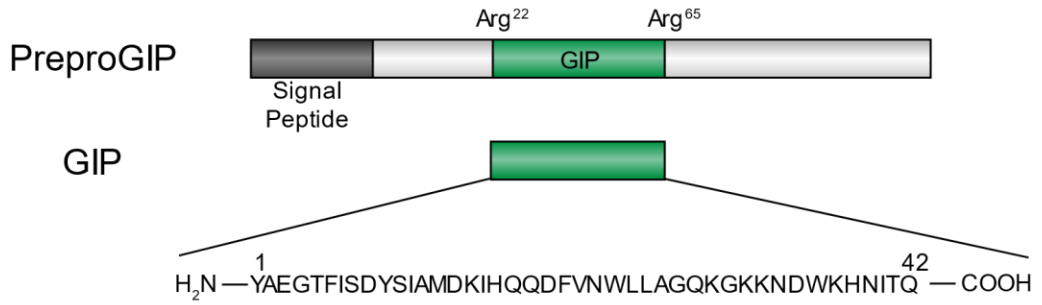

Figure 3. GIP is cleaved from preproGIP through the action of PC1/3 at residues Arg22 and Arg65. Adapted from Seino et al., 2010.[32] Figure reprinted with permission.

proximal jejunum of the small intestine indicates the role of nutrient absorption in secretion of GIP.[35]

1.3 Secretin Family of Receptors

1.3.1 Structure and Binding Mechanism of Receptors

GLP-1 signals at the 463-amino acid secretin family (class B) GPCR, GLP-1 receptor (GLP-1R), while GIP signals at GIP receptor (GIPR) a 455-amino acid class B GPCR.[36] Class B secretin family receptors each consist of two domains: a transmembrane domain comprised of seven α-helices separated by three intracellular loops and three extracellular loops and a N-terminal extracellular domain.[37,38] Coupled to the transmembrane domain are heterotrimeric G proteins involved in cellular signaling upon binding to an agonist. Given the unstable nature of transmembrane GPCRs, only two class B GPCRs have been fully structurally characterized to date, corticotropin-releasing factor

receptor 1 (CRF1) and glucagon receptor (GCGR).[39,40] Still, these structures give much structural insight to the class B family of GPCRs. Interestingly, both receptors orient their transmembrane helices to reveal a large "V-shaped" opening at the extracellular face, a substantially more pronounced opening in comparison to other GPCRs.[37] The binding mode of class B GPCR ligands are nearly the same. Upon binding to the GPCR, the peptide changes from a largely disordered conformation to an α-helix.[38] Interestingly, when peptide ligands such as $GIP_{(1-42)}$ and $GLP\text{-}1_{(7-36)}$ are cleaved at the N-terminus to form $GIP_{(1-42)}$ and $GLP\text{-}1_{(9-36)}$, they are still capable of binding to the GPCR, but act as antagonists.[41,42] Still, this suggests that the N-terminus of the peptide ligand is not required for binding. Further, this C-terminal interaction is imperative for receptor binding. PACAP and GLP-1 in addition to other ligands rely on the C-terminal insertion in between two ECD β-sheets.[38,41,42] Thus, C-terminally deleted peptides have a binding affinity that is significantly reduced. Experiments involving hybrid peptides further investigated the N- and C- termini role in binding and activation. A hybrid secretin peptide consisting of the N-terminus of calcitonin and the C-terminus of parathyroid hormone (PTH) was unable to activate their respective receptors CTR and PTHR.[38,43] Yet when a hybrid receptor consisting of a transmembrane from CTR and an ECD from PTHR, binding and activation was observed. These hybrid experiments were expanded to other secretins and developed into the "two domain" binding model.[44] This model postulates that for the activation of class B GPCRS,

an initial complex is formed between the C-terminus of the peptide and the ECD, and then the N-terminus interacts with the transmembrane domain for activation. It is proposed that the incretins GLP-1 and GIP bind and activate their respective receptors in this manner as well.

1.4 Incretin Action in the Body

1.4.1 GLP-1 in the Pancreas

GLP-1R is widely expressed among the tissues of the human body such as the pancreas, intestine, heart, kidney, brain and central nervous system. GLP-1R activity in the pancreas confers important glycemic controlling effects. Upon binding to GLP-1R, and release of Gαs, the GLP-1 leads to adenylate cyclase activation and subsequent cAMP production (Fig. 4).[32,45] cAMP then mediates insulin secretion through either a PKA dependent or PKA independent exchange protein activated by cAMP2 (EPAC2) mechanism. PKA activation results in activation of the transcription factors insulin promoter factor (PDX-1) and cAMP response element-binding protein (CREB), and thus upregulating the transcription of insulin.[46] Sulfonyl receptor 1 (SUR1) a subunit of the K_{ATP} channel is subjected to PKA serine phosphorylation, inhibiting the K_{ATP} channel.[47] cAMP independent signaling through the PI3K pathway and subsequent atypical isoform zeta of PKC (PKCζ) activation compounded with PKA action leads to the deactivation of K_v

channels.[48] K_v channels work in tandem with K_{ATP} channels, as depolarization from deactivation of K_{ATP} channels can be reversed through the repolarization actions, of K_v channels, necessitating dual inhibition. Depolarization from deactivation of the K_{ATP} ion channel by PKA and prevention of repolarization by K_v channels results in enhanced insulin secretion by pancreatic β-cells through Ca^{2+} signaling. PKA signaling in conjunction with PKCζ increases intracellular Ca^{2+} stores through two mechanisms. Depolarization opens plasma membrane L-type voltage-dependent calcium channels and induction of Ca^{2+} release from intracellular stores both increase levels of intracellular calcium, resulting in increased exocytosis of insulin secretory vesicles[49]. Further, EPAC2 stimulates Ca^{2+} release from the endoplasmic reticulum and increases insulin granule density by activating the GTPase Rap1.[50–52]

In addition to insulin, GLP-1 attenuates the production of glucagon in pancreatic α cells, though the mechanism is not fully elucidated. It is thought that GLP-1 mediates glucagon inhibitory effects indirectly, since there are no studies that show direct *in vivo* GLP-1 activity on GLP-1R of pancreatic α-cells. Studies *in vitro* implicate that GLP-1 enhanced somatostatin secretion may play a role in suppressing glucagon secretion.[33,53] It is postulated that somatostatin secretion may facilitate cAMP/PKA-dependent inactivation of low voltage activated Ca^{2+} and Na^{+} channels following depolarization by inhibition of α-cell K_{ATP} and A-type K^{+} channels as the cause of inhibited glucagon secretion.

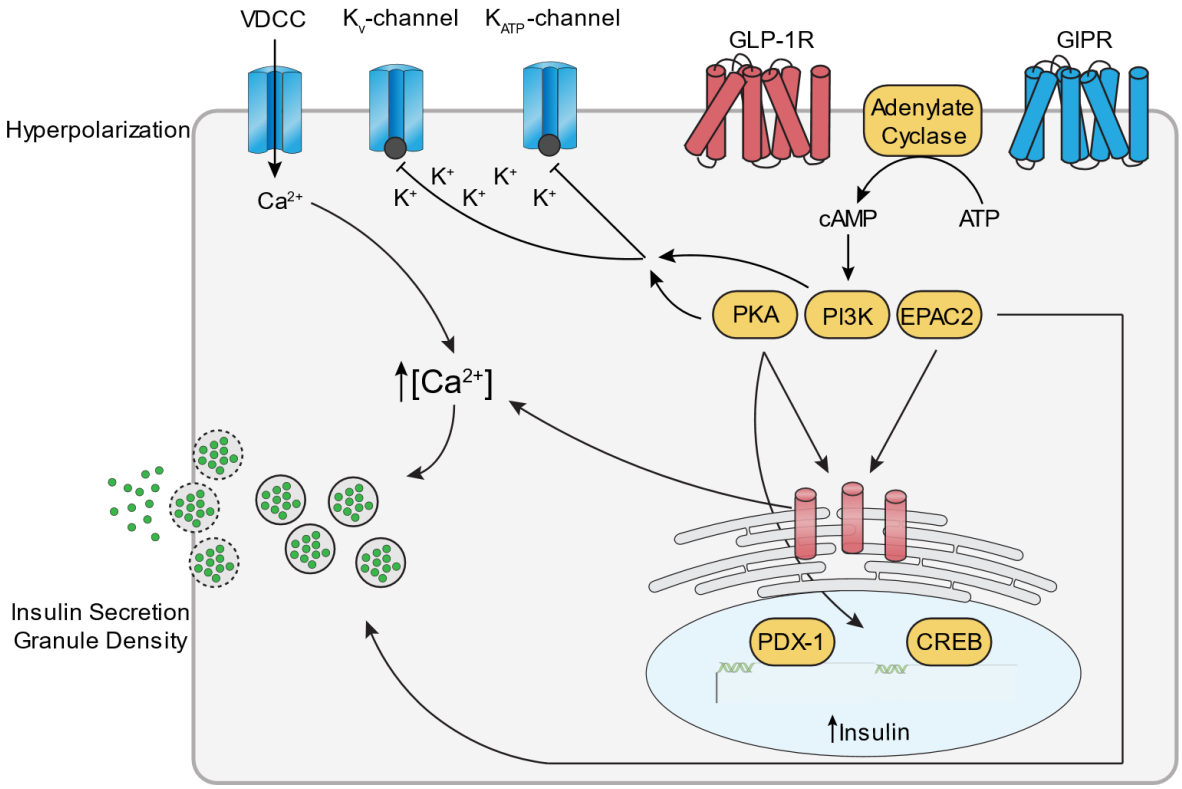

Figure 4. Incretin signaling in the pancreatic beta cell to increase insulin production. Through hyperpolarization and cAMP mediated pathways, incretins can stimulate insulin secretion and insulin biosynthesis. Adapted from Seino et al., 2010[32]. Figure reprinted with permission.

Effector functions of GLP-1 signaling increase β-cell mass through augmenting cell growth and inhibiting apoptosis. GLP-1R participates in transactivation of epidermal growth factor receptor (EGFR) after activation of c-Src and subsequent betacellulin production.[54] EGFR operates through PI3K to activate Akt, PKCζ and PKB to mediate cell proliferative effects, such as transcription of PDX-1.[54–57] Indeed, *Pdx1*$^{-/-}$ knockout mice revealed that activation of the transcription factor PDX-1 is required for cell proliferative and cell death inhibitory effects of GLP-1.[58] In addition to the insulin enhancing capabilities, the cAMP/PKA pathway and activation of CREB leads to Akt-PKB mediated proliferation and survival[59]. By enhancing the activity of NF-κB, anti-apoptotic proteins such as BCL-2,

and BCL-xL are increased, contributing to cell survival.[60,61] BCL-2 and BCL-xL play a role in thwart direct activation and oligomerization of pro-apoptotic proteins BAX and BAK, impeding mitochondrial outer membrane permeabilization and subsequent cytochrome c release.[62]

1.4.2 GLP-1 Function in Auxiliary Tissue

Though most widely studied in the pancreas, GLP-1 signaling is not limited to this tissue. To mediate inhibitory actions on gastric emptying, GLP-1 signals in the duodenum through the gastrointestinal vagal afferents, increasing feelings of satiety.[63,64] The direct anorectic action of GLP-1 on the central nervous system is less clear. Sisley et al., 2014 used Cre-Lox recombination to produce either CNS or visceral nerve *Glp1r* knockout mice.[65] In CNS Glp1r knockdown mice, treatment with GLP-1 mimetic liraglutide was unable to mediate restricted food intake and body weight lowering effects. Conversely, liraglutide was still able to mediate these effects in vagal GLP-1R knockdown mice. More specifically, Secher et al. identified that the arcuate nucleus was the target of liraglutide for reducing body weight.[66] GLP-1 also signals in the brainstem to increase energy expenditure as indicated by elevated levels of brown adipose tissue thermogenesis and oxygen consumption.[67–69] Direct GLP-1 signaling at the gastric parietal cells is also postulated to contribute to delayed gastric emptying.[70] Reduction of blood glucose levels

is also observed, as the emptying of nutrients into the small intestine is attenuated, slowing absorption of glucose.[33] In skeletal muscle and hepatocytes, rat studies show enhanced glucose uptake, glycogen synthase activity, and glucose metabolism and inhibited HGP.[71–73] Indeed, GLP-1 directly signals at GLP-1R of hepatocytes stimulating cAMP production, insulin sensitivity, and elimination of liver fat (hepatic steatosis).[74] GLP-1 receptor agonists have observed anti-atherosclerosis effects, which is imperative as most T2D patients ultimately succumb to CVD related deaths. In atherosclerotic *Apoe*$^{-/-}$ mice treated with GLP-1 and GLP-1 mimetics, suppressed macrophage infiltration, smooth muscle cell proliferation, foam cell formation, and plaque progression.[75,76] In endothelial cells, endothelial nitric oxide synthase activity is increased, resulting in increased nitric oxide production and vasodilation, implicating the role of GLP-1 in atherosclerosis.[77]

1.4.3 GIP Function in the Pancreas

GIP targets GIPR on pancreatic β-cells and subsequent signaling to induce insulin secretion identically to that of GLP-1. GIP binds to the G-coupled protein receptor GIPR expressed on the cell membrane of β-cells to catalyze the formation of intracellular cAMP via adenyl cyclase which activate both PKA and EPAC2.[78,79] Sustained depolarization from inhibition of K_{ATP} and K_v channels and opening of L-type voltage dependent calcium channels is also observed in GIP-subjected pancreatic β-cells.[49] Thus, improved insulin secretion is accomplished through GIP signaling.

GIP also has role in both the proliferation and prevention of apoptosis in pancreatic β-cells. Like GLP-1, GIP mediates anti-apoptotic effects through both PKA and PKB, contributing to increased β-cell mass. PKA translocates to the nucleus, phosphorylates CREB, and inhibits AMP-activated protein kinase (AMPK).[80] Dephosphorylation at Thr172 of AMPK results in dephosphorylation of transducer of regulated CREB activity 2 (TORC2). TORC2 nuclear translocation occurs and TORC2 binds to phosphorylated CREB to increase BCL-2 gene expression. Activation of the Akt/PKB pathway results in the inactivation of Foxo1, precluding binding to Foxo1 response elements, downregulating BAX, an important pro-apoptotic protein necessary for oligomerization and MOMP.[81] Activation of Akt/Pkb also leads to the prevention of BimEL and Bad translocation to the mitochondria and thus prevents MOMP, as BimEL and Bad are pro-apoptotic proteins capable of either directly activating BAX or sequestering BCL-2.[82,83] To induce proliferation of β-cells, GIP operates through the cAMP/PKA signaling pathway to activate the RAF-MEK1/2-ERK1/2 pathway.[84] Both GIP and GLP-1 also increase expression of cyclin D1, a critical cell cycle component important for the switch from G0 to G1-S, in pancreatic β-cells, stimulating their growth. [85] Interestingly, in pancreatic α-cells, GIP is responsible for the secretion of glucagon, which may pose difficulty when regulating hyperglycemia.[86]

1.4.4 GIP Function in Auxiliary Tissue

In adipose tissue, GIP functions to reverse breakdown of lipids. GIP upregulates proteins such as lipoprotein lipase by activating the Akt/PKB pathway for the enhancement of fatty acid synthesis and production of triglycerides[87]. Yet the role of GIP in adipocytes is still unclear, as *Gipr*$^{-/-}$ mice have improved insulin sensitivity and display attenuated weight gain.[88] Further, in *Gipr*$^{-/-}$ mice, energy expenditure markedly increases and fat is utilized as an energy source.[88]

1.5 DPP-4-directed Proteolysis and Solution

1.5.1 DPP-4 Action and Mechanism

Taken together, the extensive impact of incretins on various tissues such as the pancreas, brain, and adipose tissue point to their use as a treatment for T2D. Indeed, the two incretins account for an estimated 50% of all post-prandial insulin secretion.[89] Zander et al., in 2002, explored the use of native GLP-1 as a treatment for T2D.[90] Continuous subcutaneous injection of GLP-1, accomplished by a portable insulin pump, produced significant results. Glucose concentration and fatty acid concentrations were reduced, gastric emptying was inhibited, weight loss was observed, and insulin sensitivity was enhanced. However, a persistent challenge remains with using native incretins as a therapeutic is attributed to the cleavage by endogenous serine protease dipeptidyl peptidase 4 (DPP-4). Intravenous infusions revealed that the serum half-lives of GLP-1

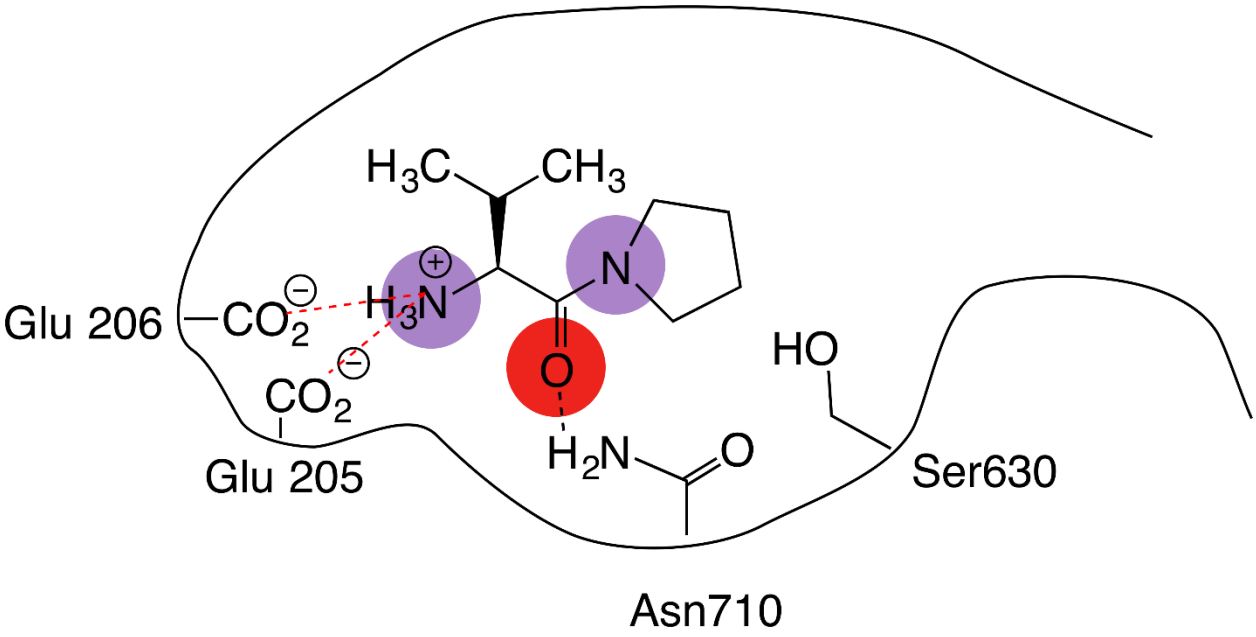

Figure 5. DPP-4 recognition and active site. Val-Pyr is shown above forming essential salt bridges and hydrogen bonds with glutamate and aspartate residues, respectively priming the Ser630 for attack. Generated using data from Rasmussen et al., 2003.[94]

and GIP are 1.5-3 min, and 5-7 min, respectively.[33,91] DPP-4 is expressed in two forms, as a transmembrane protein, and soluble DPP-4 after cleavage from the plasma membrane through receptor shedding.[92] DPP-4 is a ubiquitous protein, and can be found on the surfaces of gut endothelial cells.[93] Thus, incretins are cleaved upon secretion by membrane DPP-4, before draining into major circulatory blood vessels. Cleaved soluble DPP-4 is a dimeric enzyme consisting of an α/β-hydrolase domain and an eight bladed β-propeller domain.[94] Structural characterization studies using the competitive inhibitor valine-pyrrolidide (Val-Pyr) elucidated key binding residues (Fig. 5).[94] The binding site of DPP-4 relies on Glu205 and Glu206 to mediate salt bridges with the N-terminus of Val-Pyr. This substrate-enzyme interaction is further stabilized by hydrogen bonding between a

carbonyl and residues Asn710 and Arg125. The salt bridges are essential for the proteolytic activity of DPP-4 as these interactions constrain the active site, aligning Ser630 for proteolytic action. Indeed, alanine mutations of either Glu205 and Glu206 inhibits proteolytic activity of DPP-4.[95] DPP-4 cleavage removes the first two N-terminal amino acids, resulting in truncated metabolites GLP-1_{9-36} and GIP_{3-42}. GLP-1_{9-36} only has 1% binding affinity compared to GLP-1_{7-36}, and is a weak antagonist of GLP-1R.[96] GIP_{3-42} has also been observed *in vitro* to inhibit GIPR, and both insulin and glycemic responses are significantly reduced *in vivo*, compared to native GIP.[97]

1.5.2 DPP-4 Inhibitors

The rapid cleavage of incretins by DPP-4 has led to the development of a class of T2D therapeutics known as DPP-4 inhibitors. Indeed, animal experiments have shown that active GLP-1 expands from 10% of total GLP-1 to 99% of total GLP-1 after introduction of a DPP-4 inhibitor.[98] Further, the FDA has approved DPP-4 inhibitors such as sitagliptin (Merck & Co) for clinical use and treatment for T2D. However, inhibiting DPP-4 does not induce weight loss and may pose a risk for long term safety, as DPP-4 is responsible for the catalysis of more than 30 other substrates.[99,100]

1.5.3 Incretin Receptor Agonists

Another therapeutic approach is to extend the stability of active incretins through chemical modifications. In contrast to DPP-4 inhibitors, longer acting GLP-1 mimetics have shown to produce greater glucose-lowering effects as well as induce weight loss.[99] Liraglutide a GLP-$1_{(7\text{-}37)}$ mimetic with two amino acid substitutions, and most notably, contains a glutamate-palmitic acid adduct at Lys26.[99] Fatty acid acylation confers extended stability of GLP-1 ($t_{1/2}$ = 11-15 hr) mediated by binding to serum albumin.[101] Albumin is a globular 67 kDa protein that represents 60% of serum proteins (serum concentration: 600 μM) and is responsible for the transport of hormones and fatty acids while sustaining osmotic pressure.[102,103] Albumin has the capability of binding to multiple fatty acids concurrently, and thus is capable of binding to the lipid moiety of liraglutide. Albumin complexes are larger than the maximum size required for renal clearance (~8 nm) thereby increasing the circulatory pool of liraglutide.[104] Further, liraglutide forms aggregates, specifically a heptamer with a micelle-like shape, which may aid in reducing DPP-4 access to liraglutide and subsequent inactivation.[105,106] Though degradation may be slowed, liraglutide is still susceptible to DPP-4 cleavage, necessitating alternative modifications to circumvent this.

Analogs of GLP-1 substituting Ala^8 with 2-aminoisobutyric acid (Aib) have been shown to be resistant to DPP-4 cleavage while retaining potency and receptor binding

affinity.[107] Taspoglutide, a GLP-1 mimetic containing this adaptation entered phase 3 clinical trials but was withdrawn due to safety risks such as nausea, vomiting and immune system hypersensitivity.[108]

1.6. Design Considerations

1.6.1 Improvement on Current Therapeutics

Despite the advent and acceleration of the peptide therapeutics market in T2D, namely with incretins, the problem of stabilizing peptides remains. Recently, investigations in the Kumar group have discovered that modifications to the N-terminus of the incretin GLP-1 can confer resistance against DPP-4 cleavage while retaining potency. The notion of *N*-terminal modifications is not new, and has been previously explored. Siegel et al., synthesized an *N*-acetylated GLP-1, and though it was resistant to degradation by DPP-4, nearly 40-fold loss of potency was observed.[109] However, our findings have shown that alkylations of GLP-1, namely *N*-trifluoroethyl alkylations, are sufficient to provide stability against DPP-4 yet retain potency *in vitro*. The mechanism of resistance for N-terminal modifications is likely due to the change in pKa after acetylation or alkylation. Without protonation at the N-terminus, key recognition and binding through salt bridges with DPP-4 residues Glu205 and Glu206 is impeded, precluding proteolysis. Further, this modification has been applied to liraglutide and exenatide, leading GLP-1 receptor agonists currently in the clinic, and the identical stabilization properties are observed.

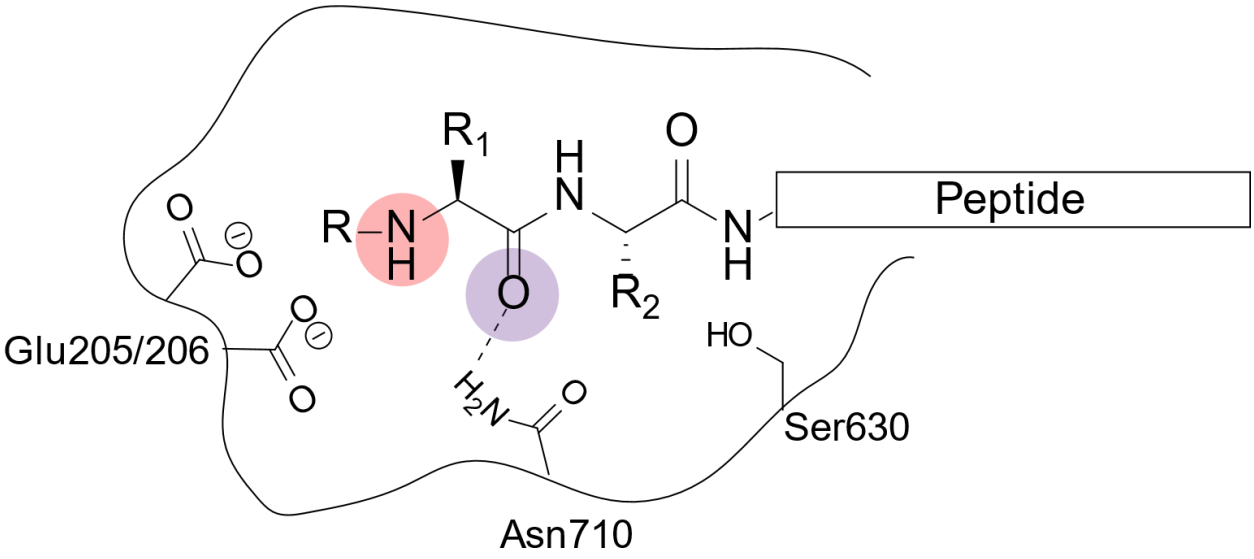

Figure 6. DPP4 active site and recognition after N-terminal alkylation. The pKa is effectively reduced and the N-terminus can no longer be protonated. Subsequent glutamic acid salt bridge formation is inhibited.

Given the success with *N*-trifluoroethyl alkylated of GLP-1, the same strategy was applied for the sister incretin GIP with similar results. Since modifications are made at the *N*-terminus, acylations such as in liraglutide can still be explored and extend half-life further. Therefore, a palmitoylated GIP containing an *N*-trifluoroethyl modification was pursued for the treatment of T2D.

1.6.2 Experimental Design

Initially, both the structures of GLP-1 with GLP-1R ECD and GIP with the GIPR ECD were analyzed for similarities. Interestingly, both GLP-1 and GIP adopt similar conformations upon examination of their structures with the ECD of GLP-1R and GIPR, respectively. Next, since K26 was utilized for $GLP\text{-}1_{7\text{-}36}$ as the site of palmitoylation, K26 was compared to Q20 of $GIP_{1\text{-}42}$. The Q20 residue of GIP is in a similar position as the K26 residue of GLP-1 position (both the 20^{th} amino acid of each respective peptide) with

respect to the ECD. The K26 residue of GLP-1 participates in hydrogen bonding with the E128 residue of GLP-1R, though this interaction is weak (Fig. 6A). GIP maintains a similar interaction with its respective receptor. Q20 participates in hydrogen bonding with the N120 residue of GIP, mediated by two nearby water molecules (Fig. 6B). Indeed, just as the K26-E128 interaction of GLP-1/GLP-1R is unstable, water-mediated hydrogen bonds are also unstable, rendering the Q20 residue as prime candidate for lipidation. However, since the Q20 side chain is amidated, substitution with a lysine was employed to permit palmitoylation.

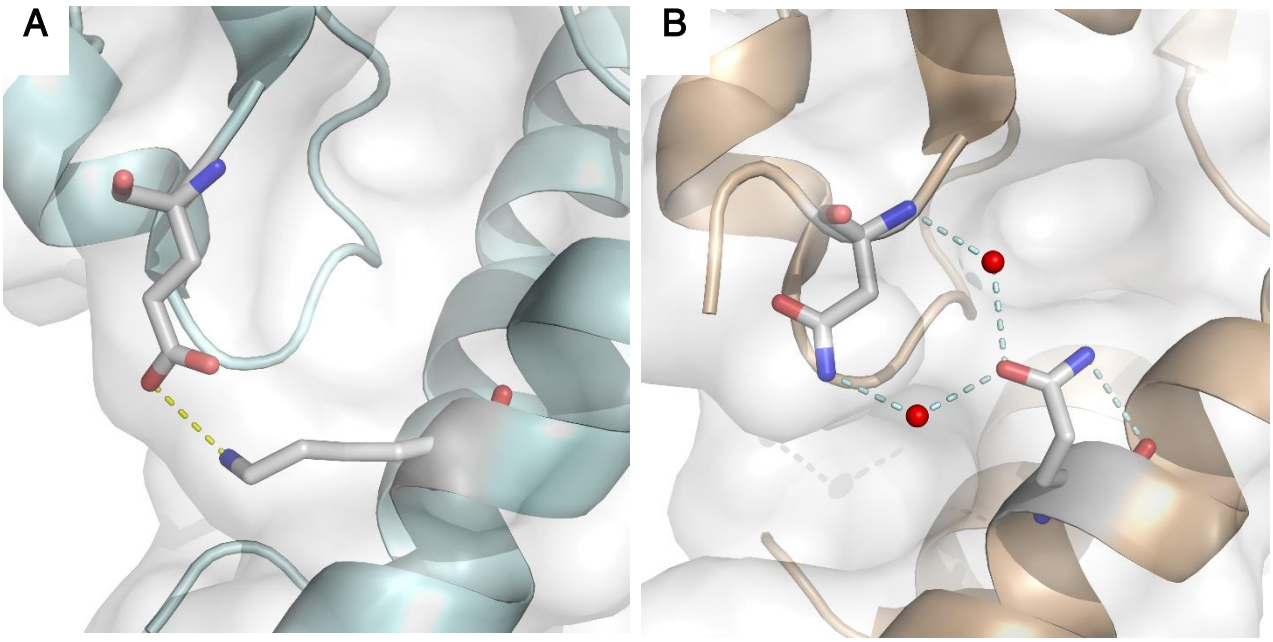

Figure 7. Incretins bound to the ECD of their native receptors. A. K26 residue of GLP-1 participates in hydrogen bonding with E128. B. Q20 residue of GIP participates in hydrogen bonding with N120, mediated by two water molecules. Generated using PyMol from PDB: 2QKH (GIP) 3IOL (GLP-1).

1.6.3 Oral Delivery of Peptides

Further enhancement of peptide therapeutics can be accomplished by improving delivery of the peptide. Currently, 61% of peptide therapeutics are taken by injection, whereas only 9% of peptide therapeutics are taken orally.[110] The central challenges with oral delivery of peptides are the: harsh conditions of the acidic stomach and ability for the peptide to travel across the blood-gut barrier, also known as the intestinal epithelial barrier.[111] Tight junctions between the epithelial cells preclude crossing of peptides into the bloodstream. Recently, major advances in the field has produced several candidates to increase bioavailability of peptides. For example, Merrion Pharmaceuticals have developed GIPET, an enteric coated tablet (prevents against dissolution in the stomach) that consists of medium chain fatty acids, which aid in transport across the intestinal epithelial barrier by contracting actin filaments.[112] Emisphere Technologies has developed its own "Eligen Technology" consisting of two promising candidates: sodium N-[8-(2-hydroxybenzoyl)amino]caprylate (SNAC) and 8-(N-2-hydroxy-5-chloro-benzyl)-amino-caprylic acid (5-CNAC).[113] The former is currently in Phase III clinical trials with semaglutide, a once weekly GLP-1 analog, and has comparable efficiency to the injected form of semaglutide. The mechanism of action has not been fully elucidated, but Malkov et al., has investigated transport of insulin with SNAC.[114] Malkov et al. utilized the fluorescent probe Bis-ANS to bind exposed hydrophobic regions. Insulin-SNAC solutions

displayed a higher fluorescence intensity than either SNAC or insulin alone, implicating the ability of SNAC to increase hydrophobicity and thus lipophilicity. Indeed, fluorescence confocal microscopy show that transcellular absorption across the intestinal epithelial barrier can be achieved. Further, cytoskeleton remodeling that may impact the integrity of tight junctions were not observed. In addition, SNAC confers a “shielding” effect by protecting insulin from trypsin and chymotrypsin access and digestion within the digestive tract.

Given the success of SNAC, we sought to synthesize SNAC for application with our own trifluoroethyl alkylated peptides, to the same end. Existing methods and patents outline a method to produce SNAC on an industrial scale, whereas there are no methods available for the synthesis of SNAC on a smaller, laboratory scale. Therefore, the goal of the following synthesis routes is to synthesize SNAC without the use of industrial equipment.

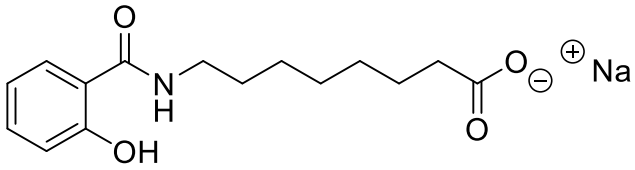

Figure 8. Structure of SNAC.

Chapter 2: Experimental Section

All organic reactions were performed under argon atmosphere. All solid phase peptide chemistry was carried out in a 10-mL reaction vessel under nitrogen atmosphere. Residues 3-42 (on Wang resin) were obtained from the Tufts University School of Medicine Core Facility. Reagent equivalents for all peptide couplings were as follows: amino acid building block (0.4 mmol, 16 eq) HBTU/HATU (0.36 mmol, 14.4 eq) *N,N*-diisopropylethylamine (110 µL, 0.63 mmol, 25 eq). Fmoc was deprotected with 20% piperidine (1x5 min, 1x15 min). Phenylsilane (100 mg) and 5 mL DCM was added to the reaction vessel, and the resin was degassed for 5 min. $Pd(PPh_3)_4$ (30 mg) was added directly and the reaction vessel was shaken for 6h. Resin was washed and excess palladium was removed with the scavenger sodium diethyl dithiocarbamate trihydrate (50 mg) dissolved in DMF (5x2 mL). After cleavage, the crude product was purified by reverse phase high performance liquid chromatography (RP-HPLC) on a C18 Vydac column using a gradient of 40% B (90% acetonitrile, 10% H_2O, 0.07% TFA)/60% A (99% H_2O, 1% acetonitrile, 0.01% TFA) to 57% B/43% A over 30 min at 50°C. Two rounds of purification were completed to obtain pure compound. Analytical RP-HPLC [Vydac C18, 7 µm, 4.6 mm × 250 mm] was completed to ascertain purity of JLD-GIP.

Solvent A: 1% acetonitrile, 99% H_2O, 0.1% TFA

Solvent B: 90% acetonitrile, 10% H_2O, 0.07% TFA

Solvents for reactions were dried on an Innovative Technologies PureSolv 400 solvent purifier. NMR solvents were purchased from Cambridge Isotope Labs. All chemicals were purchased at the highest possible purity from ChemImpex and Sigma-Aldrich and used as received. Flash column chromatography was performed on SiliCycle P-60 silica gel, 230-400 Mesh. Analytical and preparative thin layer chromatography (TLC) was carried out on EMD silica gel 60 F-254 plates. Products were visualized using UV or by staining with 5% aqueous sulfuric acid or ceric ammonium molybdate. NMR spectra were recorded on a Bruker Avance III NMR spectrometer at 500 MHz for ^1H NMR, 125 MHz for ^{13}C NMR, and 500 MHz for Gradient HSQC. Chemical shifts are reported in ppm relative to tetramethylsilane (for ^1H NMR in $CDCl_3$) or $CDCl_3$ (for ^{13}C NMR in $CDCl_3$). For ^1H NMR spectra, data are reported as follows: δ shift, multiplicity [s = singlet, bs = broad singlet, d = doublet, dd = doublet of doublets, ddd = doublet of doublet of doublets m = multiplet, t = triplet, td = triplet of doublets], coupling constants are reported in Hz. Low resolution mass spectra (LRMS) were obtained using a Finnigan LTQ ESI-MS with an additional APCI source.

Luciferase reporter assays were performed by scientists in Dr. Martin Beinborn's laboratory at the Tufts Medical Center. Briefly, human embryonic kidney 293 cells (HEK293) were grown and plated in the wells of a clear-bottomed 96-well plate with approximately 6 × 103 cells per well. After reaching near 80% confluency in the wells, cells were transiently transferred with the cDNA encoding GLP-1R (3 ng/well)*, CRE6X-LUC-hCL-PEST* reporter gene (25 ng/well), and β-galactosidase (10 ng/well). After 24 hours, the cells were incubated with a GLP-1 mimetic for 6 hours in serum-free medium. The cells were aspirated prior to lysis. After lysis, Steadylite® reagent was added, leading to its cleavage based on luciferase expression. TopCountNTX was used to quantify the luminescence. To control for transfection efficiency, a β-galactosidase assay was performed by addition of 2-nitrophenyl β-D-galactopyranoside and incubation for 30-60 minutes at 37 ˚C. The cleavage of this substrate by β- galactosidase was monitored by measurement of optical density at 420 nm using a SpectraMax® instrument and correlated to β-galactosidase expression. The luciferase data were then standardized for transfection efficiency using the β-galactosidase assay. The DPP-4 cleavage experiments performed by Dr. Martin Beinborn and members of his lab. 10 ng/well of DPP-4 was incubated with 10 μM peptide overnight. After, the peptide was diluted appropriately and added to the wells containing transfected cells. The luciferase assay was performed to quantify potency of the peptide. To determine concentration of a GLP-1 analog remaining in the blood of animals after *in vivo* studies, whole blood or plasma was diluted and then added to the wells with transfected cells. Luciferase assay was performed as above.

Synthesis of N^{α}-trifluoroethyl Tyrosine

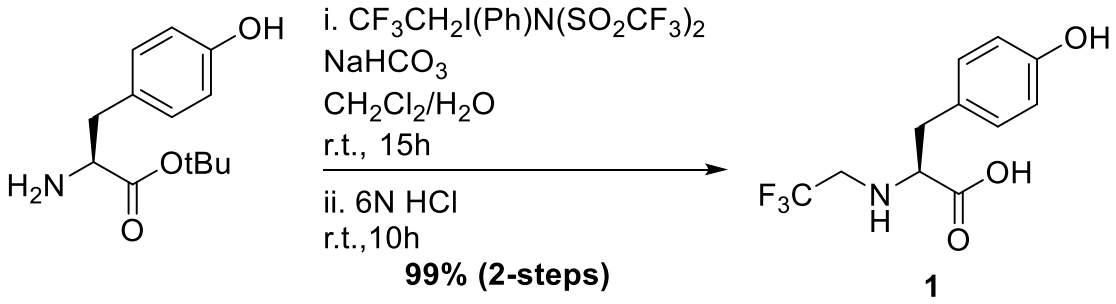

1

In preparation for addition to the GIP peptide template by solid phase peptide synthesis (SPPS), N^{α}-trifluoroethyl L-tyrosine was synthesized. L-tyrosine tert-butyl ester (956 mg, 3.5 mmol, 1.0 eq) and $NaHCO_3$ (800 mg, 9.52 mmol, 2.72 eq), were dissolved in 30 mL DCM and 30 mL. $CF_3CH_2I(Ph)N(SO_2CF_3)_2$ (iodonium salt) was subsequently added and stirred at room temperature for 15h. The reaction mixture was washed with brine (2x50 mL) and the organic layer was extracted. The organic layer was dried over anhydrous sodium sulfate and concentrated to an oil. 6N hydrochloric acid (20 mL) was added to the crude oil. The reaction mixture was stirred at room temperature for 10h. The reaction mixture was dried *in vacuo* and the reaction was repeated to afford the product with quantitative yield. The product was confirmed by ^{1}H, ^{13}C, ^{19}F, and HSQC NMR. Mass was confirmed by ESI-MS.

^{1}H NMR (MeOH, 500 MHz) δ: 7.15 (d, 2H, 8.5 Hz), 6.79 (d, 2H, J 8.0 Hz), 4.32 (dd, 1H, J = 1.5 Hz, J = 6.00 Hz), 4.03 (td, 2H, J = 3.0 Hz, J = 9.0 Hz), 3.29 (d, 1H, J = 6.0 Hz), 3.19 (dd, 1H, J = 7.0 Hz, J = 7.5 Hz)

^{13}C NMR (MeOH, 125 MHz) δ: 130.18, 115.34, 61.77, 46.04, 34.28

^{19}F NMR (MeOH, 500 MHz) δ: 69.47

ESI^{+}: calcd for $[C_{11}H_{12}F_3NO_3 + H^{+}]$ 264.09, found 264.09 $[M + H^{+}]$

JLD-GIP Synthesis

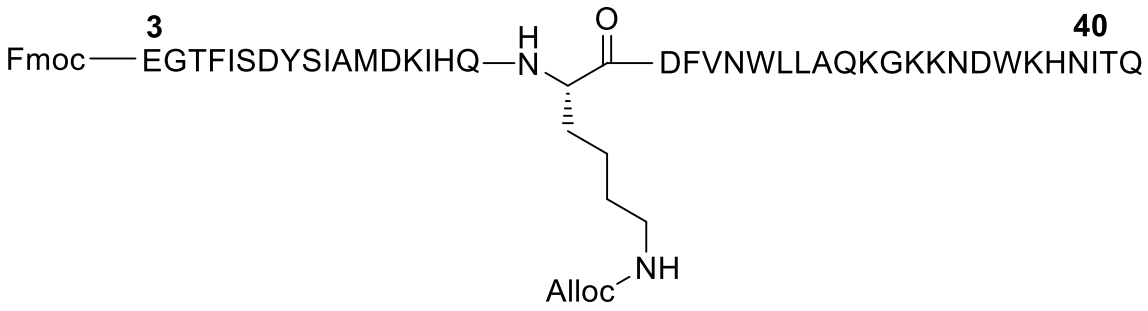

JLD-GIP was synthesized on a 0.025 mmol scale and the remaining peptide was prepared as per standard Fmoc SPPS. It is important to note that all couplings were carried out with the coupling reagent HBTU, except CF_3CH_2-Tyrosine, which was carried out with HATU. Each coupling was confirmed by Kaiser (ninhydrin) test. The K20 residue was Alloc protected, and selectively deprotected with tetrakis(triphenylphosphine)palladium(0) and phenylsilane. JLD-GIP was cleaved from the resin using a trifluoroacetic acid cleavage mixture (95 TFA:2.5 triisopropylsilane:2.5 H_2O), precipitated with diethyl ether, and dried *in vacuo*. Two rounds of purification were completed to obtain a pure compound (~1.4 mg). JLD-GIP was confirmed by ESI-MS.

ESI$^+$: calcd 5433.8496 $[M+H]^+$, found 1811.91 $[M+H^+]^{2+}$, 1359.36 $[M+H^+]^{4+}$, 1087.82 $[M+H^+]^{5+}$

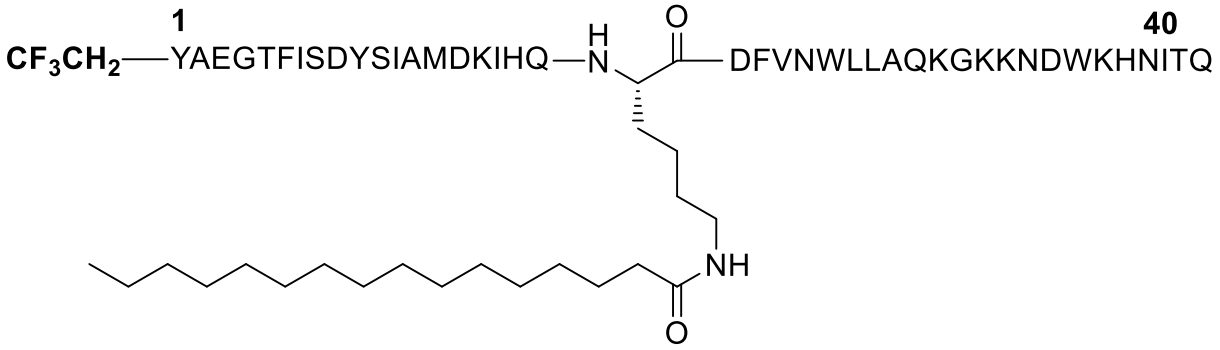

Purified JLD-GIP was dissolved in 100 µL DMSO. A 1:10 dilution in PBS was performed and the concentrations were ascertained by UV-Vis spectrometry on a Nanodrop. Absorbance was measured at λ = 280 nm. Using the Beer-Lambert law (length = 0.1 cm, extinction coefficient = 13980) and the concentration was determined to be 0.897 M.

Initial Synthetic Route for SNAC

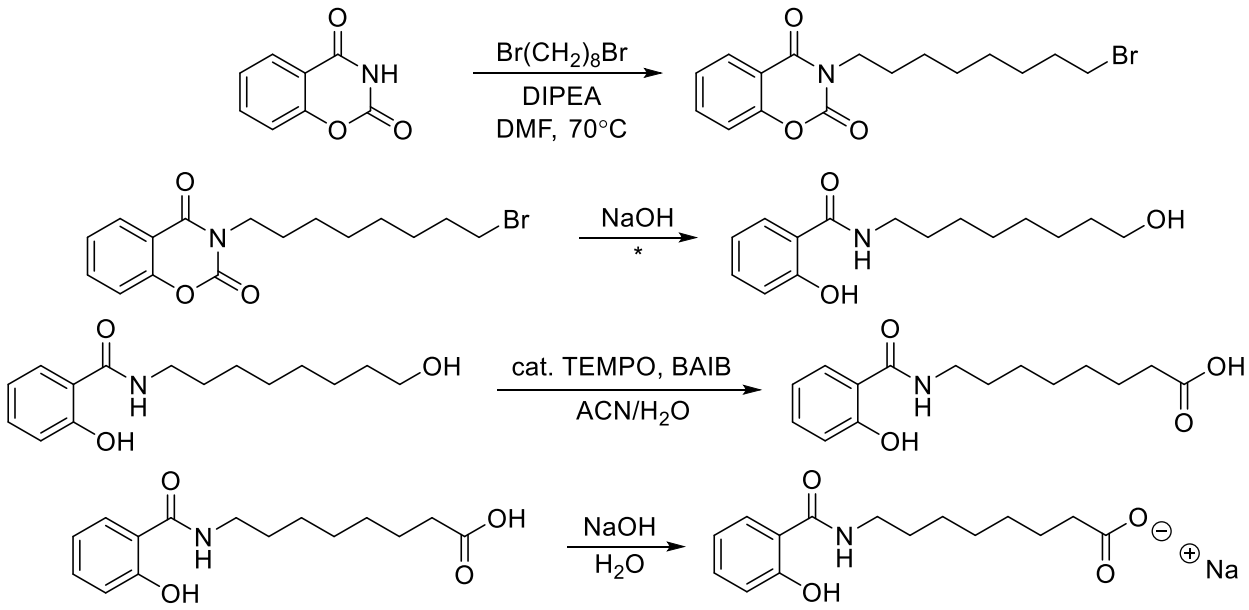

The initial attempted synthetic route to form SNAC is shown above. First, alkylation of the 2H-1,3-benzoxazine-2,4(3H)-dione followed by an S_N2 substitution by sodium hydroxide was attempted. The asterisk indicates that multiple methods were attempted to accomplish S_N2 substitution.

Synthesis of **2**

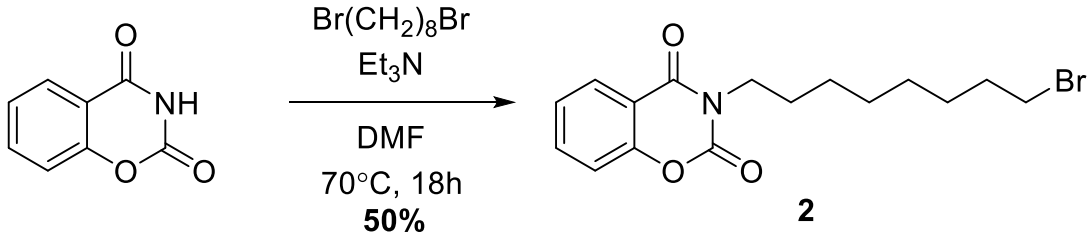

2H-1,3-benzoxazine-2,4(3H)-dione (500 mg, 3.28 mmol, 1.0 eq) and Et_3N (341.2 mg, 3.37 mmol, 1.1 eq) were added to dibromooctane (604 mg, 3.280 mmol, 1.1 eq) dropwise. The reaction flask was heated to 70°C and stirred at reflux for 18h. The reaction mixture was diluted with ethyl acetate and washed with brine (2x50 mL) and NH_4Cl (1x50 50m). The organic layer was extracted, dried over anhydrous sodium sulfate, filtered, and concentrated. The crude product was redissolved in chloroform and purified by silica gel flash column chromatography (10% ethyl acetate in hexanes). The reaction afforded a yield of 50% and the purified product was confirmed by ^{1}H, ^{13}C, and HSQC NMR.

^{1}H NMR ($CDCl_3$, 500 MHz) δ: 7.70 (t, 1H, 8.0 Hz), 7.37 (t, 1H, 7.5 Hz), 7.27 (d, 1H, 5.0 Hz), 4.05 (t, 2H, 7.5 Hz), 3.41 (t, 2H, 7.0 Hz), 1.85 (quint, 2H, 7.5 Hz), 1.75-1.68 (m, 2H), 1.46-1.29 (m, 8H)

^{13}C NMR ($CDCl_3$, 125 MHz) δ: 136.03, 128.10, 125.39, 116.41, 42.68, 33.95, 32.74, 29.00, 28.58, 28.06, 27.48, 26.64

Attempted S_N2 Substitution of **2**

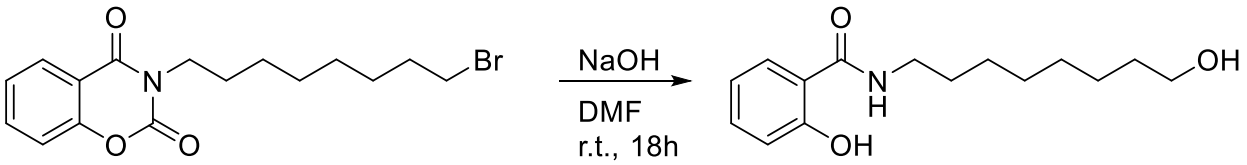

2

2 (150 mg, 0.423 mmol, 1.0 eq) and grounded sodium hydroxide (67.7 mg, 1.69 mmol, 4.0 eq) were dissolved in DMF (1.5 mL) and the reaction was stirred at room temperature for 18h. The reaction mixture was diluted with dichloromethane and washed with ammonium chloride (1x50 mL) and brine (1x50 mL). The organic layer was extracted and dried *in vacuo*. A more polar product was afforded as determined by thin layer chromatography, but the product was unable to be confirmed by ESI-MS.

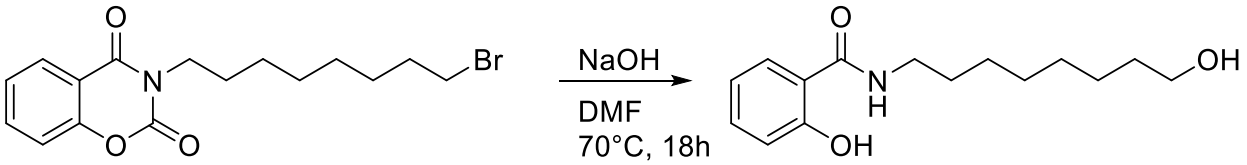

2

2 (150 mg, 0.423 mmol, 1.0 eq) and grounded sodium hydroxide (67.7 mg, 1.69 mmol, 4.0 eq) were dissolved in DMF (1.5 mL) and the reaction was stirred at 70°C for 18h. The reaction mixture was diluted with dichloromethane and washed with ammonium chloride (1x50 mL) and brine (1x50 mL). The organic layer was extracted and dried *in vacuo*. The product was unable to be confirmed. A more polar product was afforded as determined by thin layer chromatography, but the product was unable to be confirmed by ESI-MS.

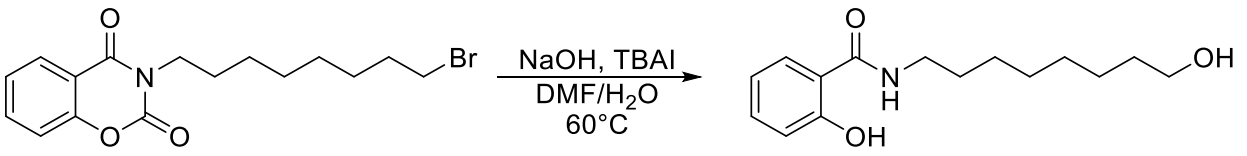

2

In a flame-dried flask, **1** (100 mg, 0.282 mmol, 1.0 eq), TBAI (9.1 mg, 0.0282 mmol, 0.1 eq) and NaOH (101.52 mg, 2.54 mol, 9.0 eq) was dissolved in 5 mL DMF/H_2O (1:1) and heated to 60°C for 14 hours. The reaction mixture was diluted with ethyl acetate and washed twice with brine. The organic layer was isolated and dried over anhydrous Na_2SO_4. The resulting crude mixture was dissolved in chloroform and purified by flash column chromatography with a mobile phase composition of 10% methanol/90% dichloromethane. The product was isolated and characterized by ESI-MS, ^{1}H NMR, ^{13}C NMR, and HSQC NMR. Product was unable to be confirmed by these analytical methods.

Alternative Synthetic Route for SNAC

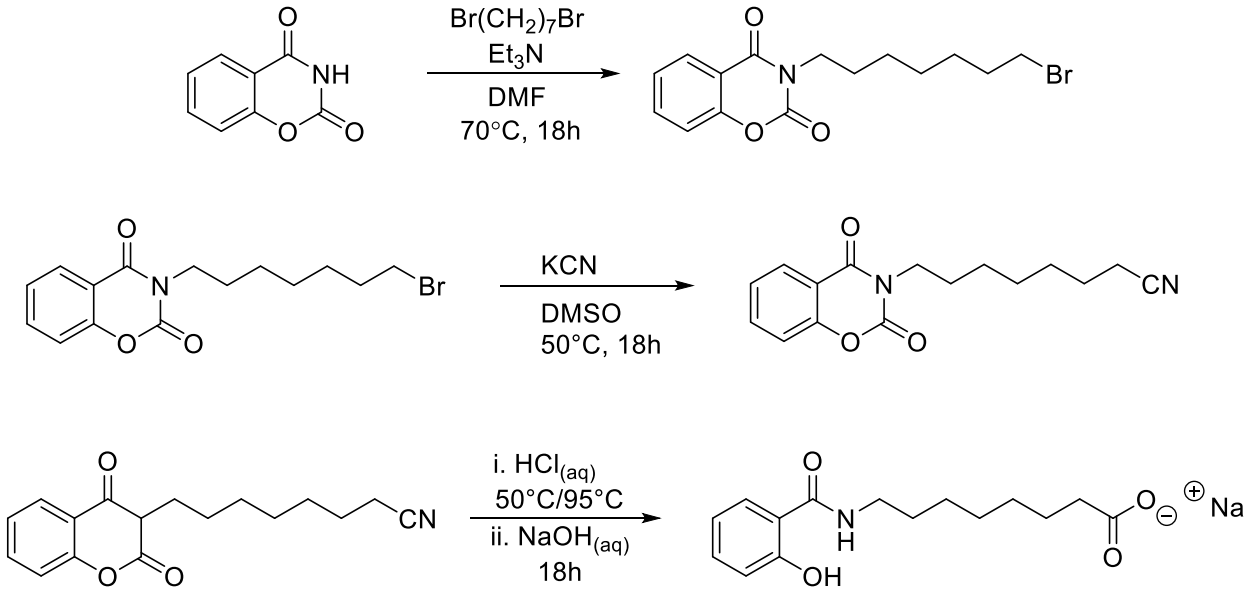

An alternative synthetic route for the synthesis of SNAC is shown above. First, alkylation of the 2H-1,3-benzoxazine-2,4(3H)-dione followed by an S_N2 substitution by potassium cyanide was attempted. After, nitrile hydrolysis followed by precipitation and formation of the SNAC salt was completed.

Synthesis of **3**

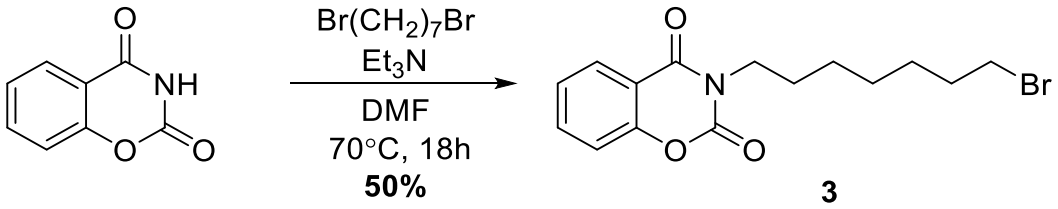

3

2H-1,3-benzoxazine-2,4(3H)-dione (2.00 g, 12.26 mmol, 1.0 eq) and Et_3N (1.37 g, 13.49 mmol, 1.1 eq) were added to dibromoheptane (3.48 g, 13.49 mmol, 1.1 eq) dropwise. The reaction flask was heated to 70°C stirred at reflux for 18h. The reaction mixture was diluted with ethyl acetate and washed with brine (1x50 mL) and ammonium chloride (1x50 mL). The organic layer was extracted, dried over anhydrous sodium sulfate, filtered and concentrated. The crude product was redissolved in chloroform and purified by silica gel flash column chromatography at 10% ethyl acetate in hexanes. The reaction afforded a yield of 50% and the purified product was confirmed by ^{1}H, ^{13}C, and HSQC NMR.

^{1}H NMR ($CDCl_3$, 500 MHz) δ: 7.73 (t, 1H, 8.0 Hz), 7.40 (t, 1H, 7.5 Hz), 7.29 (d, 1H, 5.5 Hz), 4.06 (t, 2H, 7.5 Hz), 3.43 (t, 2H, 6.5 Hz), 1.88 (quint, 2H, 7.5 Hz), 1.78-1.71 (m, 2H), 1.51-1.38 (m, 6H)

^{13}C NMR ($CDCl_3$, 125 MHz) δ: 136.05, 128.11, 125.40, 116.41, 42.62, 33.85, 32.68, 28.36, 28.01, 27.44, 26.58

Synthesis of **4**

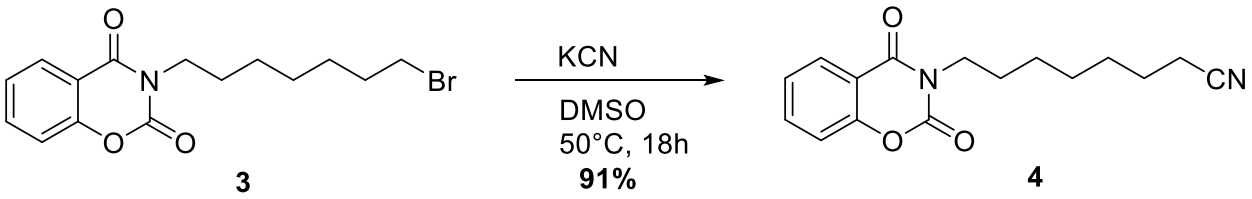

3 **4**

3 (2.00 g, 5.88 mmol, 1.0 eq) and potassium cyanide (766 mg, 11.76 mmol, 2.0 eq) dissolved in 15 mL DMSO and heated to 50°C. The reaction ran for 18h and was subsequently diluted with ethyl acetate. The reaction mixture was washed with brine (2x50 mL), dried over anhydrous sodium sulfate, and dried *in vacuo*. The crude product was purified by silica gel flash column chromatography at 20% ethyl acetate in hexanes. The reaction afforded a yield of 91% and the product was confirmed by ^{1}H, ^{13}C, and HSQC NMR.

^{1}H NMR ($CDCl_3$, 500 MHz) δ: 7.70 (t, 1H, 7.5 Hz), 7.38 (t, 1H, 7.5 Hz), 7.27 (d, 1H, 5.5 Hz), 4.03 (t, 2H, 7.5 Hz), 2.34 (t, 2H, 7.0 Hz), 1.77-1.63 (m, 4H), 1.51-1.37 (m, 6H)

^{13}C NMR ($CDCl_3$, 125 MHz) δ: 136.08, 128.10, 125.43, 116.42, 42.51, 28.51, 28.34, 27.38, 26.41, 25.28, 17.10

Synthesis of **5 (SNAC)**

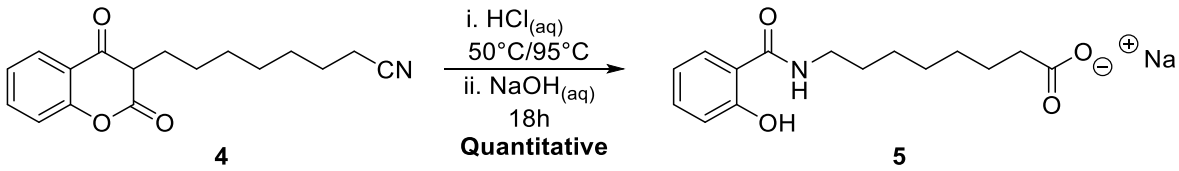

4 **5**

12N hydrochloric acid (4.2 mL) was added to **4** (1.4 g, 4.89 mmol, 1.0 eq) and heated to 50°C. The reaction mixture was stirred for 4h and was heated to 95°C. The reaction mixture was stirred for an additional 4h and filtered using a Buchner funnel. The resulting precipitate was dissolved in 2N sodium hydroxide (4 mL) and stirred for 18h. The reaction mixture was neutralized with 2% hydrochloric acid and an off white solid precipitated. The resulting product mixture was filtered and lyophilized. The reaction afforded quantitative yields. ESI-MS, ^{1}H, ^{13}C, and HSQC NMR confirmed the product.

^{1}H NMR (MeOH, 500 MHz) δ: 7.76 (dd, 1H, J = 1.5 Hz, J = 8.0 Hz), 7.38 (t, 1H, J = 8.0 Hz), 7.27 (m, 2H), 3.40 (t, 2H, 7.0 Hz), 2.31 (t, 2H, 8.0 Hz), 1.69-1.59 (m, 4H), 1.47-1.35 (m, 6H)

^{13}C NMR ($CDCl_3$, 125 MHz) δ: 133.22, 127.34, 118.64, 117.02, 39.09, 33.50, 28.96, 28.73, 28.67, 26.51, 24.60

ESI^{+}: calcd for $C_{15}H_{21}NO_4$ 280.16 [M+H], found 280.27 [M+H]

Chapter 3 Results and Discussion

3.1 Preliminary Stability Experiments

Professor Beinborn of the Tufts Medical Center kindly assayed the JLD-GIP compound for resistance against DPP-4 (Fig. 7). Native GIP showed a potency of 1.5 pM, and after an overnight incubation at 37°C without DPP-4, native GIP also shows a similar potency of 1.7 pM. However, after incubation with DPP-4 at 37°C, the degradation of GIP is evident as the luminescent response to GIP is nullified and the EC50 is substantially reduced. JLD-GIP has a similar, if not higher, potency (1.0 pm) than native GIP. Furthermore, limited degradation of CF_3CH_2-palmitoylated-GIP is seen, and potency is retained. After incubation with DPP-4 at 37°C, the potency of JLD-GIP remains close to non-incubated JLD-GIP (2.0 pM). This data supports the role of the *N*-trifluoroethyl tyrosine in the stability of JLD-GIP. The only other modification is the attachment of a palmitic acid at Q20. Palmitic acid can elicit oligomerization of peptides, but DPP-4 incubations have shown that in the absence of albumin, palmitoylated peptides remain susceptible to DPP-4 cleavage (data not shown). Therefore, *N*-trifluoroethyl tyrosine in GIP confers resistance to DPP-4 cleavage for at least 12h (overnight).

The enhanced stability observed with the *in vitro* studies is further supported by *in vivo* data (Fig. 8). Mice were injected with 1.25 µg subcutaneously to assess the stability of JLD-GIP compared to native GIP. Blood was drawn at either 1 hr or 24hr, and blood

serum was assayed for GIP concentration. JLD-GIP (indicated by FGIP-C16) was shown to substantially increase GIP concentrations at both the 1h and 24h time points, revealing enhanced stability. In addition, albumin is also present in the serum, decreasing renal clearance and increasing serum half-life of GIP. Interestingly, native GIP at both the 1h and 24h time points did not increase serum GIP, implicating rapid degradation of GIP by DPP-4. The concentration of endogenous GIP before and after injection was below the limit of detection, and was approximated to be 50 pM. Using 50 pM as serum level of GIP, the fold increases of GIP are 800- and 80- fold at the 1h, and 24h time point respectively. However, this increase may be higher if the precise endogenous GIP concentration can be determined. In addition, the exact half-life of GIP remains to be ascertained, but the large increases in circulating GIP confirms the therapeutic potential for JLD-GIP.

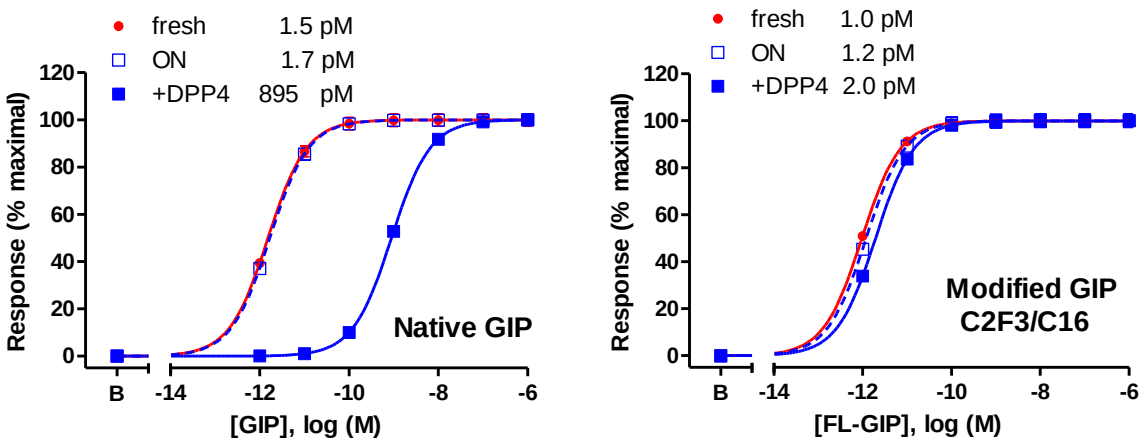

Figure 7. Luciferase assays assessing the potency (EC_{50}) of native GIP vs. JLD-GIP is shown above. Both peptides were incubated overnight at 37°C with or without DPP-4.

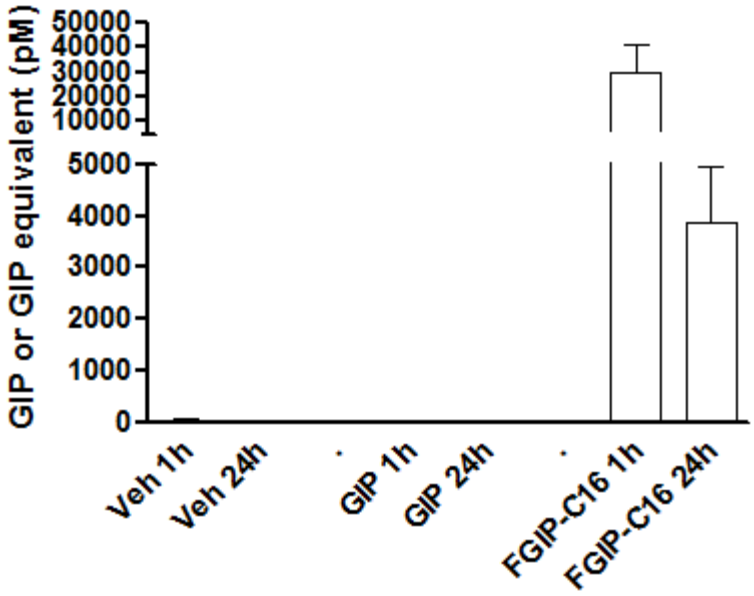

Figure 8. Vehicle (PBS), native unmodified GIP (1.25 µg), and JLD-GIP (1.25 µg) were subcutaneously injected into C57BL/6 mice. Serum GIP in pM was determined at two time points, 1h and 24h.

3.2 Future Directions

The aforementioned data surrounding the stability of JLD-GIP demonstrates the role of *N*-trifluoroethyl in conferring resistance against the serine protease DPP-4 both *in vitro* and *in vivo*. A further comparison study between GIP with exclusively the palmitic acid adduct at K20, and JID-GIP is warranted. In mice serum, albumin is present and thus will prevent rapid clearance by DPP-4. The concentration of JLD-GIP compared to the palmitic acid adduct will establish clearly the role of trifluoroethyl alkylations on stability *in vivo*. Modification of GIP is not limited to K20. There are additional residues that may be of interest for fatty acid acylation. Structural investigations with the ECD of GIPR and helical wheel analysis shows that K16 is a possible candidate for acylation (Figs. 9-10). K16 has the potential to hydrogen bond or form salt bridges with the ECD, but structural analysis of ECD-GIP interactions suggest that this does not occur. Investigating residues that allow modifications such as fatty acid acylation while retaining activity at GIPR will permit distinct modifications of several residues. As such, GIP can have other properties in addition to albumin binding and oligomerization given by the lipid tail. Penchala et al. recently synthesized a small molecule capable of binding to transthyretin, another serum protein in addition to albumin.[115]Attachment of a transthyretin binding molecule as well as a lipid tail will thus prevent renal clearance by binding to transthyretin or albumin. In addition, investigations in the laboratory have been assessing the ability for glycosylated peptides

to cross the blood brain barrier. If glycosylation can improve passage into the brain to mediate anorectic effects, a possible combination between albumin binding through fatty acid acylation and blood brain barrier crossing glycosylation can be accomplished. Interestingly, GIP over-expression increased levels of GIP within the ventromedial nucleus of the hypothalamus in mice and also reduced food intake, suggesting a role for GIP in signaling within the brain.[116] GIP and GLP-1 have been previously shown to exhibit synergy as a unimolecular dual incretin.[117] This co-agonist peptide was superior to existing gold-standard treatments (e.g. liraglutide) in reducing body weight and glycemic levels in diabetic rodents, monkeys, and humans. Thus, the JLD-GIP can be utilized in conjunction with *N*-trifluoroethylated GLP-1 to potentiate anti-diabetic responses. The delivery of GIP and GLP-1 can then be improved by accomplishing oral delivery with SNAC. Here, a developed method for synthesizing SNAC in the lab is shown, and can be utilized for oral delivery for mouse *in vivo* studies by oral gavage administration.

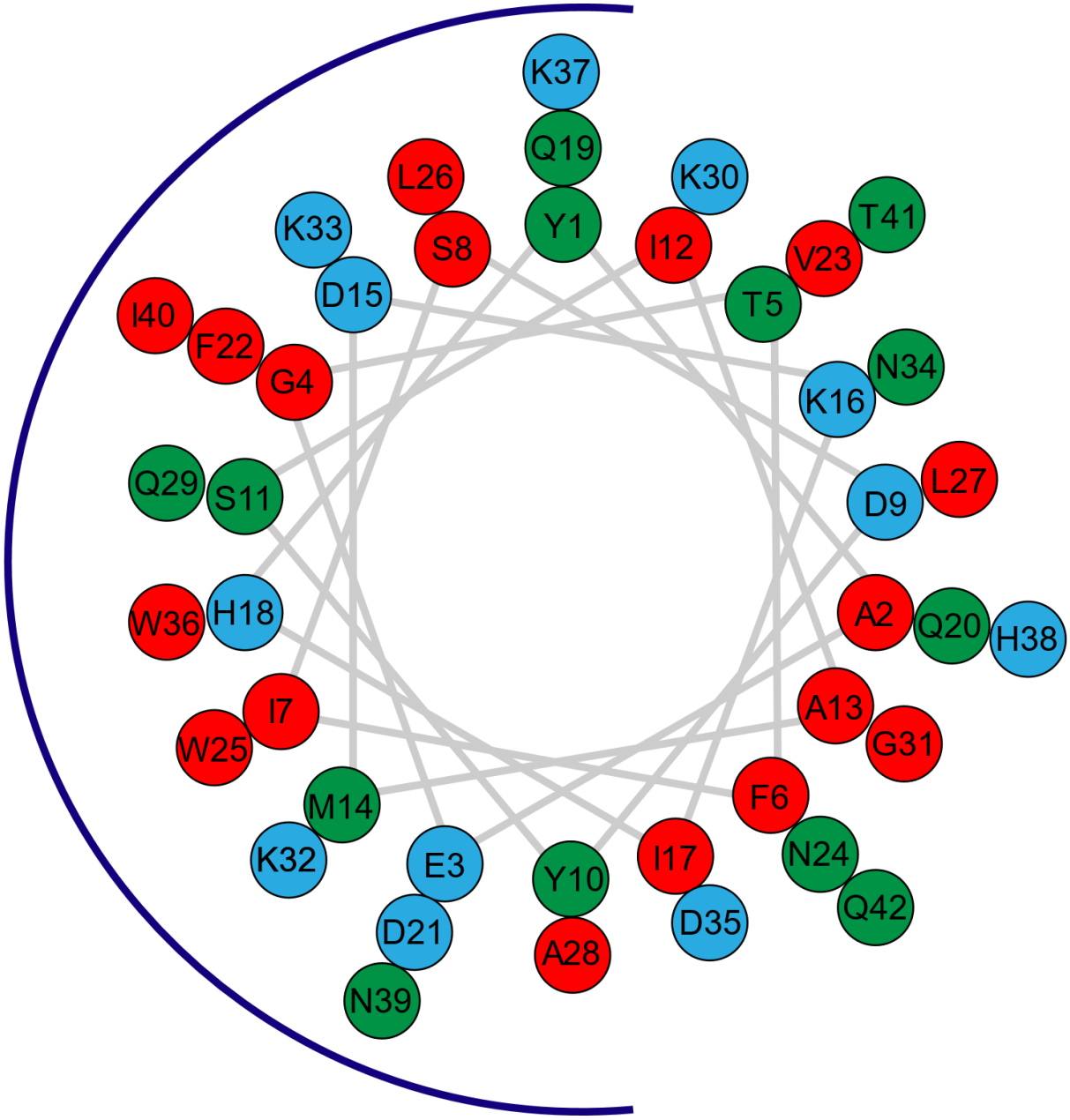

Figure 9. Helical wheel of GIP. The ECD is outlined in a blue arc.

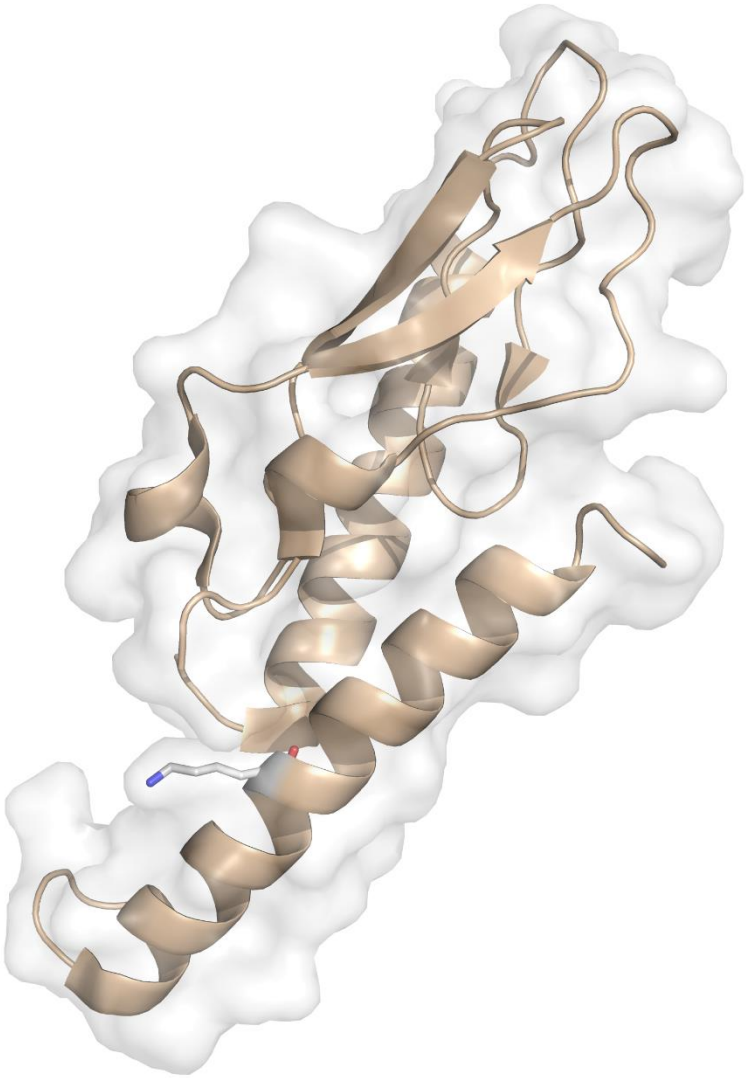

Figure 10. ECD of GIP bound to GIP. K16, a potential residue for modification is shown.

Appendix

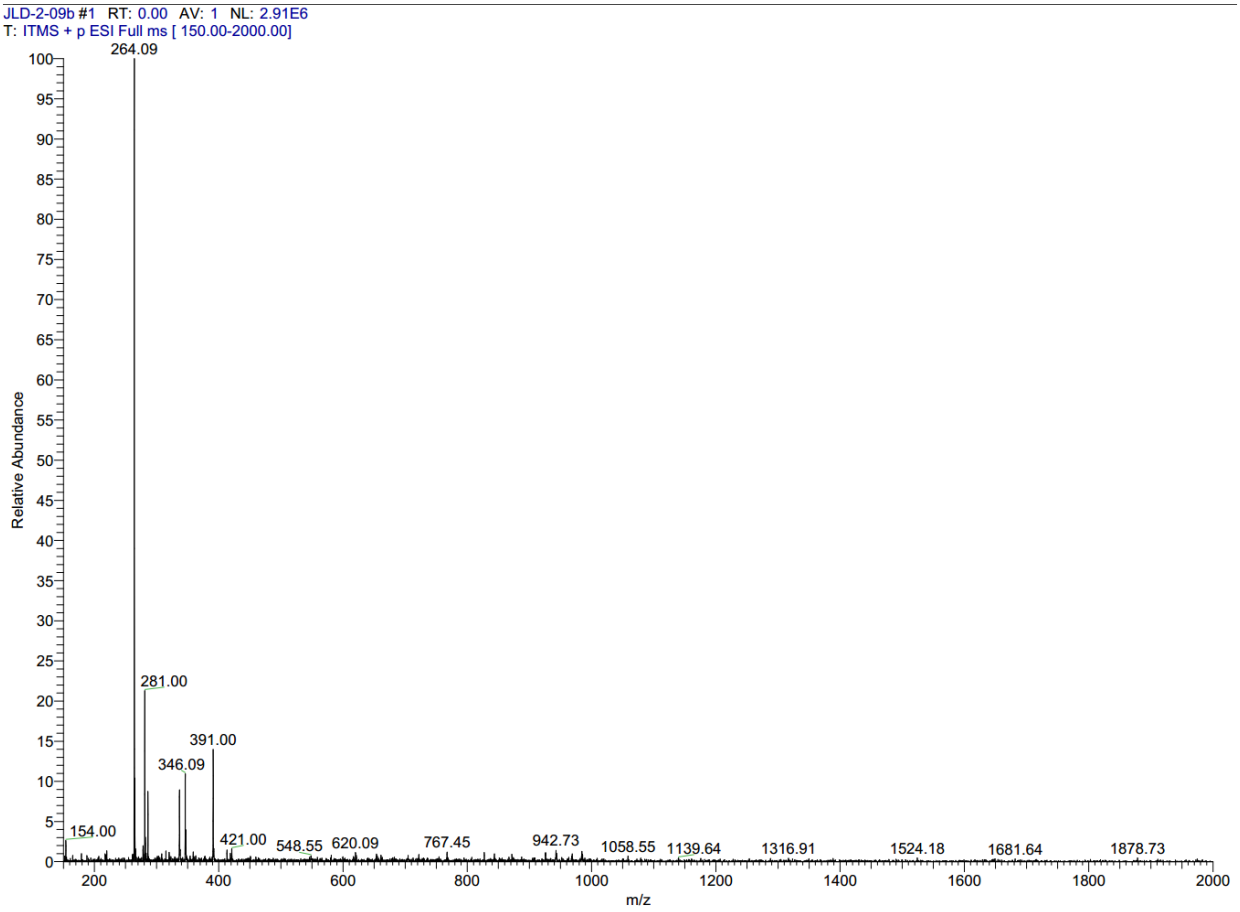

Figure 10. ESI-MS of JLD-GIP.

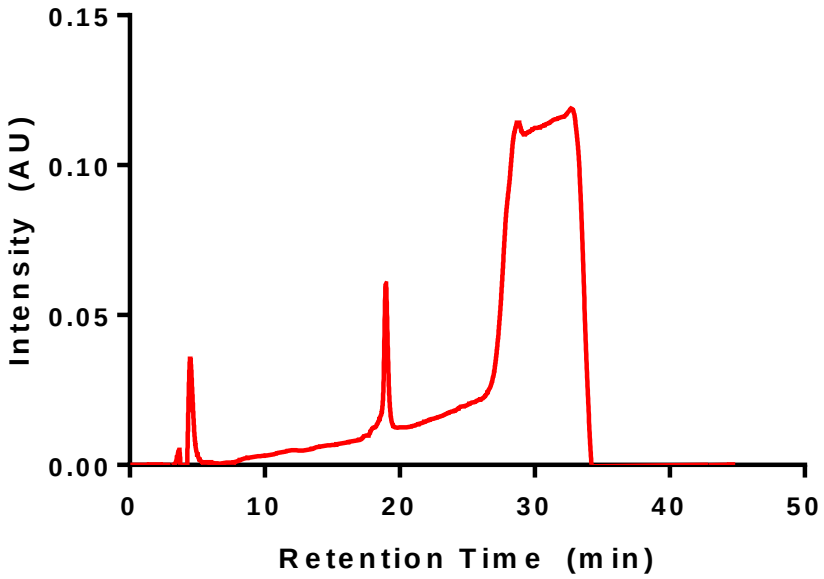

Figure 11. Analytical HPLC of JLD-GIP.

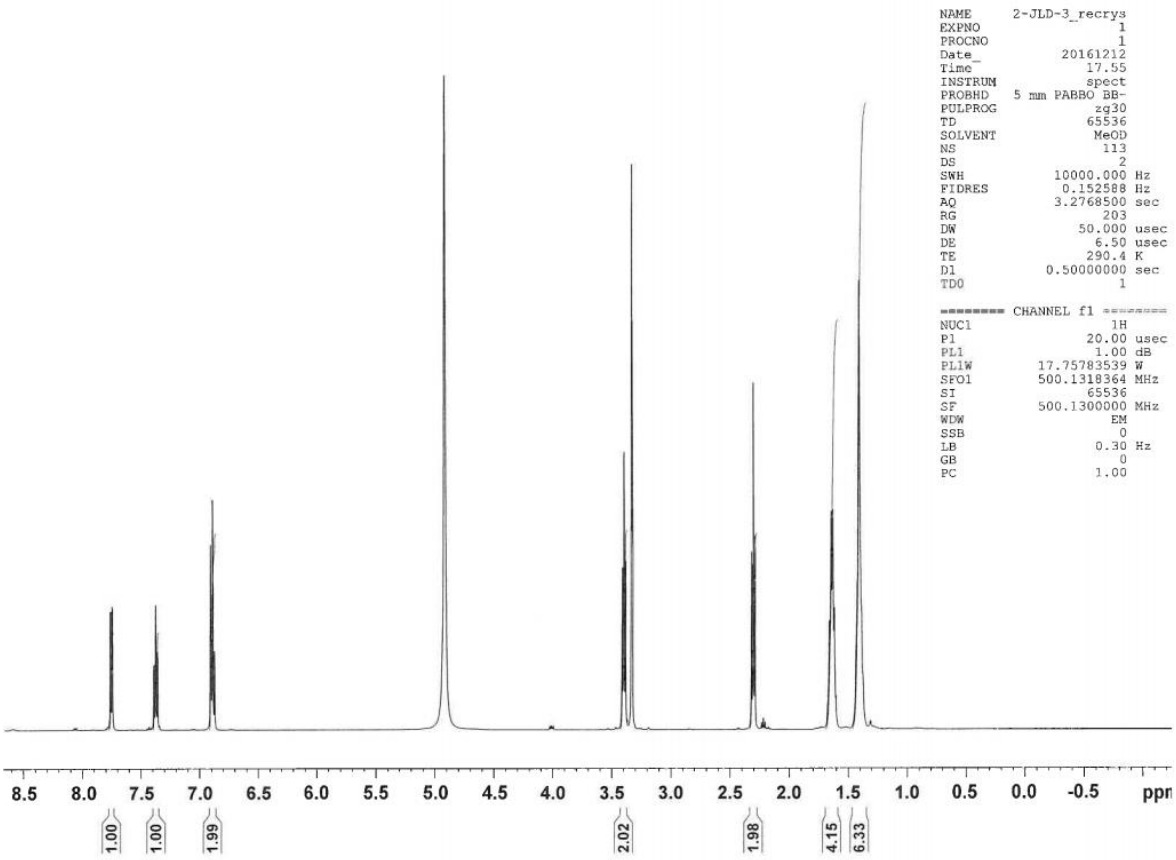

Figure 12. ^{1}H NMR of SNAC.

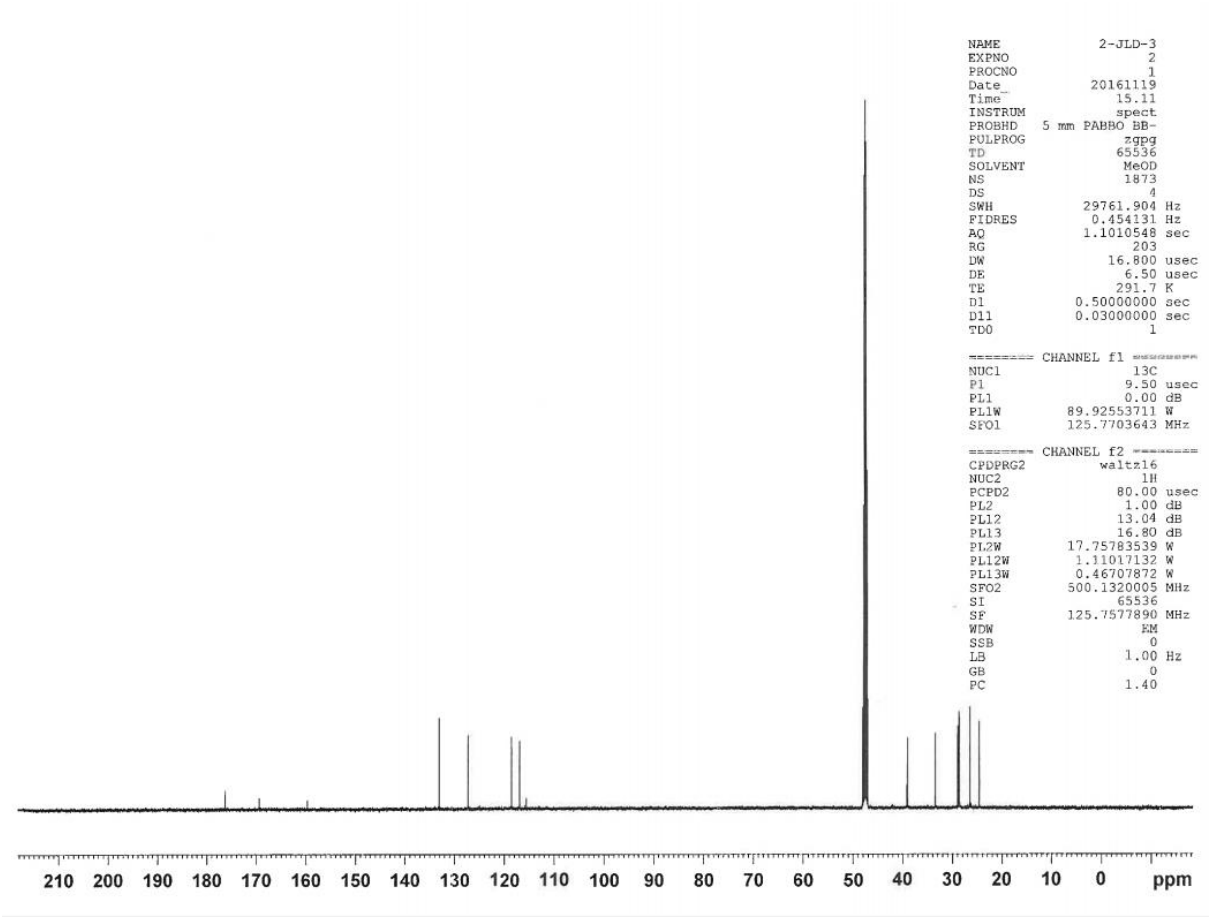

Figure 13. ^{13}C NMR of SNAC.

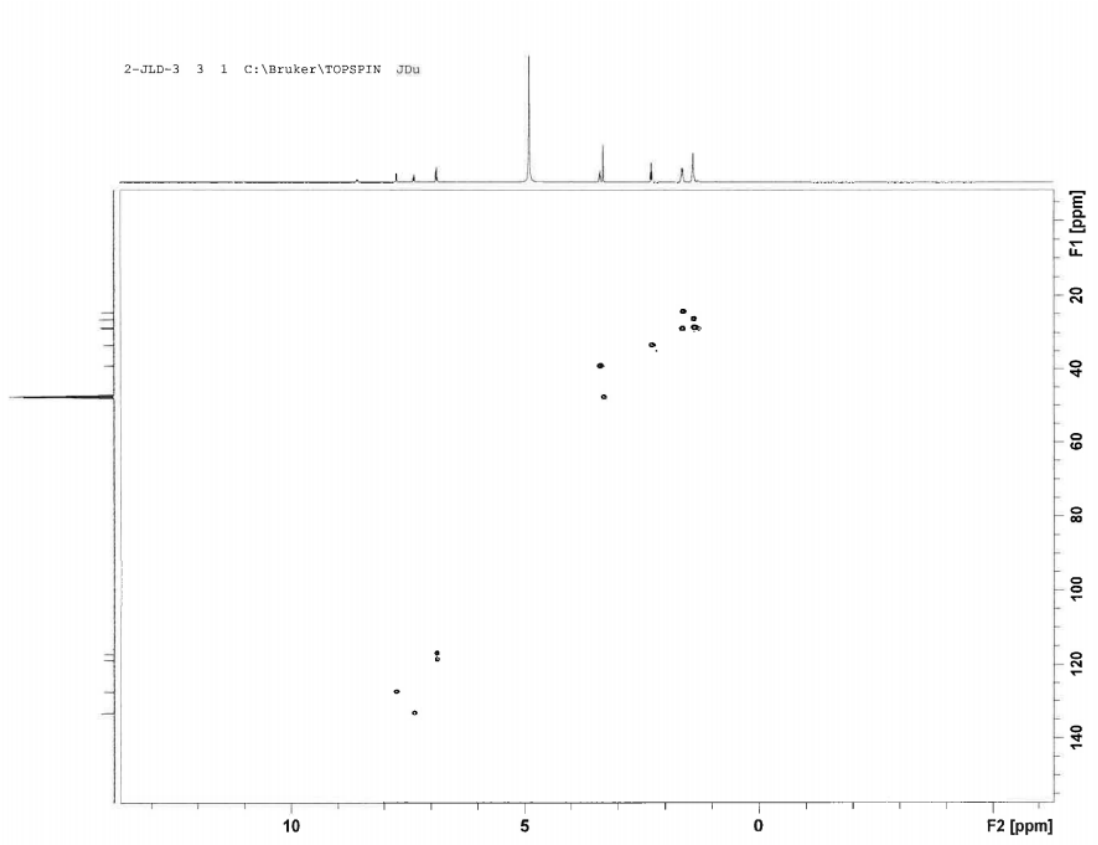

Figure 14. HSQC NMR of SNAC.

References

1. World Health Organization. Global Report on Diabetes. *Isbn* **978,** 88 (2016).
2. Zhou, B. Worldwide trends in diabetes since 1980: a pooled analysis of 751 population-based studies with 4·4 million participants. *Lancet* **387,** 1513–1530 (2016).
3. Deshpande, A. D., Harris-Hayes, M. & Schootman, M. Epidemiology of Diabetes and Diabetes-Related Complications. *Phys. Ther.* **88,** 1254–1264 (2008).
4. Saltiel, A. R. & Kahn, C. R. Insulin signalling and the regulation of glucose and lipid metabolism. *Nature* **414,** 799–806 (2001).
5. Huang, S. & Czech, M. P. The GLUT4 Glucose Transporter. *Cell Metab.* **5,** 237–252 (2007).
6. Aggen, J. B., Nairn, A. C. & Chamberlin, R. Regulation of protein phosphatase-1. *Chem. Biol.* **7,** R13–R23 (2000).
7. Berg, J. M., Tymoczko, J. L. & Stryer, L. *Biochemistry*. *Biochemistry textbook* (W.H. Freeman and Company, 2012).
8. Kono, T., Robinson, F. W. & Sarver, J. A. Insulin-sensitive phosphodiesterase. Its localization, hormonal stimulation, and oxidative stabilization. *J. Biol. Chem.* **250,** 7826–35 (1975).
9. DeFronzo, R. A. From the Triumvirate to the Ominous Octet: A New Paradigm for the Treatment of Type 2 Diabetes Mellitus. *Diabetes* **58,** 773–795 (2009).
10. DeFronzo, R. A., Ferrannini, E. & Simonson, D. C. Fasting hyperglycemia in non-insulin-dependent diabetes mellitus: contributions of excessive hepatic glucose production and impaired tissue glucose uptake. *Metabolism.* **38,** 387–95 (1989).
11. Groop, L. C. *et al.* Glucose and free fatty acid metabolism in non-insulin-dependent diabetes mellitus. Evidence for multiple sites of insulin resistance. *J. Clin. Invest.* **84,** 205–213 (1989).
12. Guilherme, A., Virbasius, J. V., Puri, V. & Czech, M. P. Adipocyte dysfunctions linking obesity to insulin resistance and type 2 diabetes. *Nat. Rev. Mol. Cell Biol.* **9,** 367–377 (2008).
13. Plum, L., Schubert, M. & Brüning, J. C. The role of insulin receptor signaling in the brain. *Trends Endocrinol. Metab.* **16,** 59–65 (2005).
14. Vannucci, S. J. *et al.* GLUT4 glucose transporter expression in rodent brain: effect of diabetes. *Brain Res.* **797,** 1–11 (1998).
15. Pocai, A. *et al.* Hypothalamic KATP channels control hepatic glucose production. *Nature*

434, 1026–1031 (2005).

16. DeFronzo, R. A., Davidson, J. A. & Del Prato, S. The role of the kidneys in glucose homeostasis: a new path towards normalizing glycaemia. *Diabetes, Obes. Metab.* **14,** 5–14 (2012).

17. Gromada, J., Franklin, I. & Wollheim, C. B. α-Cells of the Endocrine Pancreas: 35 Years of Research but the Enigma Remains. *Endocr. Rev.* **28,** 84–116 (2007).

18. Franklin, I., Gromada, J., Gjinovci, A., Theander, S. & Wollheim, C. B. -Cell Secretory Products Activate -Cell ATP-Dependent Potassium Channels to Inhibit Glucagon Release. *Diabetes* **54,** 1808–1815 (2005).

19. Leung, Y. M. *et al.* Insulin Regulates Islet α-Cell Function by Reducing K ATP Channel Sensitivity to Adenosine 5′-Triphosphate Inhibition. *Endocrinology* **147,** 2155–2162 (2006).

20. D'Alessio, D. The role of dysregulated glucagon secretion in type 2 diabetes. *Diabetes, Obes. Metab.* **13,** 126–132 (2011).

21. Gerich, J. E., Langlois, M., Noacco, C., Karam, J. H. & Forsham, P. H. Lack of Glucagon Response to Hypoglycemia in Diabetes: Evidence for an Intrinsic Pancreatic Alpha Cell Defect. *Science (80-.).* **182,** 171–173 (1973).

22. Baron, A. D., Schaeffer, L., Shragg, P. & Kolterman, O. G. Role of hyperglucagonemia in maintenance of increased rates of hepatic glucose output in type II diabetics. *Diabetes* **36,** 274–83 (1987).

23. Liljenquist, J. E. *et al.* Evidence for an important role of glucagon in the regulation of hepatic glucose production in normal man. *J. Clin. Invest.* **59,** 369–74 (1977).

24. Kim, W. & Egan, J. M. The Role of Incretins in Glucose Homeostasis and Diabetes Treatment. *Pharmacol. Rev.* **60,** 470–512 (2008).

25. NAUCK, M. A. *et al.* Incretin Effects of Increasing Glucose Loads in Man Calculated from Venous Insulin and C-Peptide Responses*. *J. Clin. Endocrinol. Metab.* **63,** 492–498 (1986).

26. Meier, J. J. & Nauck, M. A. Is the Diminished Incretin Effect in Type 2 Diabetes Just an Epi-Phenomenon of Impaired -Cell Function? *Diabetes* **59,** 1117–1125 (2010).

27. Holst, J. J. The Physiology of Glucagon-like Peptide 1. *Physiol. Rev.* **87,** 1409–1439 (2007).

28. Rocca, A. S. & Brubaker, P. L. Role of the Vagus Nerve in Mediating Proximal Nutrient-Induced Glucagon-Like Peptide-1 Secretion 1. *Endocrinology* **140,** 1687–1694 (1999).

29. Anini, Y. & Brubaker, P. L. Role of Leptin in the Regulation of Glucagon-Like Peptide-1

Secretion. *Diabetes* **52,** 252–259 (2003).

30. Patzelt, C. & Schiltz, E. Conversion of proglucagon in pancreatic alpha cells: The major endproducts. *Proc. Natl. Acad. Sci. U. S. A.* **81,** 5007–5011 (1984).

31. Rouille, Y., Kantengwa, S., Irminger, J.-C. & Halban, P. A. Role of the Prohormone Convertase PC3 in the Processing of Proglucagon to Glucagon-like Peptide 1. *J. Biol. Chem.* **272,** 32810–32816 (1997).

32. Seino, Y., Fukushima, M. & Yabe, D. GIP and GLP-1, the two incretin hormones: Similarities and differences. *J. Diabetes Investig.* **1,** 8–23 (2010).

33. Baggio, L. L. & Drucker, D. J. Biology of Incretins: GLP-1 and GIP. *Gastroenterology* **132,** 2131–2157 (2007).

34. Ugleholdt, R. *et al.* Prohormone Convertase 1/3 Is Essential for Processing of the Glucose-dependent Insulinotropic Polypeptide Precursor. *J. Biol. Chem.* **281,** 11050–11057 (2006).

35. Thomas, F. B. *et al.* Localization of gastric inhibitory polypeptide release by intestinal glucose perfusion in man. *Gastroenterology* **72,** 49–54 (1977).

36. Brubaker, P. L. & Drucker, D. J. Structure-function of the glucagon receptor family of G protein-coupled receptors: the glucagon, GIP, GLP-1, and GLP-2 receptors. *Receptors Channels* **8,** 179–88 (2002).

37. Hollenstein, K. *et al.* Insights into the structure of class B GPCRs. *Trends Pharmacol. Sci.* **35,** 12–22 (2014).

38. Pal, K., Melcher, K. & Xu, H. E. Structure and mechanism for recognition of peptide hormones by Class B G-protein-coupled receptors. *Acta Pharmacol. Sin.* **33,** 300–311 (2012).

39. Hollenstein, K. *et al.* Structure of class B GPCR corticotropin-releasing factor receptor 1. *Nature* **499,** 438–443 (2013).

40. Siu, F. Y. *et al.* Structure of the human glucagon class B G-protein-coupled receptor. *Nature* **499,** 444–449 (2013).

41. Sun, C. *et al.* Solution structure and mutational analysis of pituitary adenylate cyclase-activating polypeptide binding to the extracellular domain of PAC1-RS. *Proc. Natl. Acad. Sci. U. S. A.* **104,** 7875–80 (2007).

42. Donnelly, D. The structure and function of the glucagon-like peptide-1 receptor and its ligands. *Br. J. Pharmacol.* **166,** 27–41 (2012).

43. Bergwitz, C. *et al.* Full activation of chimeric receptors by hybrids between parathyroid hormone and calcitonin. Evidence for a common pattern of ligand-receptor interaction. *J. Biol. Chem.* **271,** 26469–72 (1996).

44. HOARE, S. Mechanisms of peptide and nonpeptide ligand binding to Class B G-protein-coupled receptors. *Drug Discov. Today* **10,** 417–427 (2005).

45. Schmidtler, J. *et al.* Stimulation of rat parietal cell function by histamine and GLP-1-(7-36) amide is mediated by Gs alpha. *Am. J. Physiol.* **266,** G775-82 (1994).

46. Skoglund, G., Hussain, M. A. & Holz, G. G. Glucagon-like peptide 1 stimulates insulin gene promoter activity by protein kinase A-independent activation of the rat insulin I gene cAMP response element. *Diabetes* **49,** 1156–64 (2000).

47. Light, P. E., Manning Fox, J. E., Riedel, M. J. & Wheeler, M. B. Glucagon-like peptide-1 inhibits pancreatic ATP-sensitive potassium channels via a protein kinase A- and ADP-dependent mechanism. *Mol. Endocrinol.* **16,** 2135–44 (2002).

48. MacDonald, P. E. *et al.* Antagonism of Rat ??-Cell Voltage-dependent K+ Currents by Exendin 4 Requires Dual Activation of the cAMP/Protein Kinase A and Phosphatidylinositol 3-Kinase Signaling Pathways. *J. Biol. Chem.* **278,** 52446–52453 (2003).

49. Ding, W.-G. & Gromada, J. Protein Kinase A-Dependent Stimulation of Exocytosis in Mouse Pancreatic -Cells by Glucose-Dependent Insulinotropic Polypeptide. *Diabetes* **46,** 615–621 (1997).

50. Shibasaki, T. *et al.* Essential role of Epac2/Rap1 signaling in regulation of insulin granule dynamics by cAMP. *Proc. Natl. Acad. Sci. U. S. A.* **104,** 19333–19338 (2007).

51. Leech, C. A. *et al.* Facilitation of β-cell K ATP channel sulfonylurea sensitivity by a cAMP analog selective for the cAMP-regulated guanine nucleotide exchange factor Epac. *Islets* **2,** 72–81 (2010).

52. Chepurny, O. G. *et al.* PKA-dependent potentiation of glucose-stimulated insulin secretion by Epac activator 8-pCPT-2'-O-Me-cAMP-AM in human islets of Langerhans. *AJP Endocrinol. Metab.* **298,** E622–E633 (2010).

53. Fehmann, H. C., Goke, R. & Goke, B. Cell and molecular biology of the incretin hormones glucagon-like peptide- I and glucose-dependent insulin releasing polypeptide. *Endocrine Reviews* **16,** 390–410 (1995).

54. Buteau, J., Foisy, S., Joly, E. & Prentki, M. Glucagon-Like Peptide 1 Induces Pancreatic -Cell Proliferation Via Transactivation of the Epidermal Growth Factor Receptor. *Diabetes* **52,** 124–132 (2003).

55. Buteau, J. GLP-1 receptor signaling: effects on pancreatic β-cell proliferation and survival. *Diabetes Metab.* **34,** S73–S77 (2008).

56. Yabe, D. & Seino, Y. Two incretin hormones GLP-1 and GIP: Comparison of their actions in insulin secretion and ?? cell preservation. *Progress in Biophysics and Molecular Biology*

107, 248–256 (2011).

57. Buteau, J., Spatz, M. L. & Accili, D. Transcription Factor FoxO1 Mediates Glucagon-Like Peptide-1 Effects on Pancreatic -Cell Mass. *Diabetes* **55,** 1190–1196 (2006).

58. Li, Y. *et al.* beta-Cell Pdx1 expression is essential for the glucoregulatory, proliferative, and cytoprotective actions of glucagon-like peptide-1. *Diabetes* **54,** 482–91 (2005).

59. Trümper, A., Trümper, K. & Hörsch, D. Mechanisms of mitogenic and anti-apoptotic signaling by glucose-dependent insulinotropic polypeptide in beta(INS-1)-cells. *J. Endocrinol.* **174,** 233–46 (2002).

60. Hui, H., Nourparvar, A., Zhao, X. & Perfetti, R. Glucagon-Like Peptide-1 Inhibits Apoptosis of Insulin-Secreting Cells via a Cyclic 5′-Adenosine Monophosphate-Dependent Protein Kinase A- and a Phosphatidylinositol 3-Kinase-Dependent Pathway. *Endocrinology* **144,** 1444–1455 (2003).

61. Joly, E. *et al.* Glucagon-like peptide-1 prevents beta cell glucolipotoxicity. *Diabetologia* **47,** 806–815 (2004).

62. Chipuk, J. E., Bouchier-Hayes, L. & Green, D. R. Mitochondrial outer membrane permeabilization during apoptosis: the innocent bystander scenario. *Cell Death Differ.* **13,** 1396–1402 (2006).

63. Imeryüz, N. *et al.* Glucagon-like peptide-1 inhibits gastric emptying via vagal afferent-mediated central mechanisms. *Am. J. Physiol.* **273,** G920-7 (1997).

64. Wettergren, A., Wojdemann, M., Meisner, S., Stadil, F. & Holst, J. J. The inhibitory effect of glucagon-like peptide-1 (GLP-1) 7-36 amide on gastric acid secretion in humans depends on an intact vagal innervation. *Gut* **40,** 597–601 (1997).

65. Sisley, S. *et al.* Neuronal GLP1R mediates liraglutide's anorectic but not glucose-lowering effect. *J. Clin. Invest.* **124,** 2456–2463 (2014).

66. Secher, A. *et al.* The arcuate nucleus mediates GLP-1 receptor agonist liraglutide-dependent weight loss. *J. Clin. Invest.* **124,** 4473–4488 (2014).

67. Osaka, T., Endo, M., Yamakawa, M. & Inoue, S. Energy expenditure by intravenous administration of glucagon-like peptide-1 mediated by the lower brainstem and sympathoadrenal system. *Peptides* **26,** 1623–1631 (2005).

68. Hwa, J. . *et al.* Differential Effects of Intracerebroventricular Glucagon-Like Peptide-1 on Feeding and Energy Expenditure Regulation. *Peptides* **19,** 869–875 (1998).

69. Lockie, S. H. *et al.* Direct Control of Brown Adipose Tissue Thermogenesis by Central Nervous System Glucagon-Like Peptide-1 Receptor Signaling. *Diabetes* **61,** 2753–2762 (2012).

70. Schmidtler, J. *et al.* Rat parietal cell receptors for GLP-1-(7-36) amide: northern blot, cross-linking, and radioligand binding. *Am. J. Physiol.* **267,** G423-32 (1994).

71. López-Delgado, M. I., Morales, M., Villanueva-Peñacarrillo, M. L., Malaisse, W. J. & Valverde, I. Effects of Glucagon-Like Peptide 1 on the Kinetics of Glycogen Synthase a in Hepatocytes from Normal and Diabetic Rats 1. *Endocrinology* **139,** 2811–2817 (1998).

72. Prigeon, R. L., Quddusi, S., Paty, B. & D'Alessio, D. A. Suppression of glucose production by GLP-1 independent of islet hormones: a novel extrapancreatic effect. *Am. J. Physiol. - Endocrinol. Metab.* **285,** E701–E707 (2003).

73. Villanueva-Pe□acarrillo, M. L., Alc□ntara, A. I., Clemente, F., Delgado, E. & Valverde, I. Potent glycogenic effect of GLP-1(7?36)amide in rat skeletal muscle. *Diabetologia* **37,** 1163–1166 (1994).

74. Ding, X., Saxena, N. K., Lin, S., Gupta, N. & Anania, F. A. Exendin-4, a glucagon-like protein-1 (GLP-1) receptor agonist, reverses hepatic steatosis inob/ob mice. *Hepatology* **43,** 173–181 (2006).

75. Nagashima, M. *et al.* Native incretins prevent the development of atherosclerotic lesions in apolipoprotein E knockout mice. *Diabetologia* **54,** 2649–2659 (2011).

76. Arakawa, M. *et al.* Inhibition of Monocyte Adhesion to Endothelial Cells and Attenuation of Atherosclerotic Lesion by a Glucagon-like Peptide-1 Receptor Agonist, Exendin-4. *Diabetes* **59,** 1030–1037 (2010).

77. Ding, L. & Zhang, J. Glucagon-like peptide-1 activates endothelial nitric oxide synthase in human umbilical vein endothelial cells. *Acta Pharmacol. Sin.* **33,** 75–81 (2012).

78. Szecowka, J., Grill, V., Sandberg, E. & Efendic, S. Effect of GIP on the secretion of insulin and somatostatin and the accumulation of cyclic AMP in vitro in the rat. *Eur. J. Endocrinol.* **99,** 416–421 (1982).

79. Kashima, Y. *et al.* Critical Role of cAMP-GEFII{middle dot}Rim2 Complex in Incretin-potentiated Insulin Secretion. *J. Biol. Chem.* **276,** 46046–46053 (2001).

80. Kim, S.-J., Nian, C., Widenmaier, S. & McIntosh, C. H. S. Glucose-Dependent Insulinotropic Polypeptide-Mediated Up-Regulation of -Cell Antiapoptotic Bcl-2 Gene Expression Is Coordinated by Cyclic AMP (cAMP) Response Element Binding Protein (CREB) and cAMP-Responsive CREB Coactivator 2. *Mol. Cell. Biol.* **28,** 1644–1656 (2008).

81. Kim, S. J., Nian, C., Widenmaier, S. & McIntosh, C. H. Glucose-dependent insulinotropic polypeptide-mediated up-regulation of beta-cell antiapoptotic Bcl-2 gene expression is coordinated by cyclic AMP (cAMP) response element binding protein (CREB) and cAMP-responsive CREB coactivator 2. *Mol Cell Biol* **28,** 1644–1656 (2008).

82. Widenmaier, S. B., Ao, Z., Kim, S.-J., Warnock, G. & McIntosh, C. H. S. Suppression of p38 MAPK and JNK via Akt-mediated Inhibition of Apoptosis Signal-regulating Kinase 1 Constitutes a Core Component of the -Cell Pro-survival Effects of Glucose-dependent Insulinotropic Polypeptide. *J. Biol. Chem.* **284,** 30372–30382 (2009).

83. Yang, J. Prevention of Apoptosis by Bcl-2: Release of Cytochrome c from Mitochondria Blocked. *Science (80-.).* **275,** 1129–1132 (1997).

84. Ehses, J. A. Glucose-dependent Insulinotropic Polypeptide Activates the Raf-Mek1/2-ERK1/2 Module via a Cyclic AMP/cAMP-dependent Protein Kinase/Rap1-mediated Pathway. *J. Biol. Chem.* **277,** 37088–37097 (2002).

85. Friedrichsen, B. N. Stimulation of pancreatic -cell replication by incretins involves transcriptional induction of cyclin D1 via multiple signalling pathways. *J. Endocrinol.* **188,** 481–492 (2006).

86. Meier, J. J. *et al.* Gastric inhibitory polypeptide (GIP) dose-dependently stimulates glucagon secretion in healthy human subjects at euglycaemia. *Diabetologia* **46,** 798–801 (2003).

87. Kim, S.-J., Nian, C. & McIntosh, C. H. S. Activation of Lipoprotein Lipase by Glucose-dependent Insulinotropic Polypeptide in Adipocytes: A ROLE FOR A PROTEIN KINASE B, LKB1, AND AMP-ACTIVATED PROTEIN KINASE CASCADE. *J. Biol. Chem.* **282,** 8557–8567 (2007).

88. Miyawaki, K. *et al.* Inhibition of gastric inhibitory polypeptide signaling prevents obesity. *Nat. Med.* **8,** 738–742 (2002).

89. Preitner, F. *et al.* Gluco-incretins control insulin secretion at multiple levels as revealed in mice lacking GLP-1 and GIP receptors. *J. Clin. Invest.* **113,** 635–645 (2004).

90. Zander, M., Madsbad, S., Madsen, J. L. & Holst, J. J. Effect of 6-week course of glucagon-like peptide 1 on glycaemic control, insulin sensitivity, and β-cell function in type 2 diabetes: a parallel-group study. *Lancet* **359,** 824–830 (2002).

91. Meier, J. J. *et al.* Secretion, degradation, and elimination of glucagon-like peptide 1 and gastric inhibitory polypeptide in patients with chronic renal insufficiency and healthy control subjects. *Diabetes* **53,** 654–62 (2004).

92. Röhrborn, D. DPP4 in diabetes. *Front. Immunol.* **6,** (2015).

93. Hansen, L., Deacon, C. F., Ørskov, C. & Holst, J. J. Glucagon-Like Peptide-1-(7–36)Amide Is Transformed to Glucagon-Like Peptide-1-(9–36)Amide by Dipeptidyl Peptidase IV in the Capillaries Supplying the L Cells of the Porcine Intestine 1. *Endocrinology* **140,** 5356–5363 (1999).

94. Rasmussen, H. B., Branner, S., Wiberg, F. C. & Wagtmann, N. Crystal structure of human

dipeptidyl peptidase IV/CD26 in complex with a substrate analog. *Nat. Struct. Biol.* **10,** 19–25 (2003).

95. Abbott, C. A., McCaughan, G. W. & Gorrell, M. D. Two highly conserved glutamic acid residues in the predicted β propeller domain of dipeptidyl peptidase IV are required for its enzyme activity. *FEBS Lett.* **458,** 278–284 (1999).

96. Knudsen, L. B. & Pridal, L. Glucagon-like peptide-1-(9-36) amide is a major metabolite of glucagon-like peptide-1-(7-36) amide after in vivo administration to dogs, and it acts as an antagonist on the pancreatic receptor. *Eur. J. Pharmacol.* **318,** 429–435 (1996).

97. Gault, V. A., Parker, J. C., Harriott, P., Flatt, P. R. & O'Harte, F. P. M. Evidence that the major degradation product of glucose-dependent insulinotropic polypeptide, GIP(3-42), is a GIP receptor antagonist in vivo. *J. Endocrinol.* **175,** 525–33 (2002).

98. Deacon, C. F. Circulation and degradation of GIP and GLP-1. *Horm. Metab. Res.* **36,** 761–765 (2004).

99. Drucker, D. J. & Nauck, M. A. The incretin system: glucagon-like peptide-1 receptor agonists and dipeptidyl peptidase-4 inhibitors in type 2 diabetes. *Lancet* **368,** 1696–1705 (2006).

100. Kim, N.-H., Yu, T. & Lee, D. H. The Nonglycemic Actions of Dipeptidyl Peptidase-4 Inhibitors. *Biomed Res. Int.* **2014,** 1–10 (2014).

101. Knudsen, L. B. *et al.* Potent Derivatives of Glucagon-like Peptide-1 with Pharmacokinetic Properties Suitable for Once Daily Administration. *J. Med. Chem.* **43,** 1664–1669 (2000).

102. BRODERSEN, R., HONORE, B. & ANDERSEN, S. Palmitate binding to serum albumin, measured by rate of dialysis. *Eur. J. Biochem.* **174,** 45–50 (1988).

103. Doweiko, J. & Nompleggi, D. Role of albumin in human physiology and pathophysiology. *J. Parenter. Enter. Nutr.* **15,** 207–211 (1991).

104. Pollaro, L. & Heinis, C. Strategies to prolong the plasma residence time of peptide drugs. *Medchemcomm* **1,** 319 (2010).

105. Frederiksen, T. M. *et al.* Oligomerization of a Glucagon-like Peptide 1 Analog: Bridging Experiment and Simulations. *Biophys. J.* **109,** 1202–1213 (2015).

106. Dharmalingam, M., Sriram, U. & Baruah, M. Liraglutide: A review of its therapeutic use as a once daily GLP-1 analog for the management of type 2 diabetes mellitus. *Indian J. Endocrinol. Metab.* **15,** 9 (2011).

107. Deacon, C. F., Wamberg, S., Bie, P., Hughes, T. E. & Holst, J. J. Preservation of active incretin hormones by inhibition of dipeptidyl peptidase IV suppresses meal-induced incretin secretion in dogs. *J. Endocrinol.* **172,** 355–62 (2002).

108. Rosenstock, J. *et al.* The Fate of Taspoglutide, a Weekly GLP-1 Receptor Agonist, Versus Twice-Daily Exenatide for Type 2 Diabetes: The T-emerge 2 trial. *Diabetes Care* **36,** 498–504 (2013).

109. Siegel, E. G. *et al.* Biological activity of GLP-1-analogues with N-terminal modifications. *Regul. Pept.* **79,** 93–102 (1999).

110. Fosgerau, K. & Hoffmann, T. Peptide therapeutics: Current status and future directions. *Drug Discovery Today* **20,** 122–128 (2015).

111. Kelly, J. R. *et al.* Breaking down the barriers: the gut microbiome, intestinal permeability and stress-related psychiatric disorders. *Front. Cell. Neurosci.* **9,** 392 (2015).

112. Walsh, E. G. *et al.* Oral delivery of macromolecules: rationale underpinning Gastrointestinal Permeation Enhancement Technology (GIPET). *Ther. Deliv.* **2,** 1595–610 (2011).

113. Aungst, B. J. Absorption enhancers: applications and advances. *AAPS J.* **14,** 10–8 (2012).

114. Malkov, D. *et al.* Oral delivery of insulin with the eligen technology: mechanistic studies. *Curr. Drug Deliv.* **2,** 191–7 (2005).

115. Penchala, S. C. *et al.* A biomimetic approach for enhancing the in vivo half-life of peptides. *Nat. Chem. Biol.* **11,** 793–798 (2015).

116. Kim, S.-J. *et al.* GIP-Overexpressing Mice Demonstrate Reduced Diet-Induced Obesity and Steatosis, and Improved Glucose Homeostasis. *PLoS One* **7,** e40156 (2012).

117. Finan, B. *et al.* Unimolecular Dual Incretins Maximize Metabolic Benefits in Rodents, Monkeys, and Humans. *Sci. Transl. Med.* **5,** 209ra151-209ra151 (2013).

Part 2:

Chapter 1: Introduction

1.1 Cardiovascular diseases: Pathophysiology

1.1.1 Atherogenesis

Cardiovascular diseases are currently the leading cause of death for both men and women across the globe.[1] Among those, coronary heart disease (CHD), marked by atherosclerosis, is the most prominent cardiovascular disease. Chronic inflammation serves as the hallmark for atherosclerosis. This chronic inflammation originates from pro-inflammatory and atherogenic stimuli such as hyperlipidemia and hypertension.[2] The most vulnerable sites lesion initiation occurs among areas of arterial branching, due to irregular blood flow, leading to low sheer stress.[3,4] A dysfunctional endothelial cell emerges, adopting a non-uniform morphology that allows the accumulation, aggregation, and oxidation of low density lipoproteins (LDLs) within the arterial wall, initiating atherogenesis.

1.1.2 Endothelial Cell Dysfunction and Arterial Wall Remodeling

Endothelial cell (EC) dysfunction mediates many atherogenic effects including activation of several molecular pathways and propagation of a pro-inflammatory response. Normally, endothelial cells express endothelial nitric oxide synthase (eNOS) that produces nitric oxide (NO) from the conversion of L-arginine to L-citrulline.[5,6] NO has a variety of observed effects in humans but is a crucial mediator in atherosclerotic lesion progression.

NO is responsible for vasodilation by binding to its receptor, soluble guanylyl cyclase, in the cytosol of smooth muscle cells to convert guanosine 5′-triphosphate (GTP) to cyclic guanosine 3′,5′-monophosphate (cGMP).[7] cGMP acts through the cGMP-dependent protein kinase to phosphorylate inositol 1,4,5-triphosphate receptor, releasing Ca^{2+} stores within the endoplasmic reticulum to initiate smooth muscle cell relaxation and vasodilation.[8] However, in atherosclerosis, increased levels of oxidized LDLs and C-reactive protein contribute to attenuated NO signaling and NO production.[9] Interestingly, reduced levels of the catalyst tetrahydrobiopterin in addition to increased superoxide production leads to eNOS uncoupling.[9,10] eNOS uncoupling transforms the nitric oxide producing enzyme to a reactive oxygen species producing enzyme contributing to endothelial cell dysfunction and atherosclerotic lesion progression.[11]

ECs directly participate in leukocyte recruitment, and in response to mechanical forces and cardiovascular risk factors, express multiple selectins that initiate capture, tethering, and rolling of leukocytes.[6] The recruitment of leukocytes, particularly monocytes, is further supported by the secretion of chemokines by ECs. Chemokines such as CCL2 and CCL5 bind to their respective receptors CCR2 and CCR5 to recruit monocytes along the chemokine concentration gradient (chemotaxis) to the site of atherosclerotic plaques.[12] This subsequently leads to monocyte-endothelial cell adhesion and extravasation into the intima. Retention of oxidized lipoproteins as well as aggregation of these lipoproteins elicits

a proinflammatory environment that promotes monocyte differentiation into macrophages.[12] Macrophages mediate lipoprotein uptake through their scavenger receptors (e.g. LOX-1, CD36), but due to massive increased uptake of lipids, these macrophages transform into lipid-laden foam cells.[13] The inflammatory pathways of these foam cells are activated and further exacerbates lesion progression. Indeed, oxLDLs activate several toll-like receptors, and phagocytosis of cholesterol crystals activate the inflammasome in macrophages.[14] Consequently, pro-inflammatory cytokines and chemokines such as IL-1β and MCP-1 are secreted, maintaining an inflammatory environment while recruiting more monocytes into the lesion.[15] These foam cells are eventually subjected to apoptosis, namely through endoplasmic reticulum (ER) stress and the unfolded protein response (UPR).[16] Concurrently, smooth muscle cells (SMCs) emerge, proliferate, and aggregate, initiating formation of the fibrous cap.[17] These smooth muscle cells are responsible for secretion of collagen, elastin, and other ECM proteins to establish the fibrous, atherosclerotic plaque.[17]

1.1.3 Plaque Progression and Rupture

In order to resolve early lesions, apoptotic cell clearance by other phagocytes, known as efferocytosis is necessary. However, in late atheroma, efferocytosis becomes defective, promoting apoptotic macrophages to secondary necrosis and forming the necrotic core.[18] The necrotic core is especially pernicious as the macrophage debris,

mostly lipids, contributes to inflammation and more notably the thinning of the fibrous cap.[19] This renders the atherosclerotic lesion a vulnerable plaque and at risk of rupture, which can lead to thrombosis and other acute coronary events.

1.2 Women and Cardiovascular Disease

1.2.1 Pre-menopausal Women vs. Post-menopausal Women

Between men and women, women generally develop atherosclerosis much later than men, about seven to ten years. Indeed, prevalence of CVD in women is like that of men below the age of 40, but at 60, more women than men are affected.[20] Further, when cardiovascular disease does appear in women, associated risk factors such as diabetes and hypertension are more widely observed.[21,22] The delayed progression of cardiovascular disease and manifestation of risk factors are mainly attributed to menopause. Body weight of women significantly increases post-menopause, subjecting them to obesity and type II diabetes (T2D). T2D doubles their CVD mortality risk when compared to men.[22] In addition to a higher prevalence of hypertension among women with CVD, hypercholesterolemia as total cholesterol, LDL, and lipoprotein a levels all significantly increase after menopause.[23] Post-menopause, women lose their ability to secrete the steroid hormones progesterone and estrogen and thus experience symptoms such as hot flushes.[24]

1.2.2 Hormone Replacement Therapy and the Timing Hypothesis

The atherosclerotic consequences of menopause lead scientists to investigate the use of hormone replacement therapy (HRT), namely with estrogen, and examine its capability of reducing CVD risk. The Nurses' Health Study became both a landmark and controversial study. Both the four-year and ten-year follow-up indicated that HRT with estrogen reduces CVD risk, with the ten-year follow-up showing a 50% risk reduction.[25,26] However, the Framingham Heart study produced opposing results and observed that estrogen HRT did not reduce CVD risk but perhaps increases risk instead.[27] The Women's Health Initiative (WHI) study, also supported the non-significant effects of estrogen HRT and suggested the risk of increasing cancer prevalence in those undergoing HRT, a legitimate concern.[28] Breast cancer and endometrial (uterine) cancer are both linked to estrogen receptor (ER) signaling, and ER is utilized as a biomarker for progression of either disease.[29]

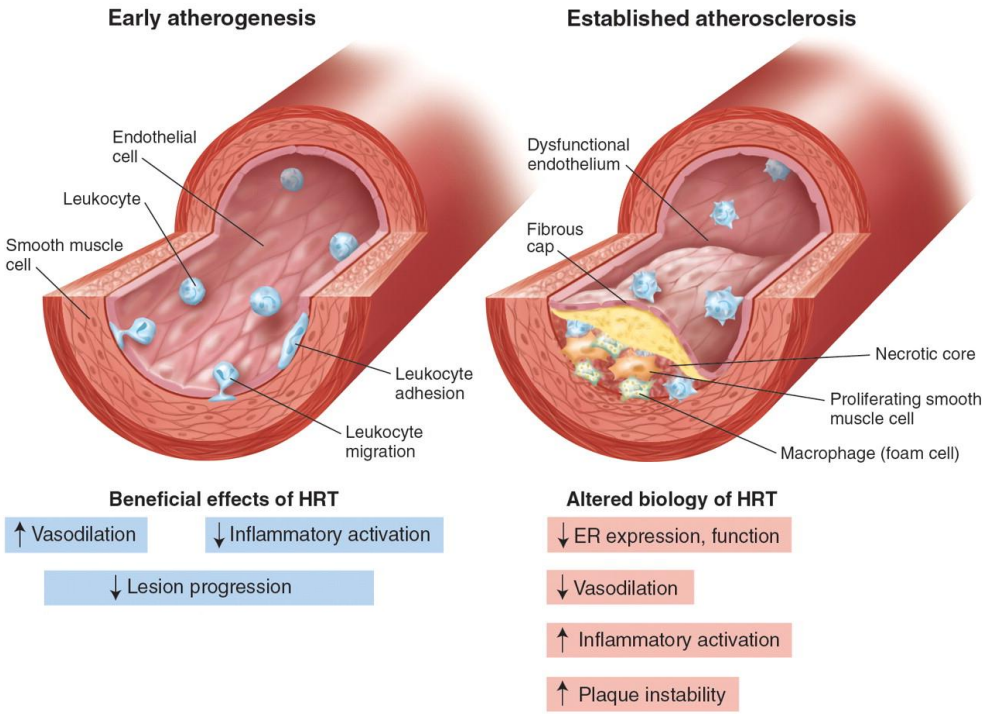

Figure 9. Timing hypothesis of estrogen hormone replacement therapy. In early menopause, atherosclerosis is still in the early stages, allowing for beneficial effects. In established atherosclerosis, ER expression is reduced, diminishing any beneficial effects. Adapted from Mendelsohn and Karas, 2005.[92] Reprinted with permission from Science/AAAS.

Yet, a confounding factor that the WHI study did not address was age. Subsequent meta-analysis of hormone replacement therapy data indicated that in younger post-menopausal women, HRT reduced the risk of CVD and related events.[30,31] Studies such as these developed into the timing hypothesis. Essentially, CVD protective effects of HRT depends on the timing of initiation, and estrogen affects the vasculature environment differently, depending on the progression of atherosclerosis (Fig. 1). The WHI study observed women who averaged 10 years past menopause, when atherosclerosis has already been well developed. Post-menopausal women who have established, advanced atherosclerotic plaques are not subjected to the beneficial effects of estrogen, and thus a

reduction of CVD risk was not seen. Various animal model and primate studies suggest that when HRT is initiated before the progression to advanced atheroma, reduction of CVD risk can be accomplished.[32,33] The Early versus Late Intervention Trial with Estradiol (ELITE) specifically investigated this timing hypothesis and examined atherosclerotic progression in both early and late menopausal women receiving estrogen containing HRT.[34] Progression of atherosclerosis advanced at a much slower rate than the placebo when HRT was initiated in early menopausal women, but not when HRT was initiated in late menopausal women.

1.3 Estrogen Origin and Function

1.3.1 Biosynthesis of Estrogens

The use of estrogen containing HRT clearly establishes the role of estrogen signaling at the estrogen receptor in atherosclerotic progression. Estrogen is naturally produced in three forms estrone (E1), estradiol (E2), and estriol (E3). Production of estrogen is mainly carried out in the ovaries, but studies have demonstrated production in auxiliary organs such as the liver, brain, and heart.[35] E2, the most potent and most widely

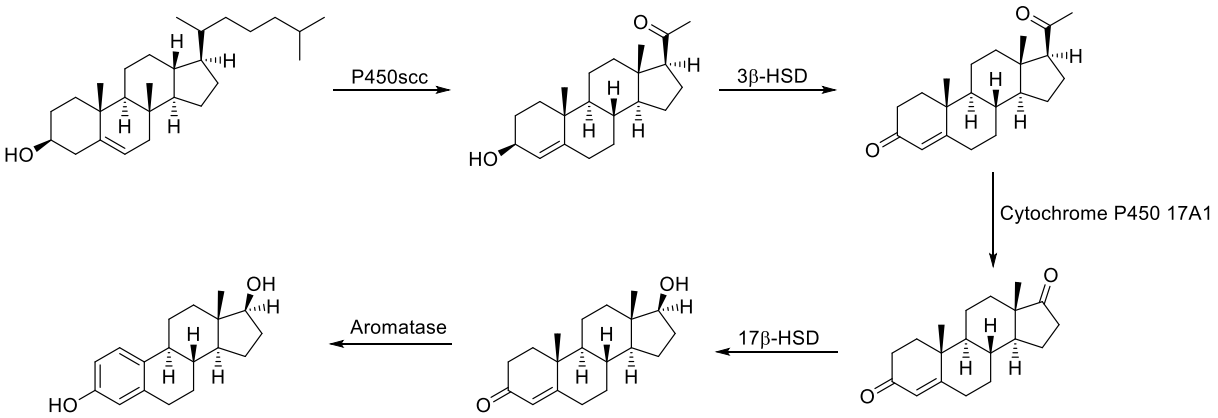

Figure 10. Biosynthesis of estradiol. Estradiol synthesis occurs in the ovaries, liver, brain, and heart.

produced estrogen that utilizes cholesterol as its starting point.[36] Cholesterol side-chain cleavage enzyme (P450scc) initially oxidizes and cleaves cholesterol to produce pregnenolone (Fig. 2). 3β-Hydroxysteroid dehydrogenase (3β-HSD) then oxidizes the hydroxyl at the 3rd position of pregnenolone to produce progesterone. Cytochrome P450 17A1 and 17β-HSD subsequently oxidize progesterone to produce testosterone which is then aromatized by aromatase to produce E2.

1.3.2 Estrogen Receptor Structure

Estrogen receptor (ER) is crucial for the activation of several signal transduction pathways, is widely expressed in various tissues, and its plethora of classes variants, and isoforms are implicated in several diseases. There are two types of ER, ERα and ERβ, and is encoded by *ESR1* and *ESR2*, each on separate chromosomes.[37] ER consists of a N-terminal domain, a DNA-binding domain, a ligand-binding domain, and a hinge domain.[38]

At the N-terminus and the ligand binding domain are activation function 1 (AF-1) and AF-2, respectively. Both AF-1 and AF-2 recruit protein complexes after ER binds to DNA, to regulate transcriptional activation.[39,40] AF-1 also poses as a differentiating point between the two isoforms α/β. AF-1 has been shown to recruit the TATA-binding protein in ERα, enhancing transcription.[41] In ERβ, such recruitment is unobserved. This results in differences in coregulatory protein recruitment and regulation of gene expression.

The ligand-binding domain contains a large hydrophobic core, allowing for E2 to bury itself in, and that low energy conformation is further stabilized by hydrogen bonding at the 3rd and 17th position (phenol/hydroxyl) of E2.[42] Upon binding of E2 to the ligand-binding domain, helix 12 forms a lid-like shape over the helices that surround and interact with E2. The conformational change involving helix 12 allows for AF-2 to become exposed, indicating the ligand-dependent activation of AF-2. AF-2 recruits p160 coactivators allowing for protein complexes to form upon DNA binding of ER.[43] Further, the hinge region of ER undergoes conformational change to link the DNA-binding domain and the ligand-binding domain.

The DNA-binding domain prior to nuclear translocation, utilizes its two zinc fingers comprised of eight total cysteine residues coordinated with two Zn^{2+} ions, forming two tetrahedral coordination networks.[44] One of the zinc fingers contains a cluster of residues that compose the “D box”, which is essential for dimerization of ER.[44] The “D box”

cooperates with the ligand binding domain, allowing for both hetero and homodimerization with an estimated K_d of 2-3 nM.[45] Following nuclear entrance of the dimerized ER, a cluster of residues on the other zinc finger known as the "P box" is responsible for DNA binding, and thus dimerized ER binds to DNA in two locations.[46]

1.3.3 Classical Estrogen Receptor Signaling

Classical ER signaling involves nuclear ER directly binding to DNA and regulating gene expression (Fig. 3). The transcription of atheroprotective genes after nuclear ER binding in the vasculature is dependent on the role of coregulatory proteins. For instance, steroid receptor co-activator 3 (SRC-3) is a strong coactivator of ER, allowing upregulation of ER targeted genes specifically in vascular smooth muscle cells (VSMCs) and ECs. In *Src3*$^{-/-}$ mice, VSMCs and ECs were unable to prevent neointima formation.[47] Thus, the estrogen mediated atheroprotective effects is dependent on coregulation machinery for effective transcription of ER targeted genes. The downstream effects of ER signaling are far-reaching. Genomic signaling contributes to vasodilation through the upregulation of vasodilatory enzymes such as inducible nitric oxide synthase (iNOS) in VSMCs, eNOS in ECs, and prostacyclin synthase.[48,49] In response to atherosclerosis progression and vascular injury, estrogen mediates an increased expression of vascular endothelial growth factor (VEGF).[49] VEGF aids in maintaining endothelial cell layer integrity through nitric oxide and prostacyclin production that may facilitate inhibition of smooth muscle cell

growth.[50] ECM-related proteins such as collagen and matrix metalloproteinase 2, as well as cell adhesion proteins such as E-selectin are regulated by estrogen-mediated genomic signaling presenting the role of estrogen in remodeling the extracellular matrix and modulating inflammation.[49,51,52] Further, TGF-β, EGFR, platelet-derived growth factor, and flt-4 tyrosine kinase are influenced by estrogen signaling, supporting estrogen's role in vascular injury recovery and angiogenesis.[48,53,54] Interestingly, systemic effects such as lower LDL and lipoprotein a concentrations are also partly mediated by estrogen-mediated genomic signaling.[55]

1.3.4 Rapid Signaling Pathway

In the 1970s, researchers discovered a novel binding mechanism of estrogen, that is, binding and signaling at the plasma membrane.[56] Two decades later, a rapid signaling pathway for this membrane estrogen receptor (mER) was uncovered.[57,58] Assessment of the downstream effects uncovered that mER was responsible for the induction of nitric oxide, particularly within endothelial cells, and mediates these effects within 15-30 minutes (Fig. 3).[57] Surprisingly, some effects such as elevation in cAMP levels can occur in as little as 15 seconds.[59] Interestingly, in ERα-knockout mice, the vasodilatory effects of nitric oxide were reversed, establishing the nature of mER as a variant of ERα.[60,61] To mediate nitric oxide release and vasodilation, mER releases its associated G-proteins Gαi and Gβγ

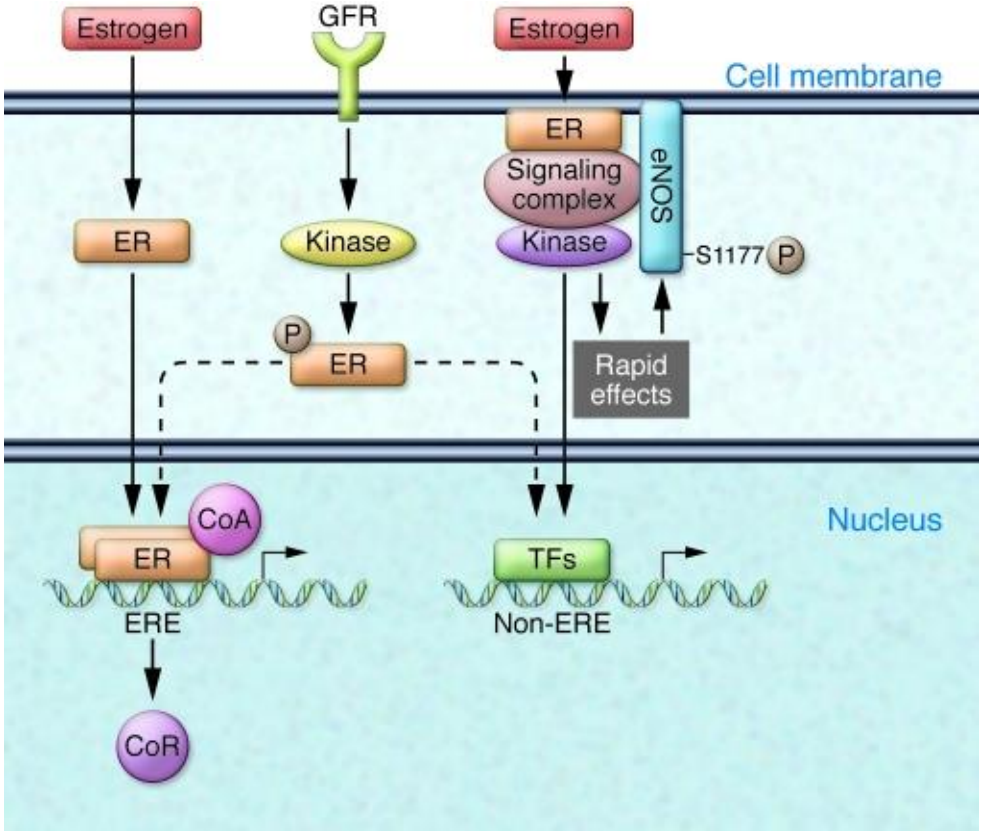

Figure 11. E2 can function by eliciting either the classical nuclear ER pathway or the rapid signaling pathway as indicated. GFR cross-talk also occurs, though further elucidation is necessary for the exact effects in cardiovascular disease. Reprinted from Mendelsohn and Karas, 2010 with permission.[60]

following estrogen binding, allowing Gαi to activate c-Src, a kinase that phosphorylates phosphoinositide 3-kinase (PI3K).[62,63] PI3K is critical, as the PI3K/Akt pathway is elicited, leading to phosphorylation of eNOS at Ser1177, amplifying nitric oxide production by the endothelial cell.[64,65] Vasodilation in CVD relieves hypertension and shear stress, inhibiting progression of atherosclerosis.[66] In addition to vasodilation, inhibition of VSMC growth and migration and leukocyte adhesion are additional properties of nitric oxide, implicating its role in ECM modeling and inflammation.[67] In addition to the rapid signaling pathway, mER

is implicated in transcriptional activation, and has been seen to induce cyclin D_1 transcription.[68,69]

1.3.5 Estrogen Receptor Cross-talk

Estrogen receptor need not be directly activated by estrogen to confer atheroprotective effects. Vascular cells participate in estrogen-independent signaling via growth factor receptors such as EGFR eliciting the MAPK cascade and directly activating ERα (Fig. 3). After phosphorylation at key serine residues 104 and 106 by the MAPK cascade, ERα contributes to estrogen-independent signaling.[60,70] Interestingly, upon binding to ERα, estrogen can mediate EGFR signaling through receptor transactivation, revealing cross-talk between the receptors.[71] Cross-talk has also been investigated in mediating against tamoxifen resistance in breast cancer. MCF-7 and Cos-1 cells, transiently transfected to express ER, have shown ERα activation in a ligand independent manner.[72] PI3K and AKT activation through growth factors such as EGF were sufficient to activate ERα and mediate proliferative effects. Thus, tamoxifen, which normally inhibits ERα, is rendered ineffective, as estrogen independent effects can result in cell proliferation. In addition, mER itself can participate in ER cross-talk. Filardo et al. revealed that estrogen signaling at the plasma membrane can stimulate EGFR signaling by inducing heparin bound EGF release, and subsequent activation by EGF.[73] By this mechanism,

extracellular signal-related kinase (Erk)-1 and Erk-2 are activated to mediate cell proliferation. In contrast, mER can inhibit Erk activation through a distinct pathway.[74] By activating adenylyl cyclase, stimulation of cAMP production occurs, and the protooncogene Raf-1 is inactivated, preventing Erk activation.

1.3.6 Current Approaches to Selective Targeting

The discovery of mER and the rapid signaling pathway stimulated intense scientific attention to the field and researchers have developed strategies to target mER for the treatment of CVD. Estrogen containing HRT, as explained earlier, poses a major health risk if used to treat CVD, as widespread proliferation in the breast or uterine tissues may ensue. However, since mER operates mainly through the rapid signaling pathway, it may be particularly advantageous to target this receptor. Indeed, Katzenellenbogen and coworkers pursued this strategy and developed estrogen dendrimer conjugates (EDCs). EDCs are large macromolecules that are synthesized through global reductive amination of modified E2 to a poly(amido)amine (PAMAM) dendrimer.[75] In their study, Chambliss et al. used a Generation 6 dendrimer with 256 available amines and a molecular weight of 58,048, which was then coupled to E2. Interestingly, in mice, these EDCs were unable to penetrate the plasma membrane and instead specifically targeted the mER for cardiovascular protection. Targeting at the mER promoted endothelial cell proliferation and migration as well as enhanced monolayer integrity. Gap formation and other injuries

to the endothelial layer are a result of sheer stress and contribute to atherosclerotic lesion and plaque progression, yet rescue of the endothelial layer can be accomplished through the action of selective activation of mER. Further, neointima formation is attenuated in *Apoe*$^{-/-}$ mice treated with EDCs, displaying mER role in preventing coronary occlusion. Importantly, these atherprotective outcomes were not coupled with uterotrophic or oncogenic responses. EDCs prevented uterine growth in ovariectomized female mice as well as tumor growth in MCF cell tumor xenografts of SCID mice. In comparison, treatment with E2 resulted in 7-fold increase in uterine size and promoted tumor growth. By selectively targeting the mER, the genomic proliferative actions of ER are effectively blunted, and cardiovascular protection from rapid signaling is ensured.

However, EDCs are molecules with little therapeutic potential. Variability during synthesis, bulky characteristics, and solubility issues, all serve as substantial setbacks for EDCs, despite their clear selectivity for mER. Recently, Katzenellenbogen and coworkers have modified the steroid core of E2 to develop novel pathway preferential estrogens (PaPEs).[76,77] The goal of these PaPEs is to selectively activate the extranuclear ER pathway by reducing the relative binding affinity of E2. The rationale is that by preventing long-term interactions between ER and its ligand, the genomic pathway can be avoided. Sustained ER-ligand complexes are necessary for the genomic actions of ER, as recruitment of coregulator protein complexes, histone modifications, and gene

transcription by RNA polymerase II are required. However, the rapid signaling pathway does not rely on sustained ER-ligand complex for activation requiring much lower ligand binding affinities. To accomplish this, PaPEs were synthesized without the central A-B-C-D core found on E2, but rather with an A-C-D core or simply an A-C core.[76] Instead of native nanomolar affinities to ER, these novel compounds have micromolar affinities. Studies in mice display their ability to retain monolayer integrity while precluding uterine and tumor growth, concurrent with EDC studies. Despite promising results, the half-life of PaPEs are similar to that of E2 (~1 hr) and the concentration necessary to obtain *in vivo* responses is 500x that of E2.

1.4 Design Considerations

1.4.1 Membrane Tethered E2

Clearly, there is a demonstrated need to develop an ER agonist that is selective for mER with therapeutic potential for cardiovascular protection. Selective mER was accomplished previously through the use of EDC or PaPEs, but sacrifice key therapeutic design elements such as solubility and stability.

We propose the synthesis of three conjugates for the selective activation of mER: a membrane tethered lipidated E2 derivative (MT-E2), a transthyretin binding E2 (TB-E2) conjugate, and an E2-GLP-1 conjugate (Figs. 10-12). Lipidated compounds have been

previously widely used to ensure membrane tethering to the plasma membrane as well as binding to the blood serum albumin. Lipidation to proteins within the cell has been shown to localize proteins to the 1 nm diameter surface layer at the membrane. Given the volume of the cell as 1000x the volume at that thin layer, the effective concentration at the membrane of these cytosolic proteins increases 1000-fold as well.[78] Translational degrees of freedom are also reduced from three to two, further increasing effective molarity at the membrane.[79] The extracellular space is much greater than the volume of the cell, allowing us to achieve at least 1000-fold increases in effective concentration for our E2 lipid conjugate, MT-E2. Further, lipidation of small molecules and proteins extend half-life by binding to human serum albumin (further explained in Part I). For MT-E2 reversible binding will permit binding to the plasma membrane or to mER. The phenolic spacer ensures retention of the native orientation of E2 in the ligand binding pocket. PEGylation is also employed to improve solvation of the conjugate, reduce renal clearance, and preclude entry into the cell due to an extended hydrogen bonding network with water.[80]

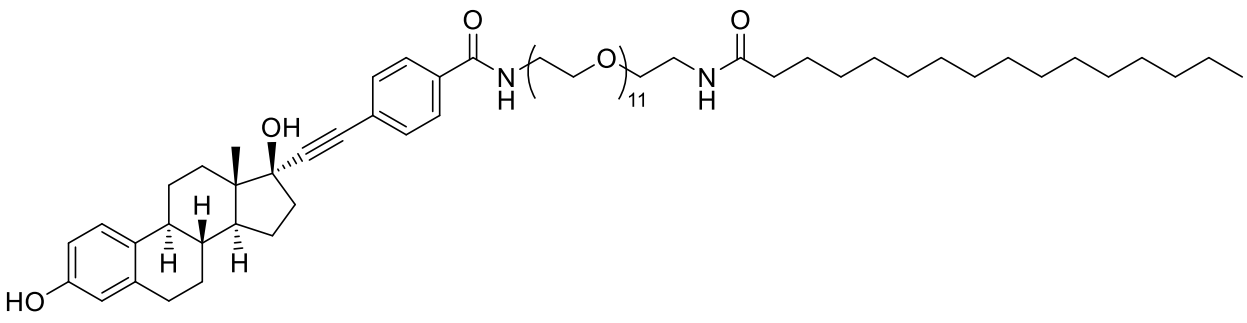

Figure 12. Structure of the membrane tethered estradiol conjugate.

1.4.2 Transthyretin Binding Conjugate

Transthyretin is a 55 kDa homo-tetramer similar to human serum albumin and is responsible for the transport of retinol binding protein (RBP) bound to either retinol of Vitamin A.[81] Transthyretin exists at lower concentrations than serum albumin (5 μM), yet the reversible binding of RBP increases the half-life of *holo*-RBP from 3.5h to 11h, garnering interest from scientists.[81–83] Penchala et al., designed a potent and selective transthyretin binding small molecule (Kd ~32 nM) TLHE1 capable of being attached to gonadotropin-releasing hormone agonists and other peptides through facile click coupling.[84] The half-life of all TLHE1-peptide conjugates explored significantly increased while retaining preferential binding to their target receptors. The application of TLHE1 to E2 was of interest due to the stability and preferential binding properties. Since AG10 binds to transthyretin at nM affinities, we hypothesized that conjugating TLHE1 to E2 (TB-E2) would establish an equilibrium between the two binding partners: transthyretin and mER. Consequently, concentrations of free TB-E2 and potential for TB-E2 to traverse the plasma membrane would be effectively reduced. The desired conjugate retains both the aromatic spacer and PEG components utilized for MT-E2, but also contains the TLHE1 transthyretin binding small molecule. Importantly, TB-E2 as a small molecule provides desirable soluble properties imparted by its aromatic functional groups and may enhance therapeutic potential of E2.

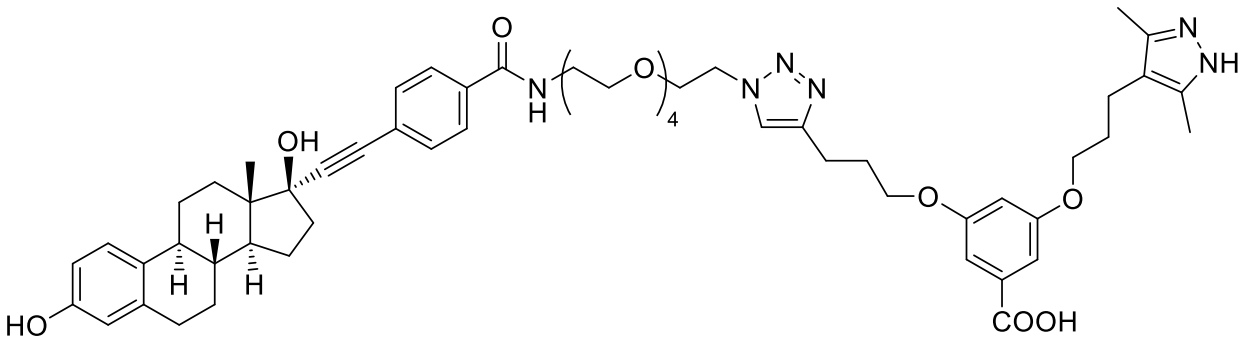

Figure 13. Structure of the transthyretin binding conjugate.

1.4.3 E2-GLP-1 Conjugate

Glucagon-like peptide-1 (GLP-1) is a 30 or 31 amino acid peptide hormone produced from intestinal L-cells to regulate glucose homeostasis and satiety through the actions at the G-protein coupled receptor (GPCR) GLP-1R (further outlined in Part I). Applications have mostly been for the treatment of type II diabetes (T2D), but it is important to note that T2D and CVD are irrevocably intertwined diseases. In fact, most T2D patients ultimately succumb to cardiovascular diseases. At least 68% of T2D patients over the age of 65 die from heart disease.[85] Interestingly, GLP-1 proves to have cardiovascular protective effects, contributing to vasodilation through both nitric oxide dependent and independent pathways. Owing to its short half-life (~90 seconds), the peptide hormone has been repeatedly modified to enhance stability for the treatment of type II diabetes. The premier GLP-1 mimetic liraglutide designed by NovoNordisk, employs lipidation at Lys26 to increase half-life.[86] Though treatment of GLP-1 receptor agonists have been used for,

treatment with liraglutide, significantly decreased risk of cardiovascular events in T2D patients.[87] Interestingly, ERα is widely expressed in the medial amygdala of the brain. Signaling at ERα in the amygdala has been seen to have a prominent effect, decreasing food intake and increasing energy expenditure possibly through the rapidly signaling pathway.[88] E2 administered by transdermal patch also plays a role in increasing insulin sensitivity and lowering blood glucose levels in post-menopausal women.[89] Insulin insensitivity serves a critical role in rendering T2D patients hyperglycemic, suggesting that E2 can be a viable molecule to treat T2D, in addition to cardiovascular disease.

GLP-1 is particularly interesting for both the carrier and selectivity properties that it can impart to E2. The addition of GLP-1 to E2 will substantially increase the size of the conjugate, precluding entry into the cell and selectively activate mER. A possible setback arises due to GLP-1 binding to GLP-1R. Sustained GPCR signaling is normally followed by clathrin light chain mediated endocytosis for eventual lysosomal degradation and recycling.[90] This endocytic process introduces both GPCR and its respective ligand into the cellular environment, which poses a problem for E2-conjugated GPCR agonists. E2 endocytosis into breast or uterine tissue cells may result in activation at the nuclear ER and result in proliferative genomic consequences. Yet, GLP-1R expression is localized to tissues such as the pancreas, liver, heart, kidney, and lung rather than oncogenic susceptible tissues such as the breast or uterus. Thus, endocytosis at these tissues is

permitted and perhaps welcomed as perhaps nuclear E2 signaling at target tissues such as the arterial wall can be accomplished. Indeed, Finan et al. explored a E2-GLP-1 conjugate that conferred both anti-diabetic and cardioprotective effects, though significant changes were observed only at a high concentration of 400 μg/kg.[91] In addition, the activity of E2 at its respective receptor was less than 1% of native E2, possibly owing to the structure of the conjugate. E2 was linked through an ether bond at the 3rd position (phenol) to the C-terminus of a modified GLP-1. As mentioned previously, both hydroxyls at the 3rd and 17th position are crucial for the orientation and binding of E2 in the ligand binding pocket of estrogen receptor. Thus, both affinity and potency are negatively and significantly impacted by the ether linkage. Nevertheless, decreased blood glucose levels, fat mass, triglycerides, cholesterol, and fatty acids were observed. Further, increased weight loss and reduced food intake indicated that the E2-conjugate was capable of acting on the central nervous system. Interestingly, at a 4,000 μg/kg dosage, there were no increases in uterine or MCF-7 xenograft tumor size. Still, the ether bond at the 3rd position poses a significant obstacle for E2 signaling.

The desired E2-GLP-1 conjugate is composed of E2, GLP-1, an *N*-trifluoroethyl histidine, and a combined oligo-ethylene glycol (OEG)/γ-glutamyl linker. Instead of a 3rd position ether bond, E2 will be conjugated at the 17th position through an aromatic spacer to the combined OEG/ γ-glutamyl linker. Recently our lab has proved that *N*-terminal

modifications, namely with a trifluoroethyl alkylation, can preserve potency and integrity of GLP-1 can be accomplished. The OEG γ-glutamyl linker provides improved solubility properties in addition to assuring unperturbed binding for E2 and GLP-1.

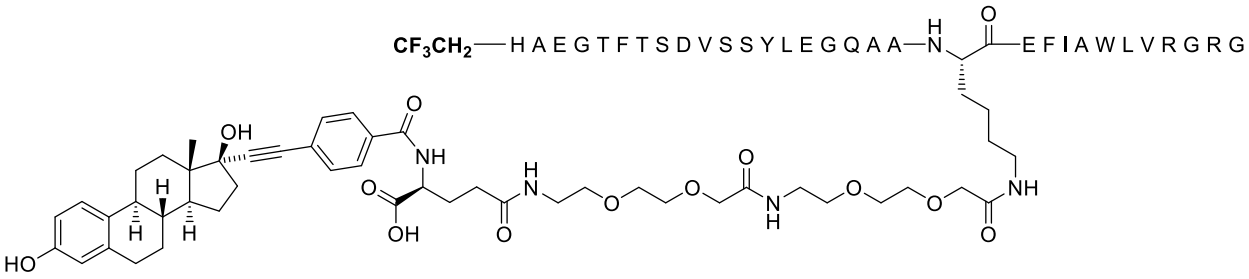

Figure 14. Structure of the E2-GLP-1 conjugate.

Chapter 2: Experimental Section

All organic reactions were performed under argon atmosphere. All organic reactions were carried out with Dr. John Issa. All solid phase peptide chemistry was carried out in a 10-mL reaction vessel under nitrogen atmosphere. Residues 3-42 (on Wang resin) were obtained from the Tufts University School of Medicine Core Facility. Reagent equivalents for all peptide couplings were as follows: amino acid building block (0.4 mmol, 13.3 eq) HBTU/HATU (0.36 mmol, 12 eq) *N,N*-diisopropylethylamine (110 µL, 0.63 mmol, 21 eq). Fmoc was deprotected with 20% piperidine (1x5 min, 1x15 min). Solvents for reactions were dried on an Innovative Technologies PureSolv 400 solvent purifier. NMR solvents were purchased from Cambridge Isotope Labs. All chemicals were purchased at the highest possible purity from ChemImpex and Sigma-Aldrich and used as received. Flash column chromatography was performed on SiliCycle P-60 silica gel, 230-400 Mesh. Analytical and preparative thin layer chromatography (TLC) was carried out on EMD silica gel 60 F-254 plates. Products were visualized using UV or by staining with 5% aqueous sulfuric acid or ceric ammonium molybdate. NMR spectra were recorded on a Bruker Avance III NMR spectrometer at 500 MHz for ^{1}H NMR, 125 MHz for ^{13}C NMR, and 500 MHz for Gradient HSQC. Chemical shifts are reported in ppm relative to tetramethylsilane (for ^{1}H NMR in $CDCl_3$) or $CDCl_3$ (for ^{13}C NMR in $CDCl_3$). For ^{1}H NMR spectra, data are reported as follows: δ shift, multiplicity [s = singlet, bs = broad singlet, d = doublet, dd = doublet of doublets, ddd = doublet of doublet of doublets m = multiplet, t = triplet, td = triplet of doublets], coupling constants are reported in Hz. Low resolution mass spectra (LRMS) were obtained using a Finnigan LTQ ESI-MS with an additional APCI source.

Synthesis and purification of **1**

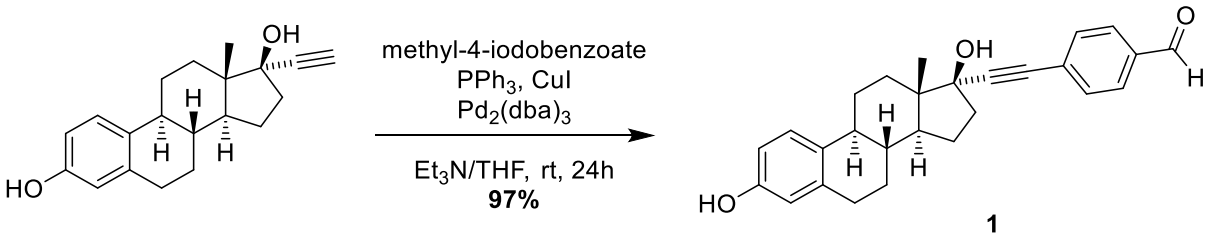

1

Tris(dibenzylideneacetone) dipalladium (Pd_2dba_3) (45.79 mg, .05 mmol), triphenylphosphine (26.28 mg, .1 mmol), copper iodide (2 mg), methyl-4-iodobenzoate (470.54 mg, 2.028 mmol), and 17α-ethynylestradiol (300.56 mg, 1.014 mmol) were dissolved in 10 mL of DMF and 10 mL of triethylamine. Manipulation of the stir bar was needed to ensure dissolution of the catalyst. The mixture was stirred for 24h at r.t., and the crude product mixture was a dark yellow-green. The product was washed with ammonium hydroxide (3x50 mL) to extract any remaining copper catalyst. Extraction of copper was indicated by a light blue aqueous layer. The organic layer was extracted, filtered through Celite®, dried over anhydrous sodium sulfate and concentrated under vacuum. The crude product was loaded with dichloromethane and purified using silica gel flash column chromatography (60-50% ethyl acetate in hexanes). ^{1}H NMR was used to confirm the product. The reaction afforded a yield of 97% and was an off white solid.

^{1}H NMR ($CDCl_3$, 500 MHz) δ: 10.01 (s, 1H), 7.83 (d, 2H, J = 10.5 Hz), 7.55 (d, 2H, J = 10.5 Hz), 7.07 (d, 1H, J= 8.0 Hz), 6.53 (dd, 1H, J = 2.4 Hz, J = 8.0 Hz), 6.50 (d, 1H, J = 2.47 Hz), 3.45-1.20 (m, 15H), 0.88 (s, 3H).

Synthesis and purification of **2**

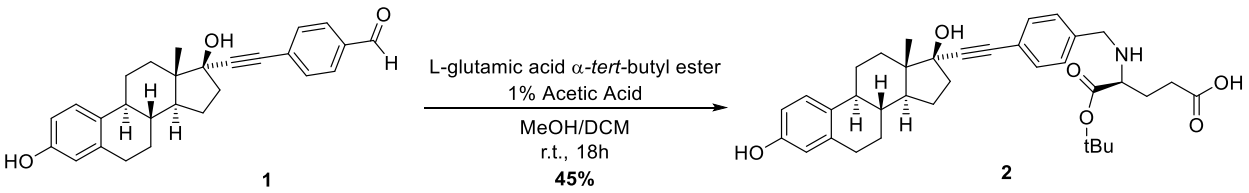

L-glutamic acid α-tert-butyl-ester (66.97 mg, 0.3296 mmol, 1.1 eq), **1** (120 mg, 0.2996 mmol, 1.0 eq), $NaBH_3CN$ (20.71 mg, 0.3296 mmol, 1.1 eq) were dissolved in a 1.5 mL methanol/dichloromethane mixture (1:2) and 15 µL of glacial acetic acid was added. The mixture was stirred at room temperature for 18h. The crude product was directly purified by silica gel flash column chromatography (10% methanol in DCM). The reaction afforded a yield of 45% and was an off-white solid. ^{1}H NMR was used to confirm the product.

^{1}H NMR (MeOD, 500 Mhz) δ: 7.46 (dd, 4H, J = 8.0 Hz, J = 12.0 Hz), 7.11 (d, 1H, J = 8.5 Hz), 6.56 (dd, 1H, J = 2.0 Hz, J = 8.5 Hz), 6.50 (d, 1H, J = 1.5 Hz), 4.12-3.94 (s, 2H), 3.74-3.59 (m, 1H), 3.40-3.25 (m, 4H), 2.88-2.72 (m, 2H), 2.58-1.76 (m, 14H), 1.57-1.23 (m, 18H), 0.94 (s, 3H)

2.2.3 First E2-GLP-1 Synthesis Attempt

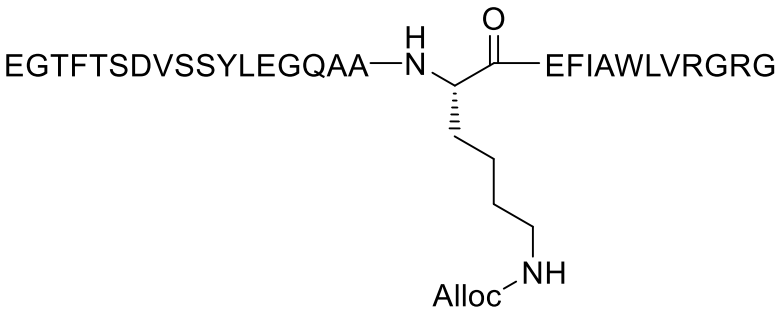

E2-GLP-1 was synthesized on a 0.03 mmol scale and the remaining peptide was prepared as per standard Fmoc solid phase peptide synthesis. Each coupling was confirmed by Kaiser (ninhydrin) test. The K26 residue was Alloc protected, and selectively deprotected. Phenylsilane (100 mg) and 5 mL DCM was added to the reaction vessel, and the resin was degassed for 5 min. $Pd(PPh_3)_4$ (30 mg) was added directly and the reaction vessel was shaken for 6h. Resin was washed and excess palladium was removed with the scavenger sodium diethyl dithiocarbamate trihydrate (50 mg) dissolved in DMF (5x2 mL). E2-GLP-1 was cleaved from the resin using a trifluoroacetic acid cleavage mixture (95 TFA:2.5 triisopropylsilane:2.5 H_2O), precipitated with diethyl ether, and dried *in vacuo*. However, the product was unable to be confirmed by ESI-MS.

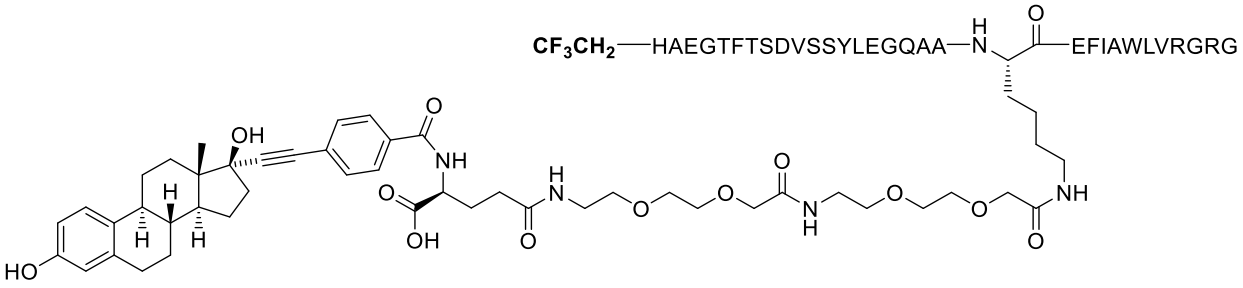

2.2.4 Synthesis and purification of **3**

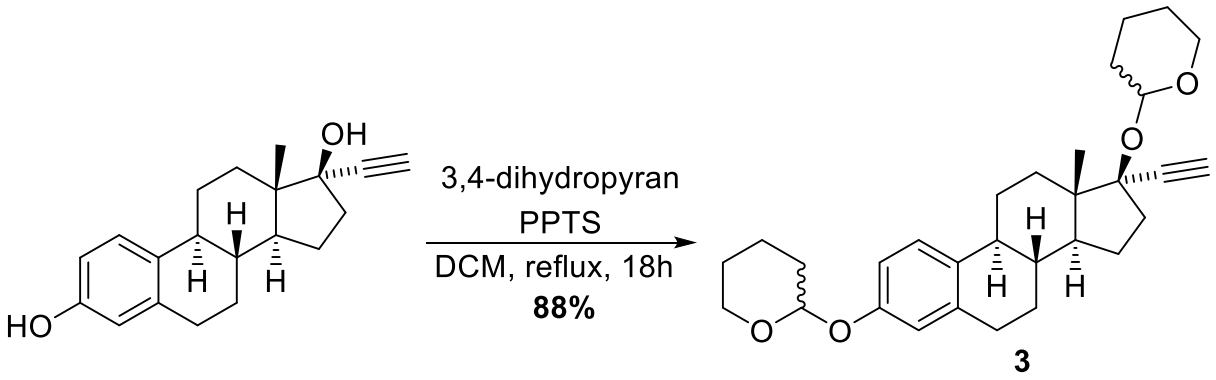

3

17α-ethynylestradiol (300.56 mg, 1.014 mmol, 1.0 eq), and pyridinium p-toluenesulfonate (25.48 mg, 0.1014 mmol, 0.10 eq) were dissolved in 8 mL dichloromethane and reflux was commenced (40°C). 3,4-dihydropyran (858 mg, 10.14 mmol, 10.0 eq), was added dropwise to the reaction mixture and stirred for 18h. The reaction mixture was diluted with dichloromethane and washed with brine (2x50 mL) and saturated aqueous sodium bicarbonate (1x50 mL). The organic layer was extracted, dried over anhydrous sodium sulfate, filtered, and concentrated *in vacuo*. The crude product was dissolved in dichloromethane, and purified by silica gel flash column chromatography (15% ethyl acetate in hexanes). The reaction afforded a yield of 88%, was characterized by ^{1}H NMR, and was a white solid.

^{1}H NMR ($CDCl_3$, 500 Mhz) δ: 7.21 (d, 1H, J = 8.5 Hz), 6.83 (d, 1H, 8.51 Hz), 5.42-5.36 (m, 1H), 5.25-5.18 (m, 1H), 4.05-3.84 (m, 2H), 3.64-3.56 (m, 1H), 3.56-3.46 (m, 1H), 2.91-2.77 (m, 2H), 2.60 (s, 1H), 2.38-1.28 (m, 23H), 0.94 (s, 3H)

Synthesis and purification of **4**

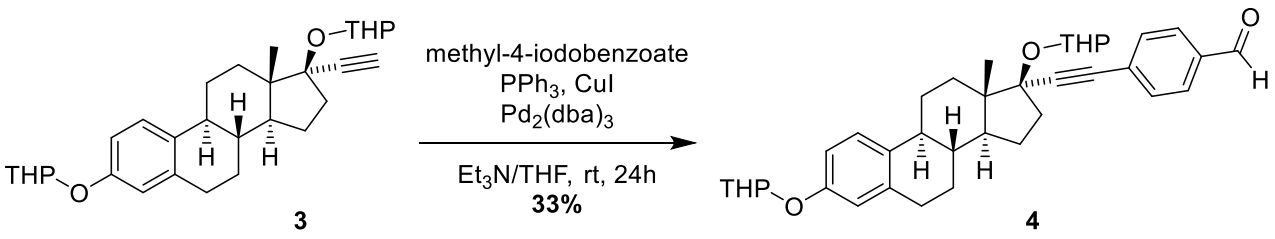

3 (352.5 mg, 0.8 mmol, 1.0 eq), methyl-4-iodobenzoate (371.23 mg, 1.6 mmol, 2.0 eq), copper (I) iodide (7.618 mg, 0.4 mmol, 0.5 eq), triphenylphosphine (83.93 mg, 0.32 mmol, 0.4 eq), and Pd_2dba_3 (36.63 mg, 0.04 mmol, 0.05 eq) were dissolved in 10 mL anhydrous THF and 10 mL triethylamine. The flask was protected from light and stirred at room temperature for 24h. The reaction mixture was concentrated down and washed with ammonium hydroxide (2x50 mL). The organic layer was extracted, filtered through Celite®, dried over anhydrous sodium sulfate, filtered, and dried *in vacuo*. The crude product was redissolved in ethyl acetate and purified by silica gel flash column chromatography (15-20% ethyl acetate in hexanes). The reaction afforded a 33% yield and was a white solid. Purified product was identified by ^{1}H NMR.

^{1}H NMR ($CDCl_3$, 500 Mhz) δ: 10.00 (s, 1H), 7.83 (d, 2H, J = 8.0 Hz), 7.59 (dd, 2H, J = 3.5 Hz, J = 8.0 Hz), 7.21 (d, 1H, J = 8.5 Hz), 6.85 (d, 1H J = 8.5 Hz), 6.79 (s, 1H), 5.39 (s, 1H), 4.00-3.89 (m, 1H), 3.65-3.50 (m, 2H), 2.92-2.78 (m, 2H), 2.40-2.30 (m, 2H), 2.29-2.20 (m, 1H), 2.04-1.33 (m, 23H), 0.98 (s, 3H)

Synthesis and purification of **5**

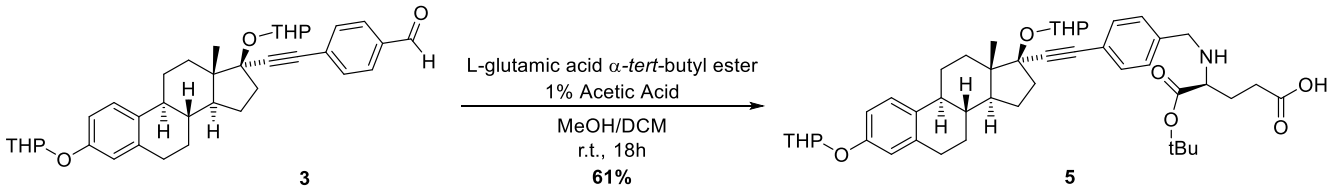

L-glutamic acid α-tert-butyl-ester (45.6 mg, 0.255 mmol, 1.1 eq), **3** (116 mg, 0.2054 mmol, 1.0 eq), sodium cyanoborohydride (12.8 mg, 0.204 mmol, 1 eq) were dissolved in a 1.5mL methanol/dichloromethane mixture (1:2) and 15 µL of glacial acetic acid was added. The mixture was stirred at room temperature for 18h. The crude product was directly purified by silica gel flash column chromatography (5% methanol in dichloromethane). The reaction afforded a yield of 61% and was an off-white solid. ^{1}H NMR and ESI-MS was used to confirm the product.

^{1}H NMR (MeOD, 500 Mhz) δ: 7.47-7.40 (m, 2H) 7.32-7.28 (m, 2H), 7.23 (d, 1H, J = 9.5 Hz), 7.19 (d, 1H, J = 8.0 Hz), 6.87 ppm (d, 1H, J = 7.0 Hz), 6.81 (d, 1H, J = 2.0 Hz), 5.29 (dd, 1H, J = 1.5 Hz), 5.12-5.07 (m, 1H), 4.10-3.91 (m, 2H), 3.89-3.77 (m, 1H), 3.66-3.52 (m, 2H), 2.92-2.80 (m, 2H), 2.68-2.29 (m, 5H, 2.29-1.22 (m, 39H), 0.99 (s, 3H)

ESI^{+}: calcd $C_{46}H_{61}NO_8$ 756.45 [M+H^{+}], found 756.27 [M+H^{+}]

Second E2-GLP-1 Synthesis Attempt

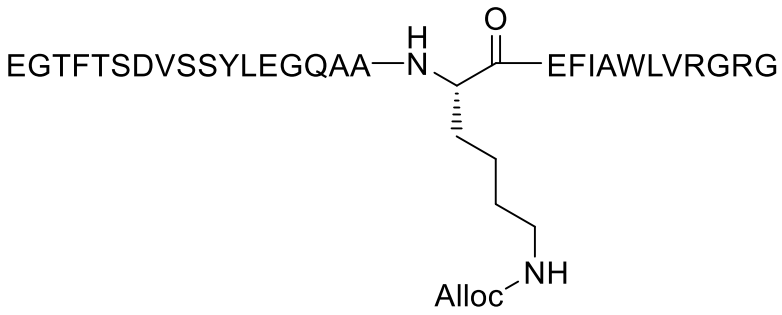

THP-E2-GLP-1 was synthesized on a 0.03 mmol scale and the remaining peptide was prepared as per standard Fmoc solid phase peptide synthesis. Each coupling was confirmed by Kaiser (ninhydrin) test. The K26 residue was Alloc protected, and selectively deprotected. Phenylsilane (100 mg) and 5 mL DCM was added to the reaction vessel, and the resin was degassed for 5 min. $Pd(PPh_3)_4$ (30 mg) was added directly and the reaction vessel was shaken for 6h. Resin was washed and excess palladium was removed with the scavenger sodium diethyl dithiocarbamate trihydrate (50 mg) dissolved in DMF (5x2mL). THP-E2-GLP-1 was cleaved from the resin using a trifluoroacetic acid cleavage cocktail (95 TFA:2.5 triisopropylsilane:2.5 H_2O), precipitated with diethyl ether, and dried *in vacuo*. However, once again, the product was unable to be confirmed by ESI-MS.

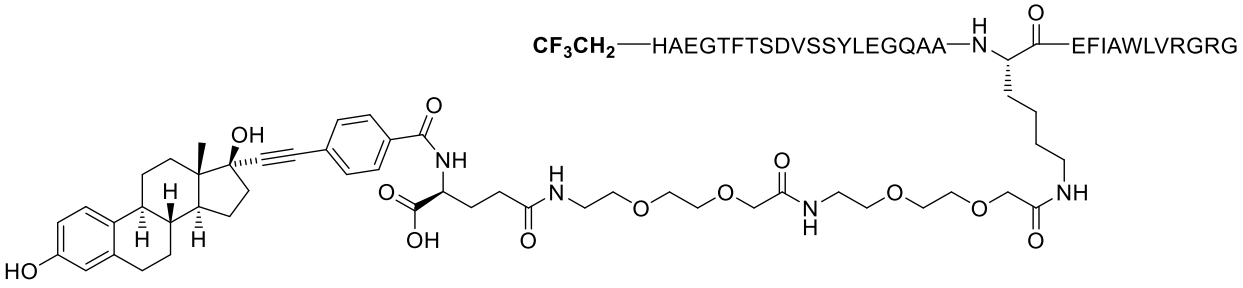

Synthesis and purification of **7**

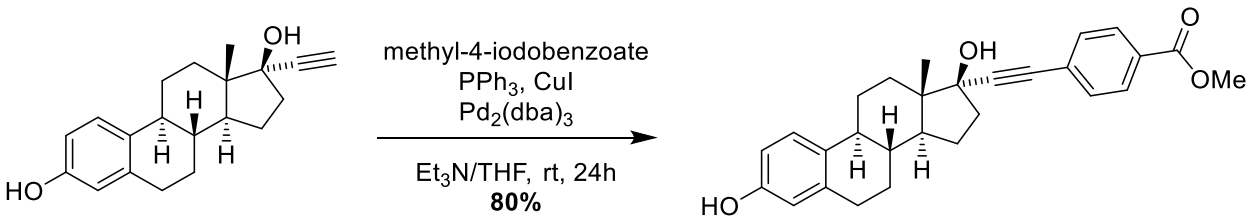

7

17α ethynyl-estradiol (500 mg, 1.685 mmol, 1.0 eq), methyl-4-iodobenzoate (663 mg, 2.53 mmol, 2.0 eq), PPh_3 (32.13 mg, 0.1687 mmol, 0.1 eq), CuI (44.25 mg, 0.1687 mmol, 0.1 eq), and $Pd_2(dba)_3$ (154 mg, 0.1687 mmol, 0.1 eq) were dissolved in 10 mL anhydrous THF and 10 mL of triethylamine was added. The reaction mixture was protected from light and stirred for 24h. The reaction mixture was concentrated and redissolved in ethyl acetate. The reaction mixture was washed with brine (1x50 mL) and ammonium hydroxide (1x50 mL). The organic layer was extracted, dried over anhydrous sodium sulfate, filtered, and dried *in vacuo*. The crude was redissolved in methanol and purified by flash silica gel column chromatography (10% methanol in dichloromethane). The reaction afforded a yield of 52% and the resulting product was confirmed by ^{1}H, ^{13}C, and HSQC NMR.

^{1}H NMR (500 MHz, CDCl3) δ: 7.99 (d, 2H, J = 8.29 Hz), 7.50 (d, 2H, J = 8.30 Hz), 7.17 (d, 1H, J = 8.45 Hz), 6.64 (dd, 1H J = 8.41, 2.54 Hz, 6.57 (d, 1H J = 2.45 Hz), 4.68 (s, 1H), 3.92 (s, 3H), 2.89-2.78 (m, 2H), 2.46-2.37 (m, 2H), 2.26-1.73 (m, 9H), 1.59 (s, 1H), 1.57-1.31 (m, 5H), 0.94 (s, 3H)

^{13}C NMR ($CDCl_3$, 125 MHz) δ: 131.58, 129.47, 126.58, 115.24, 112.70, 52.27, 49.90, 43.64, 39.46, 39.07, 33.12, 29.64, 27.20, 26.46, 22.96, 12.89

Synthesis and purification of **8**

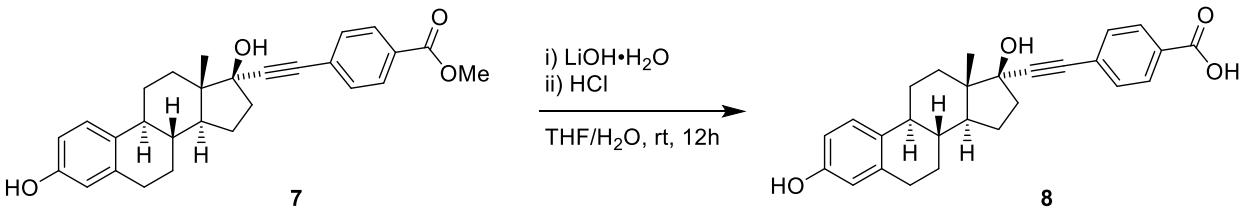

Lithium hydroxide monohydrate (374.8 mg, 1.74 mmol, 2.0 mg) was placed in a glass vial and dissolved in 2 mL H_2O. **7** (73.0 mg, 0.871 mmol, 1.0 eq) was dissolved in anhydrous THF and lithium hydroxide monohydrate was added dropwise. The product was concentrated, redissolved in methanol and purified by silica gel flash column chromatography (10% methanol in dichloromethane). The reaction afforded a quantitative yield and was confirmed by ^{1}H, ^{13}C, and HSQC NMR.

^{1}H NMR (500 MHz, MeOD) δ: 7.47 (d, 2H, J = 8.5 Hz), 7.06 (d, 1H, 9.0 Hz), 6.5 (dd, 1H, J = 2.5 Hz, J = 8.5 Hz), 6.44 (d, 1H, J = 2.5 Hz), 2.82-2.68 (m, 2H), 2.38-2.29 (m, 2H), 2.14 (dd, 1H, J= 3.0 Hz, J = 12.0 Hz), 2.05 (dd, 1H, J = 4.0 Hz, J = 13.5 Hz), 1.95 (dd, 1H, 4.0 Hz, J = 13.5 Hz), 1.89-1.73 (m, 4H), 1.50-1.21 (m, 4H), 0.89 (s, 3H).

^{13}C NMR (MeOD, 125 MHz) δ: 132.39, 130.76, 127.29, 116.04, 113.76, 51.27, 49.51, 45.20, 21.20, 39.1, 34.34, 30.74, 28.64, 27.77, 23.87, 13.49

Synthesis and purification of **9**

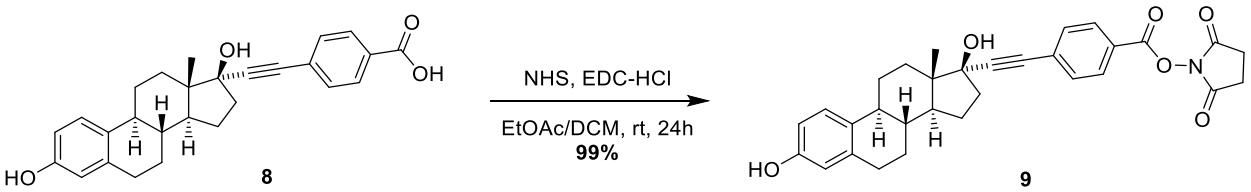

8 (412 mg, 0.989 mmol, 1.0 eq), NHS (120 mg, 1.04 mmol, 1.05 eq), EDC-HCl (199 mg, 1.04 mmol, 1.05 eq) were dissolved in DCM (20 mL) and ethyl acetate (10 mL) and stirred for 24h at room temperature. The crude reaction mixture was washed with brine (2x50 mL) and dried over anhydrous sodium sulfate. The product was dried *in vacuo* and was an amber solid. The reaction afforded a 95% yield and was confirmed by ^{1}H NMR.

^{1}H NMR (500 MHz, MeOD) δ: 8.10 (d, 2H, J = 8.5 Hz), 7.58 (d, 2H, J= 8.0 Hz), 7.20 (d, 1H, J = 8.50 Hz), 6.65 (dd, 1H, J = 3.0 Hz, J = 8.0 Hz), 6.59 (d, 1H, 2.5 Hz), 2.99-2.82 (m, 6H), 2.53-1.20 (m, 15H), 0.97 (s, 3H)

^{13}C NMR ($CDCl_3$, 125 MHz) δ: 131.95, 130.45, 126.59, 49.98, 43.63, 39.47, 33.17, 33.17, 29.64, 27.22, 26.46, 25.69, 22.99, 12.91

GLP-1 Template Synthesis and Cleavage

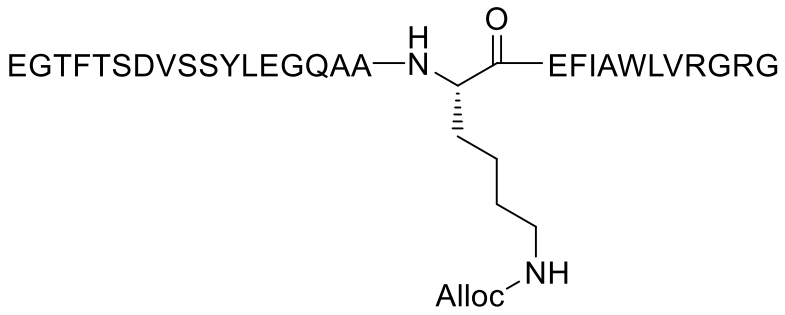

The GLP-1 template was synthesized on a 0.03 mmol scale and the remaining peptide was prepared as per standard Fmoc solid phase peptide synthesis. Each coupling was confirmed by Kaiser (ninhydrin) test. The K26 residue was Alloc protected, and selectively deprotected. Phenylsilane (100 mg) and 5 mL DCM was added to the reaction vessel, and the resin was degassed for 5 min. $Pd(PPh_3)_4$ (30 mg) was added directly and the reaction vessel was shaken for 6h. Resin was washed and excess palladium was removed with the scavenger sodium diethyl dithiocarbamate trihydrate (50 mg) dissolved in DMF (5x2mL). The GLP-1 template was cleaved from the resin using a trifluoroacetic acid cleavage mixture (95 TFA:2.5 triisopropylsilane:2.5 H_2O), precipitated with diethyl ether, and dried *in vacuo*.

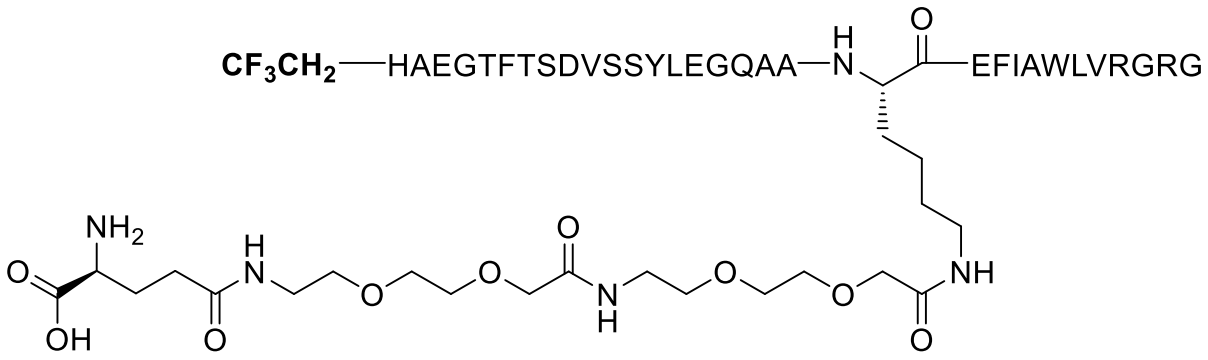

Third E2-GLP-1 Synthesis Attempt

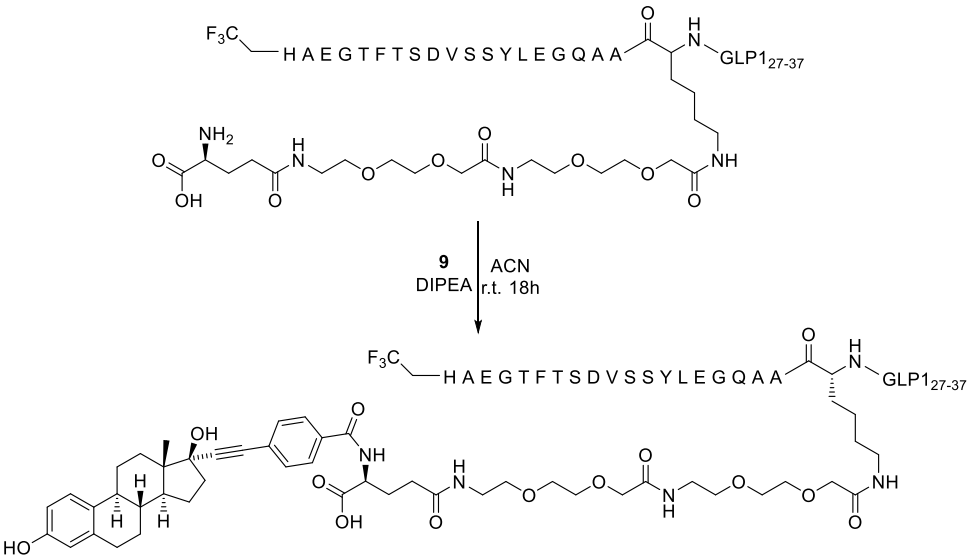

9 (35.7 mg, 0.0695 mmol, 6.0 eq), crude GLP-1 template (45 mg, 0.0116 mmol, 1.0 eq), and were dissolved in 3 mL acetonitrile. The flask was rinsed with an additional 2 mL acetonitrile. DIPEA (42 mg, 0.325 mmol, 28.0 eq) was added to the reaction mixture and the reaction was run at room temperature for 18h. The product was unable to be confirmed by ESI-MS.

Final E2-GLP-1 Synthesis and Purification

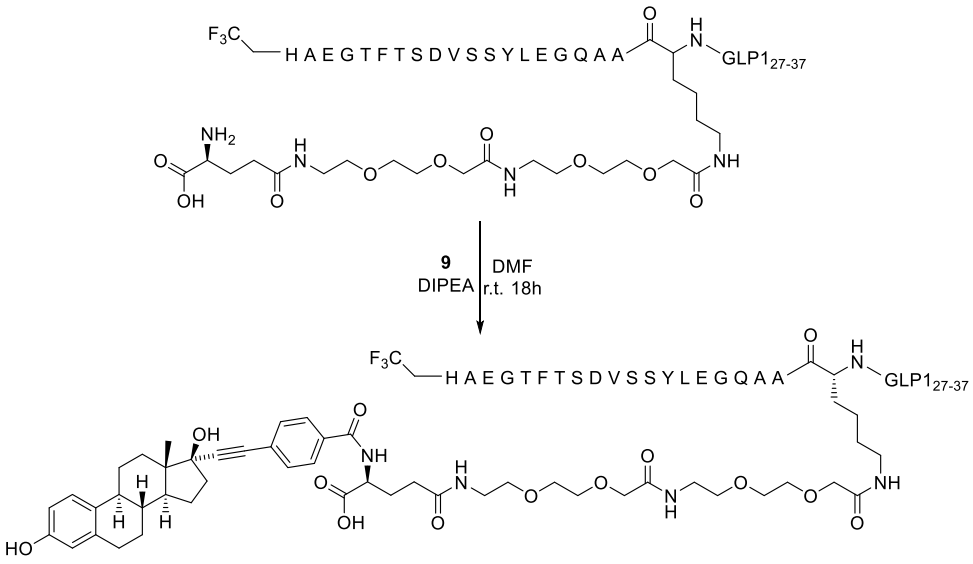

9 (50.9 mg, 0.0992 mmol, 4.0 eq), crude GLP-1 template (96.2 mg, 0.0248 mmol, 1.0 eq) were dissolved in 0.25 mL DMF in separate glass vials. *N,N*-diisopropylethylamine (48 mg, 0.372 mmol, 5 eq) was added to the GLP-1 template solution and then **9** was subsequently added. The vial was rinsed with an additional 0.25 mL DMF and the reaction was run at room temperature for 18h. The resulting E2-GLP1 conjugate was purified via semi-preparative reverse phase high performance liquid chromatography (RP-HPLC) (Vydac, C18, 10 mm, 10 mm x 250 mm). The gradient employed was 15% Solvent B_1/85% Solvent A_1 to 35% Solvent B_1/65% Solvent A_1 over 30 min at a column temperature of 55°C. The product purity was assessed by analytical RP-HPLC with a gradient of 30% Solvent B_2/70% Solvent A_2, to 60% Solvent B_2/40% Solvent A_2 over 30 min at room temperature. Product identification after reaction and purification was completed using ESI-MS.

Solvent A_1: 20% isopropanol, 80% H_2O, 0.1% trifluoroacetic acid (TFA)
Solvent B_1: 60% isopropanol, 20% acetonitrile, 20% H_2O, 0.1% TFA
Solvent A_2: 1% acetonitrile, 99% H_2O, 0.1% TFA
Solvent B_2: 90% acetonitrile, 10% H_2O, 0.07% TFA

ESI^+: found 1428.82 $[M+H^+]^{3+}$

Synthesis of N^{π}- trifluoroethyl L-Histidine methyl ester

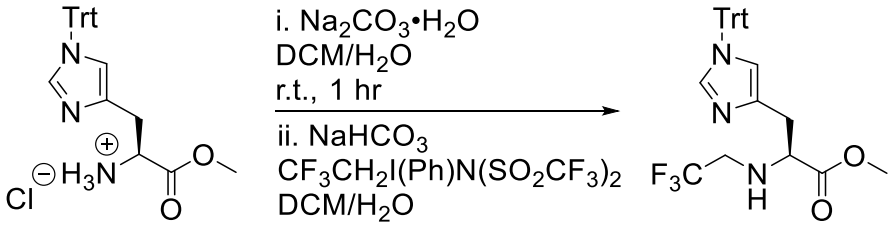

10 (1.8 g, 4.02 mmol, 1.0 eq), and sodium carbonate monohydrate (5.0 g, 40 mmol, 10.0 eq) were dissolved in 50 mL H_2O and 50 mL DCM. The reaction mixture was stirred for one hour, and the organic layer was subsequently extracted. Sodium bicarbonate (800 mg, 9.52 mmol, 3.0 eq) $CF_3CH_2I(Ph)N(SO_2CF_3)_2$ (triflimide salt) (2.00 g, 3.53 mmol, 1.1 eq), and 30 mL H_2O were added to the reaction mixture and stirred for two hours. The organic layer was extracted and concentrated. The crude product was redissolved in dichloromethane and purified by silica gel flash column chromatography (5% methanol, 5% ethyl acetate, 90% toluene). The reaction afforded a yield of 42% and the purified product was identified by ^{1}H NMR and ESI-MS.

^{1}H NMR (500 MHz, $CDCl_3$) δ: 7.38 (s, 1H), 7.33 (m, 9H), 7.15-7.09 (m, 6H), 6.59 (S, 1H), 3.69 (t, 1H, J = 6.00 Hz), 3.64 (s, 3H), 3.34-3.25 (m, 1H), 3.07-2.96 (m, 2H), 2.88 (dd, 1H, J = 7.0 Hz, J = 7.5 Hz)

Synthesis of N^{α}- trifluoroethyl L-Histidine

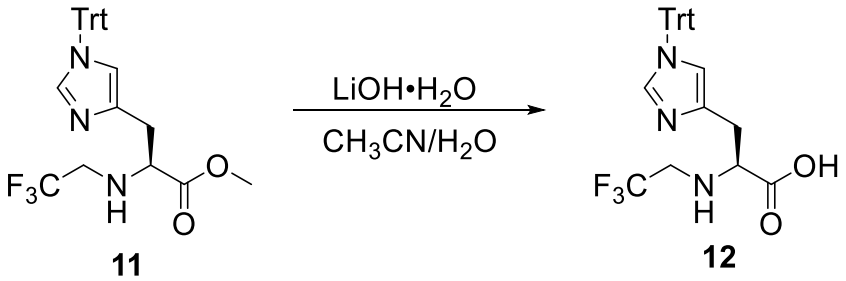

11 **12**

11 (785 mg, 1.59 mmol, 1.0 eq) and $LiOH{\cdot}H_2O$ (133.5 mg, 3.18 mmol, 2.0 eq) were dissolved in 15 mL H_2O and 15 mL acetonitrile. The reaction was stirred at room temperature for 24h and subsequently concentrated and lyophilized. The reaction afforded a quantitative yield and the product was identified by ESI-MS and ^{1}H NMR.

^{1}H NMR (500 MHz, MeOD) δ: 8.73 (d, 1H, J = 1.5 Hz), 7.50-7.45 (m, 9H), 7.24-7.19 (m, 6H), 3.63 (q, 1H, J = 5.0 Hz), 3.49-3.35 (m, 2H), 3.21-3.07 (m, 2H), 2.95 (dd, 1H, J = 6.0 Hz, J = 9.5 Hz)

Synthesis and extraction of **13**

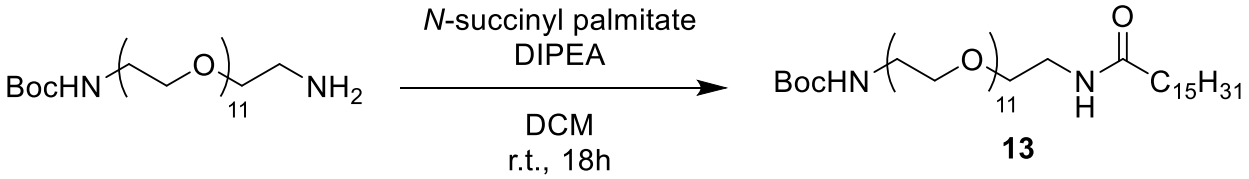

13

N-succinyl palmitate (37.1 mg, 0.105 mmol, 1.05 eq) was dissolved in 1 mL dichloromethane in a glass vial. *N,N*-diisopropylethylamine (52 µL, 0.300 mmol, 3.0 eq) was added and stirred vigorously. H_2N-PEG_{11}-NHBoc (64.5 mg, 0.100 mmol, 1.0 eq) was dissolved into 1 mL dichloromethane and added to the reaction mixture. The reaction ran for 18h and subsequently diluted with dichloromethane. The organic layer was washed with brine (1x50 mL), extracted, and dried over anhydrous sodium sulfate. It was subsequently filtered, concentrated *in vacuo*, and used for the subsequent reaction.

Synthesis and purification of **14**

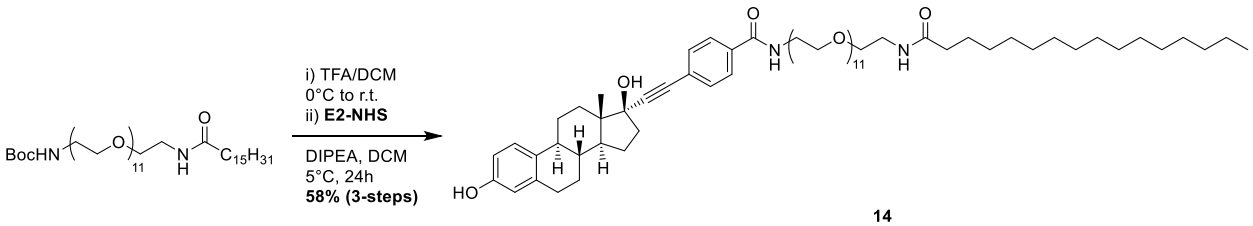

13 (88.32 mg, 0.100 mmol, 1.0 eq) was cooled to 0°C and neat trifluoroacetic acid (1.0 mL) was added dropwise. The reaction vessel warmed to room temperature and after 1.5 hr, trifluoroacetic acid was removed *in vacuo*. The resulting product was redissolved in 3.5 mL dichloromethane, triethylamine (500 µL, 3.58 mmol, 36.0 eq) was added and the reaction mixture was cooled to 5°C. **9** (53.92 mg, 0.105 mmol, 1.05 eq) was added dropwise to the reaction mixture and stirred for 24h. The reaction mixture was concentrated, redissolved in dichloromethane, and washed with brine (2x50 mL). The organic layer was extracted, dried over anhydrous sodium sulfate, filtered and concentrated. The crude product was redissolved in 7% methanol in DCM and purified by silica gel flash column chromatography (7-7.5% methanol in dichloromethane). The reaction afforded a yield of 58%. The purified product was confirmed by ESI-MS, ^{1}H, ^{13}C, and HSQC NMR.

^{1}H NMR ($CDCl_3$, 500 MHz) δ: 7.79 (d, 2H, J = 8.0 Hz), 7.48 (d, 2H, J = 8.0 Hz), 7.13 (d, 2H, 8.5 Hz), 6.86-6.76 (m, 1H), 6.65 (dd, 1H, J = 2.5 Hz, J = 8.5 Hz), 6.57 (s, 1H), 6.29 (s, 1H), 3.57-3.70 (m, 48H), 3.55 (t, 2H, J = 5.0 Hz), 3.44 (q, 2H, J = 5.0 Hz), 2.89-2.73 (m, 2H), 2.57-2.30 (m, 4H), 2.26-2.06 (m, 4H), 2.00-1.71 (m, 5H), 1.651-1.181 (m, 34H), 0.94 (s, 3H), 0.88 (t, 3H, J = 7.0 Hz)

^{13}C NMR ($CDCl_3$, 125 MHz) δ: 131.76, 127.28, 115.51, 70.31, 70.27, 70.09, 50.02, 43.85, 40.00, 39.64, 39.30, 36.83, 32.04, 29.80, 29.7, 29.66, 29.53, 29.48, 27.43, 26.61, 25.89, 22.81, 14.25, 13.06

ESI^{+}: calcd $C_{67}H_{108}N_2O_{15}$ $[M+H^{+}]$ 1180.78, found 1198.55 $[M+NH_4^{+}]$

Synthesis and purification of **15 (MT-E2 Control)**

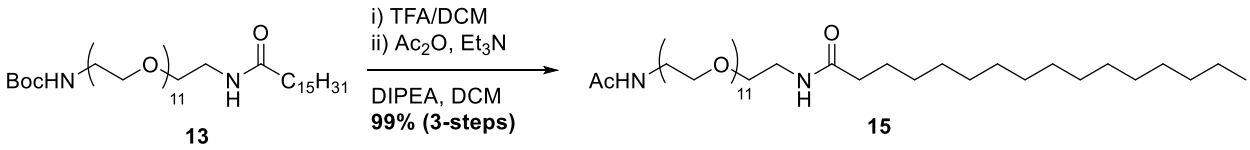

13 (88.32 mg, 0.100 mmol, 1.0 eq) was dissolved in 2.5 mL dichloromethane. The solution was cooled to 2°C and neat trifluoroacetic acid (1 mL) was added drop wise to the bath. The reaction was removed from ice and stirred for one hour. The product was dried *in vacuo* and redissolved in 3 mL dichloromethane. Triethylamine (500 µL, 3.58 mmol, 36.0 eq) was added and the mixture was cooled to 2°C. Acetic anhydride (1.0 mL, 10.0 mmol, 100 eq) was added dropwise to the mixture. The reaction mixture was stirred for 24h and washed with H_2O (1x50 mL) and ammonium chloride (1x50 mL). The organic layer was dried over anhydrous sodium sulfate, filtered, and dried *in vacuo*. The product was confirmed by ^{1}H, ^{13}C, and HSQC NMR.

^{1}H NMR ($CDCl_3$, 500 MHz) δ: 3.72-3.60 (m, 43H), 3.56 (q, 4H, J = 5.0), 3.47-3.41 (m, 4H), 3.16-3.06 (m, 3H), 2.17 (t, 2H, 8.0 Hz), 1.99 (s, 3H), 1.84 (s, 3H), 1.62 (quint, 2H, J = 8.0 Hz), 1.42 (td, 4H, J = 2.0 Hz, J = 7.5 Hz), 1.35-1.20 (m, 30H), 0.88 (t, 4H, 7.0 Hz)

^{13}C NMR ($CDCl_3$, 125 MHz) δ: 70.53, 70.24, 70.23, 70.00, 69.87, 45.78, 39.33, 39.14, 36.77, 31.94, 29.71, 29.68, 29.67, 29.54, 29.43, 29.38, 25.78, 22.71, 14.14, 8.63

ESI^{+}: calcd $C_{42}C_{84}N_2O_{13}$ [M+H^{+}] 825.61, found 842.45 [M+NH_4^{+}]

Synthesis and purification of Methyl 3-hydroxy-5-(pent-4-yn-1-yloxy)benzoate **(13)**

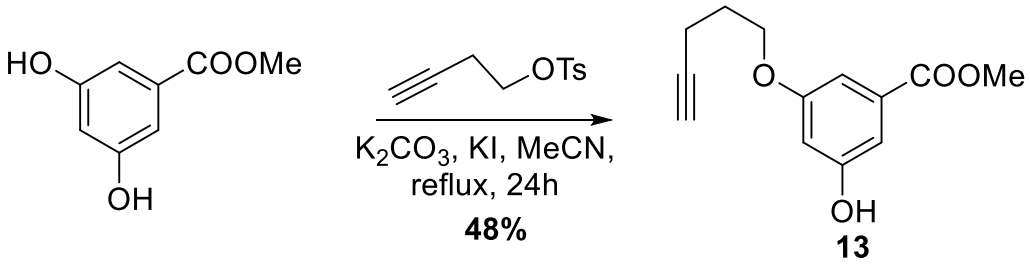

Methyl 3,5-dihydroxybenzoate (.784 g, 4.662 mmol, 1.0 eq) and 4-pentynyl *p*-tosylate (1.00 g, 4.196 mmol, 0.9 eq) were dissolved in acetonitrile (25 mL). Solid potassium iodide (.154 mg, .932 mmol, 0.2 eq) and potassium carbonate (1.288 g, 9.324 mmol, 2.0 eq), was added. The reaction flask was rinsed with 5 mL of acetonitrile and reflux was commenced. After 24h, reflux was halted, and the reaction was filtered. The crude was washed with ethyl acetate (3x50 mL). The reaction was concentrated to a yellow syrup and diluted with ethyl acetate. Silica gel flash column chromatography (15-30% ethyl acetate in hexanes)) was completed and 473 mg of the white solid product (48%) was isolated. The product was confirmed by ^{1}H, ^{13}C, and HSQC NMR.

^{1}H NMR ($CDCl_3$, 500 MHz) δ: 7.15 (m, 2H), 6.61 (s, 1H), 5.51 (s, 1H), 4.10 (t, 2H), 3.92 (s, 3H), 2.34-2.46 (m, 2H), 1.92-2.08 (m, 3H).

^{13}C NMR ($CDCl_3$, 125 MHz) δ: 109.40, 107.97, 107.23, 69.15, 66.63, 52.49, 28.18, 15.28

Synthesis and purification of Methyl 3-hydroxy-5-(pent-4-yn-1-yloxy)benzoate **(14)**

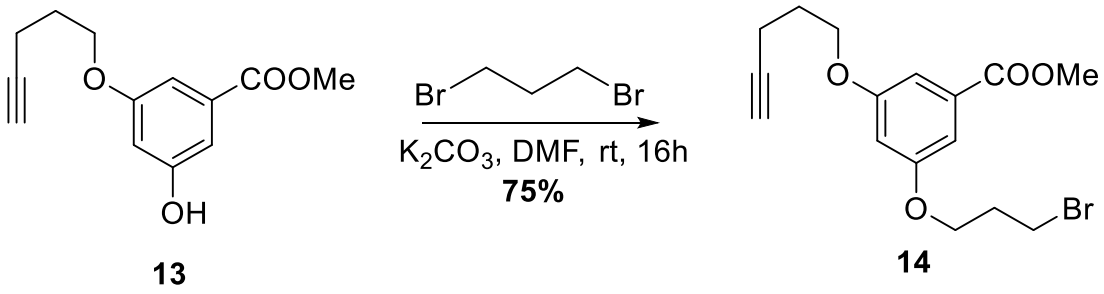

13 **14**

13 (351 mg, 1.5 mmol, 1.0 eq) and 1,3-dibromo-propane (0.76 mL, 7.5 mmol, 5.0 eq) was dissolved in 5 mL DMF. Solid potassium carbonate (249 mg, 1.8 mmol, 1.2 eq) was added and stirred for 16h at room temperature. The reaction mixture was diluted with H_2O and extracted with ethyl aceteate (2x50 mL). The organic layer was dried over Na_2SO_4, filtered, and concentrated *in vacuo*. The product was redissolved in ethyl acetate/dichloromethane and purified by silica gel flash column chromatography (100% toluene). The reaction afforded a 75% yield and the product was identified by ^{1}H, ^{13}C, and HSQC NMR. The chemical shifts and coupling constants were in accordance with previous literature characterization.[84]

Synthesis and purification of Methyl 3-(3-(3,5-dimethyl-1H-pyrazol-4-yl)propoxy)-5-(pent-4-yn-1-yloxy)benzoate **(15)**

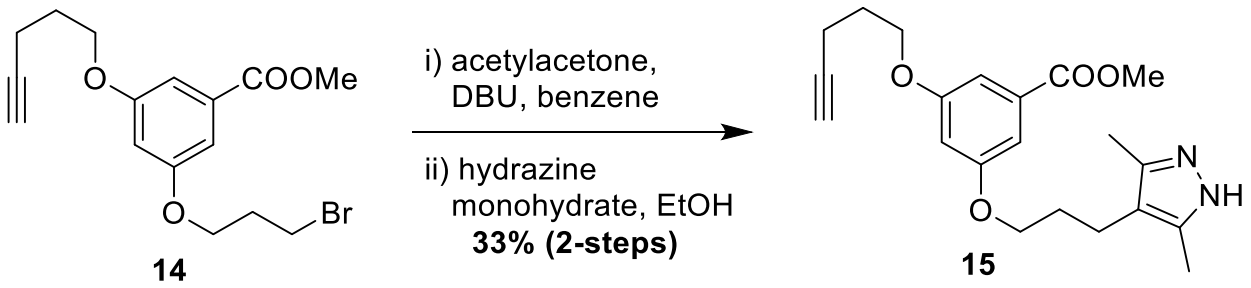

14 **15**

Acetylacetone (.223 mL, 2.18 mmol, 2.0 eq) was dissolved in 5 mL benzene. DBU (.325 mL, 2.18 mmol, 2.0 eq) was added dropwise. **14** was dissolved in 4 mL benzene and likewise added dropwise. The reaction was stirred for 24h at room temperature. The reaction mixture was diluted with dichloromethane and extracted with H_2O (2x50 mL). The organic layer was dried over anhydrous sodium sulfate, filtered, and concentrated *in vacuo*. The crude mixture was redissolved in dichloromethane and purified by silica gel flash column chromatography (2-2.5% ethyl acetate in dichloromethane). The product was dried *in vacuo* and dissolved in 5 mL ethanol. Hydrazine monohydrate was added (44 µL, 0.875 mmol, 2.5 eq) and heated to reflux for four hours. The crude mixture was concentrated *in vacuo* and purified by silica gel flash column chromatography (5% methanol in dichlormethane). The reaction afforded a 33% yield over two steps and the product was identified by ^{1}H, ^{13}C, and HSQC NMR. The chemical shifts and coupling constants were in accordance with previous literature characterization.[84]

Synthesis and purification of 3-(3-(3,5-dimethyl-1H-pyrazol-4-yl)propoxy)-5-(pent-4-yn-1-yloxy)benzoic acid **(16)**

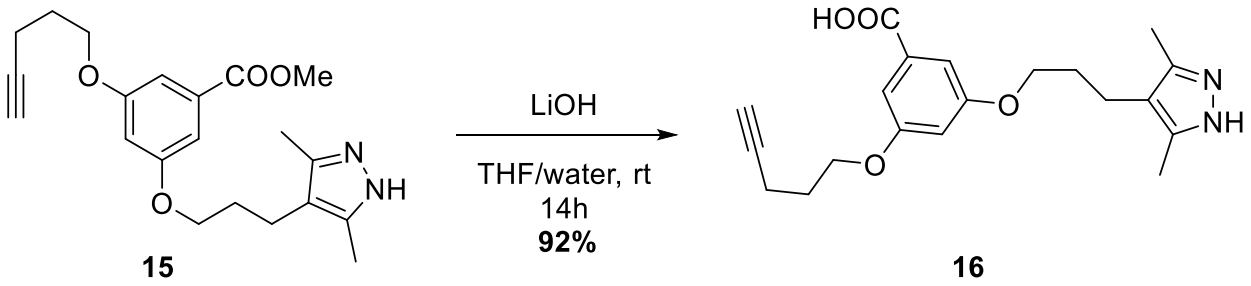

15 **16**

15 (130 mg, 0.351 mmol, 1.0 eq) was dissolved in 3 mL THF. LiOH·H_2O (29.4 mg, .702 mmol, 2.0 eq) was dissolved in 2 mL H_2O and added dropwise to the reaction mixture (further rinse transferred with 1 mL H_2O). The reaction was stirred for 14h at room temperature and neutralized with Amberlite-120 H^+ resin until pH was ~6. The reaction mixture was filtered and concentrated *in vacuo*. The crude was redissolved in 15% methanol/dichloromethane and purified by silica gel flash column chromatography (15% methanol in dichloromethane). The reaction afforded a yield of 92%. The purified product was confirmed by ^1H NMR, ^{13}C, and HSQC NMR. The chemical shifts and coupling constants were in accordance with previous literature characterization.[84]

Synthesis of **17**

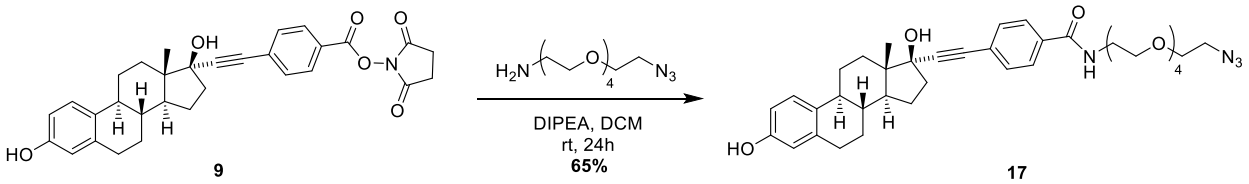

9 (53.93 mg, 0.105 mmol, 1.05 eq) was dissolved in 1 mL DCM in a flame dried double walled glass vial. *N,N*-diisopropylethylamine (52 µL, 0.300 mmol, 3.0 eq) was added to the reaction mixture and stirred for 24h at room temperature. The reaction mixture was diluted with dichloromethane, washed with H_2O (1x50 mL) and washed with brine (1x50 mL). The organic layer was extracted, dried over anhydrous sodium sulfate, filtered, and concentrated. The crude was concentrated and redissolved in 5% methanol/dichloromethane. The crude was purified by silica gel flash column chromatography (5% methanol in dichloromethane). The reaction afforded a yield of 65% and was confirmed by ESI-MS, ^{1}H, ^{13}C, and HSQC NMR.

^{1}H NMR ($CDCl_3$, 500 MHz) δ: 7.78 (d, 2H, J = 8.5 Hz), 7.48 (d, 2H, J = 8.5 Hz), 7.07 (d, 1H, J = 8.5 Hz), 6.51 (dd, 1H, 2.5 Hz), 6.45 (d, 1H, J = 2.0 Hz), 3.66-3.50 (m, 20H), 3.31-3.29 (m, 1H), 2.82-2.69 (m, 2H), 2.39-2.30 (m, 2H), 2.18-2.10 (m, 20H), 2.05 (dd, 1H, J = 3.5 Hz, J = 14.0 Hz), 1.95 (dd, 1H, J = 3.5 Hz, J = 13.0 Hz), 1.80 (m, 4H), 1.50-1.27 (m, 5H), 0.90 (s, 3H)

^{13}C NMR ($CDCl_3$, 125 MHz) δ: 132.48, 128.51, 127.30, 116.06, 113.78, 71.58, 71.52, 71.30, 71.11, 70.48, 51.73, 51.26, 48.91, 45.21, 41.18, 41.04, 39.92, 34.46, 30.74, 28.65, 27.78, 23.87, 13.51

ESI^+: calcd $C_{37}H_{48}N_4O_7$ $[M+H^+]$ 661.36, found 683.45 $[M+Na^+]$

Synthesis of **18**

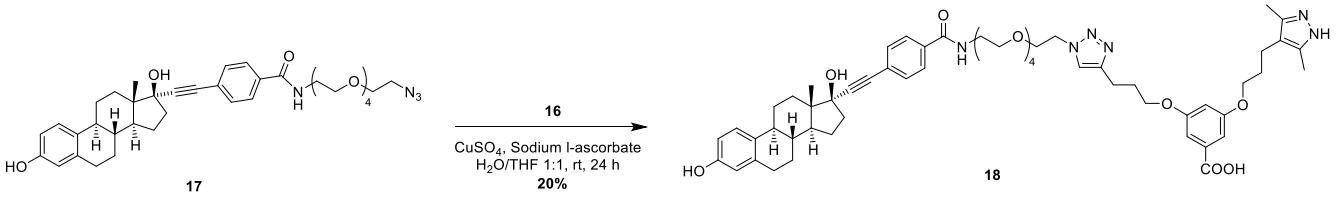

17 (18.17 mg, 0.0275 mmol, 1.1 eq) and **16** (9.26 mg, 0.250 mmol, 1.0 eq) were dissolved into 0.75 mL THF. $CuSO_4$ (4.00 mg, 0.250 mmol, 1.0 eq) and L-sodium ascorbate (9.90 mg, 0.0500 mmol, 2.0 eq) were dissolved in water. The water reagent mixture was added to the reaction mixture and stirred for 24h at room temperature. The product was isolated from a preparative thin layer chromatography (7.5% methanol in dichloromethane). The product was further purified by reverse phase HPLC with a gradient of 20% Solvent B/80% Solvent A to 60% Solvent B/40% Solvent A over 30 min at room temperature. The reaction afforded a yield of 20% and the product was confirmed by ESI-MS, ^{1}H, ^{13}C, and HSQC NMR.

Solvent A: 1% acetonitrile, 99% H_2O, 0.1% TFA
Solvent B: 90% acetonitrile, 10% H_2O, 0.07% TFA

^{1}H NMR ($CDCl_3$, 500 MHz) δ: 7.14 (d, 2H, J = 13.0 Hz), 7.10 (d, 1H, J = 8.5 Hz), 6.81 (t, 1H, J = 2.5 Hz), 6.55 (dd, 1H, J = 2.5 Hz, J = 8.5 Hz), 6.49 (d, 1H, J = 2.5 Hz), 4.52 (t, 2H, J = 5.0 Hz), 4.02 (t, 2H, J = 6.0 Hz), 3.97 (t, 2H, J = 6.0 Hz), 3.83 (t, 2H, J = 4.5 Hz), 3.67-3.50 (m, 16H), 2.89 (t, 2H, J = 7.5 Hz), 2.86-2.74 (m, 2H), 2.71 (t, 2H, J = 7.5 Hz), 2.42-2.30 (m, 8H), 2.20-1.77 (m, 11H) 1.53-1.27 (m, 5H), 0.91 (s, 3H)

^{13}C NMR ($CDCl_3$, 125 MHz) δ: 131.09, 127.12, 122.87, 114.66, 112.38, 87.84, 75.69, 75.59, 73.40, 73.25, 70.11, 70.03, 69.88, 69.09, 68.99, 68.64, 66.35, 49.92, 49.87, 48.44, 43.80, 39.78, 39.62, 38.52, 33.07, 29.44, 29.33, 28.62, 27.23, 26.37, 22.47, 21.45, 18.46, 12.10, 9.19

ESI^{+}: calcd $C_{57}H_{72}N_6O_{11}$ $[M+H^{+}]$ 1017.54, found 1017.64 $[M+H^{+}]$

Synthesis of **19**

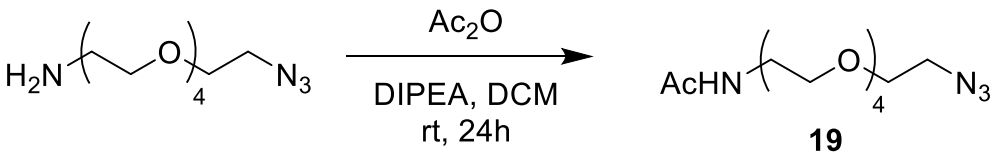

19

N_3-PEG_4-NH_2 (131.2 mg, 0.500 mL, 1.0 eq) and Et_3N (2.51 mL, 18 mmol, 36 eq) were dissolved in 5 mL dichloromethane. Acetic anhydride (4.72 mL, 50 mmol, 100 eq) was added dropwise to the reaction mixture. The reaction was stirred for 24h at room temperature. The reaction mixture was concentrated, diluted with H_2O, and extracted with DCM. The organic layer was washed additionally with brine (1x50 mL), dried over anhydrous sodium sulfate, filtered and dried *in vacuo*. The reaction afforded a quantitative yield. The purified product was confirmed by ^1H, ^{13}C, and HSQC.

^1H NMR ($CDCl_3$, 500 MHz) δ: 6.32 (s, 1H), 3.72-3.60 (m, 14H), 3.56 (t, 2H, J = 5.0 Hz), 3.44 (q, 2H, J = 5.0 Hz), 3.39 (t, 3H, 5.0 Hz), 1.99 (s, 3H)

^{13}C NMR ($CDCl_3$, 125 MHz) δ: 70.71, 70.10, 50.68, 39.33, 23.24

Synthesis of **20 (TB-E2 Control)**

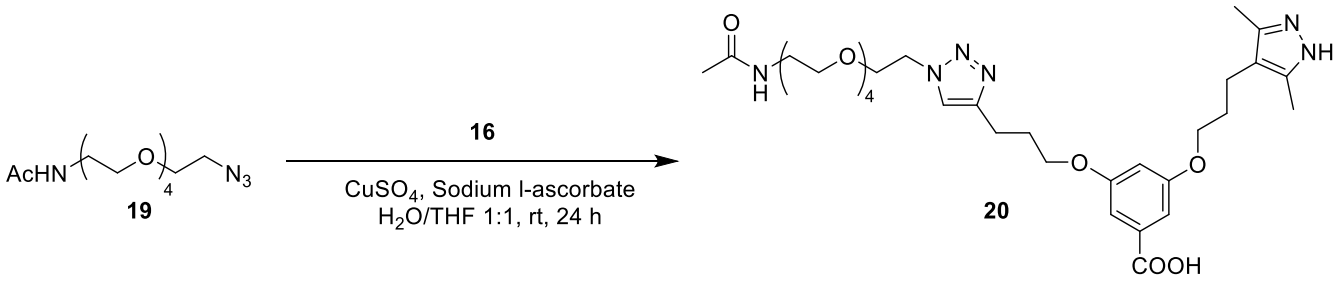

19 (16.74 mg, 0.055 mmol, 1.1 eq) and **16** (18.51 mg, 0.050 mmol, 1.0 eq) were dissolved in 0.75 mL THF. $CuSO_4$ (8.00 mg, 0.050 mmol, 1.0 eq) and sodium L-ascorbate (19.81 mg, 0.100 mmol, 2.0 eq) were dissolved in 0.75 mL H_2O. The water reagent mixture was added to the reaction mixture and stirred for 24h at room temperature. The product was isolated by preparative thin layer chromatography at 3:1:1 ethyl acetate: methanol: water. The purified product was confirmed by ESI-MS, ^{1}H, ^{13}C, and HSQC.

^{1}H NMR (MeOD, 500 MHz) δ: 7.89 (s, 1H), 7.16 (s, 1H), 7.14 (s, 1H), 6.71 (t, 1H, J = 2.0 Hz), 4.57 (t, 2H, J = 5.0 Hz), 4.07 (t, 2H, J = 6.0 Hz), 2.01 (t, 2H, J = 5.5 Hz), 3.90 (t, 2H, J = 5.5 Hz), 3.64-3.57 (m, 12H), 3.53 (t, 2H, J = 5.5 Hz), 3.36-3.34 (m, 2H), 2.93 (t, 2H, J = 7.5 Hz), 2.75 (t, 2H, J = 7.5 Hz), 2.37 (s, 6H), 2.18 (quint, 2H, J = 7.0 Hz), 2.03 (quint, 2H, J = 6.5 Hz), 1.95 (s, 3H)

^{13}C NMR ($CDCl_3$, 125 MHz) δ: 122.89, 107.20, 103.47, 70.08, 70.03, 69.83, 69.19, 69.04, 66.50, 66.16, 49.92, 39.04, 29.53, 28.71, 21.50, 21.14, 18.46

ESI^{+}: calcd $C_{26}H_{48}N_6O_9$ 661.36 $[M+H^{+}]$, found 661.45 $[M+H^{+}]$, 683.45 $[M+Na^{+}]$

Chapter 3 Results and Discussion

3.1 E2 Rearrangement Mechanisms

Initial synthetic routes to generate the E2-GLP-1 conjugate proved to be ineffective. Both compounds **2** and **5** were synthesized, characterized, and ready to be coupled to the GLP-1 template on resin. Yet, the reaction did not occur, suggesting that **2** and **5** participated in an alternative reaction. Concurrently, this mass loss was also seen when attempting to generate MT-E2 using HATU or HBTU (reaction scheme not shown). The loss of 18 suggested that a rearrangement mechanism was occurring at the 17th position hydroxyl. It was hypothesized that the hydroxyl participates in a Wagner-Meerwein rearrangement (Fig. 7). During HBTU coupling conditions, the primary reaction is not amide formation, but rather the hydroxyl directly reacts with HBTU to generate a tetramethyluronium adduct, an excellent leaving group. The adduct can shortly thereafter form tetramethylurea and a tertiary carbocation at the 17th position. Subsequently, a 1,2-alkyl rearrangement occurs. The 18th position methyl shifts to the 17th position and elimination mediated by diisopropylethylamine occurs forming an olefin. Thus, a rearranged E2 molecule is produced from the HBTU coupling. Since, the 3rd and 17th hydroxyls are necessary for orientation of E2 in the hydrophobic ligand binding pocket, eliminating the 17th hydroxyl would have significant consequences on activity at ER.[42] Forming THP protecting groups at the hydroxyls, as in **5**, may be a solution for on resin

synthesis, but TFA cleavage also activates the hydroxyl. A tertiary hydroxyl normally has a pKa ~18, and the highly acidic conditions of TFA cleavage leads to the formation of hydronium at the 17th position. Thus, the hydronium ion leaves, generating the identical tertiary carbocation and 1,2-rearrangment once again occurs. This prompted the use of an E2-NHS ester to form an activated E2 ester and perform the coupling reactions. Regarding E2-GLP-1, the template was first cleaved from the peptide and then an in-solution coupling was performed with E2-NHS. All three E2 conjugates were synthesized using the E2-NHS ester. Moreover, this Wagner-Meerwein rearrangement has been observed and characterized previously in the literature.[92,93]

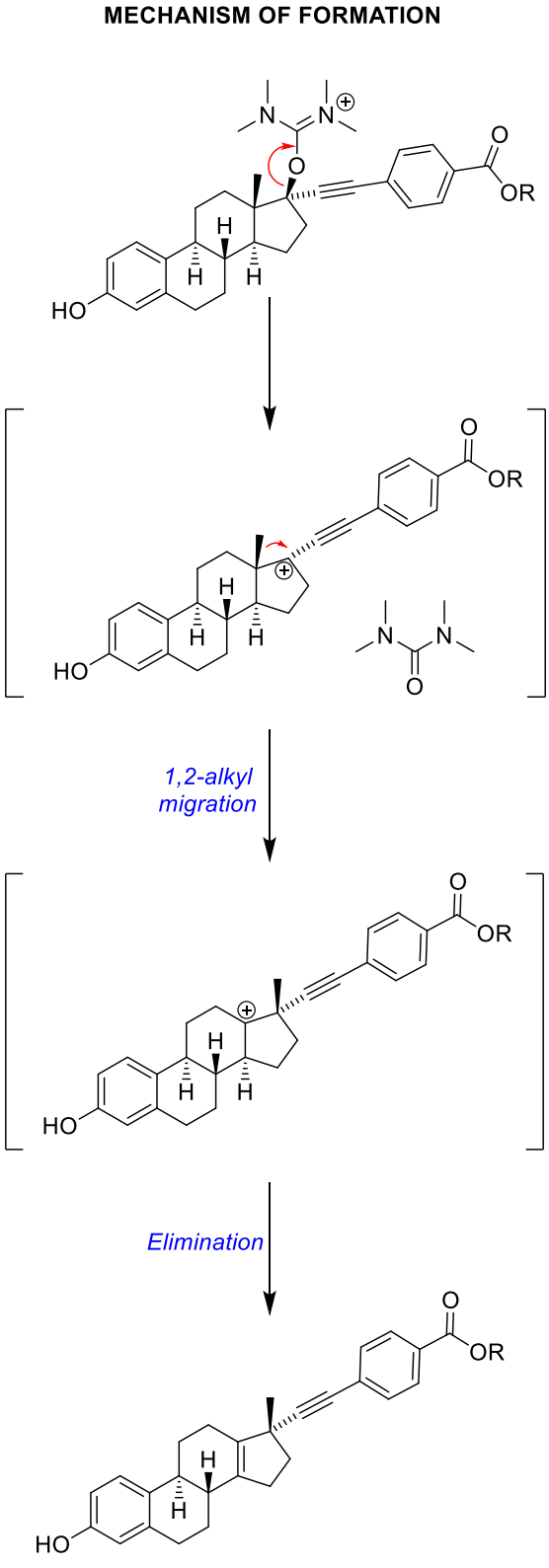

Figure 15. Mechanism of E2 rearrangement during HBTU couplings.

3.2 Preliminary *in vitro* Data

The *in vitro* cellular assays were performed by Dr. Qing Lu in Professor Gavin Schnitzler's laboratory at the Tufts Medical Center. Activation of the rapid signaling pathway was assessed for the MT-E2 and TB-E2 conjugates in Cercopithecus aethiops kidney cells (Cos-1) and human endothelial cells (EAHy-296). Cos-1 cells were transiently transfected to express ER (as in Campbell et al.[72]), while (EAHy-296) naturally express ERα. The data for both conjugates in Cos-1 cells and for TB-E2 in EAHy-296 is inconclusive. This may be due to solubility issues when preparing the conjugates for cellular assays. Interestingly, the phosphorylated:unphosphorylated ratios of eNOS, Akt, and Erk are significantly increased compared to the vehicle and control when Eahy-296 cells were treated with MTE2 (100 nM) (Figs. 9-11). Further, this activation of Akt and Erk occurs in a dose-dependent manner. Indeed, eNOS, Akt, and Erk are all downstream effector proteins that mediate rapid signaling, indicating activation at mER. Still, optimization of the assays to improve solubility of the conjugates is necessary to assess their rapid signaling properties.

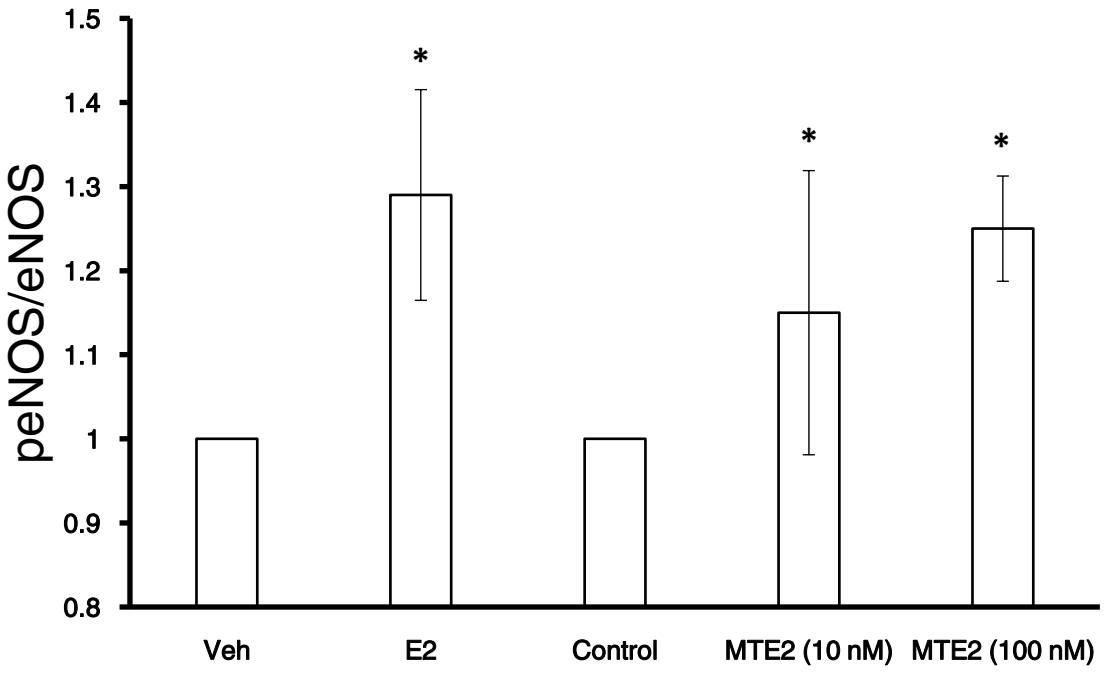

Figure 16. Human endothelial Eahy-296 cells were coincuabed with varying concentrations of MTE2 to determine eNOS phosphorylation and activation. Vehicle is P.B.S. and the control is the lipid tail without E2. *P<0.05 vs. vehicle.

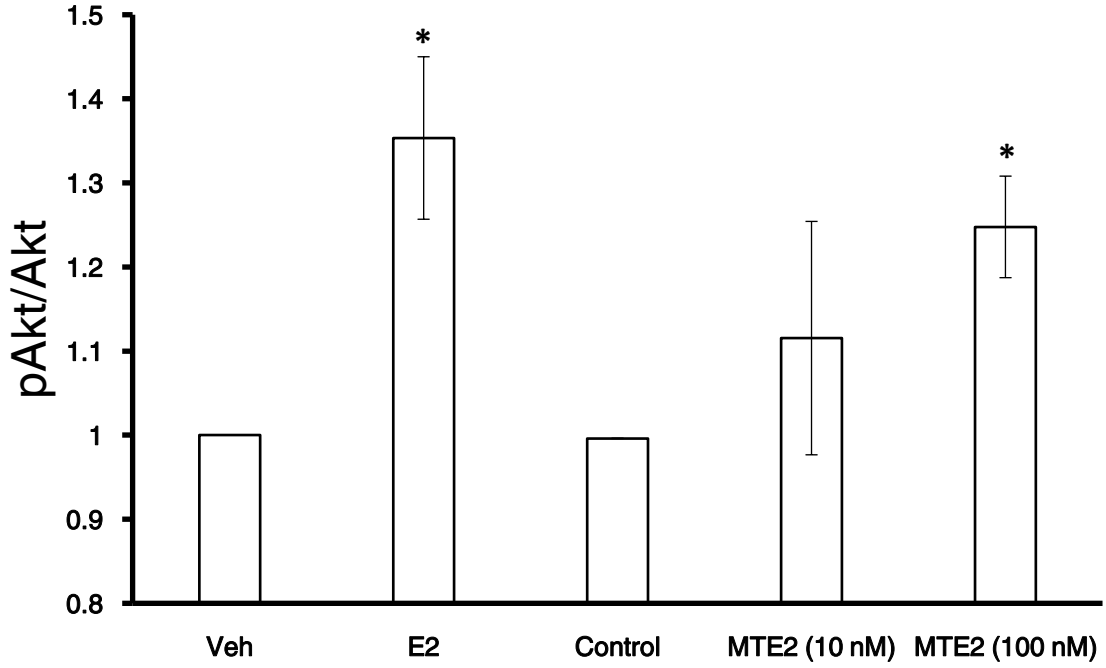

Figure 17. Human endothelial Eahy-296 cells were coincuabed with varying concentrations of MTE2 to determine pAKT phosphorylation and activation. Vehicle is P.B.S. and the control is the lipid tail without E2. *P<0.05 vs. vehicle.

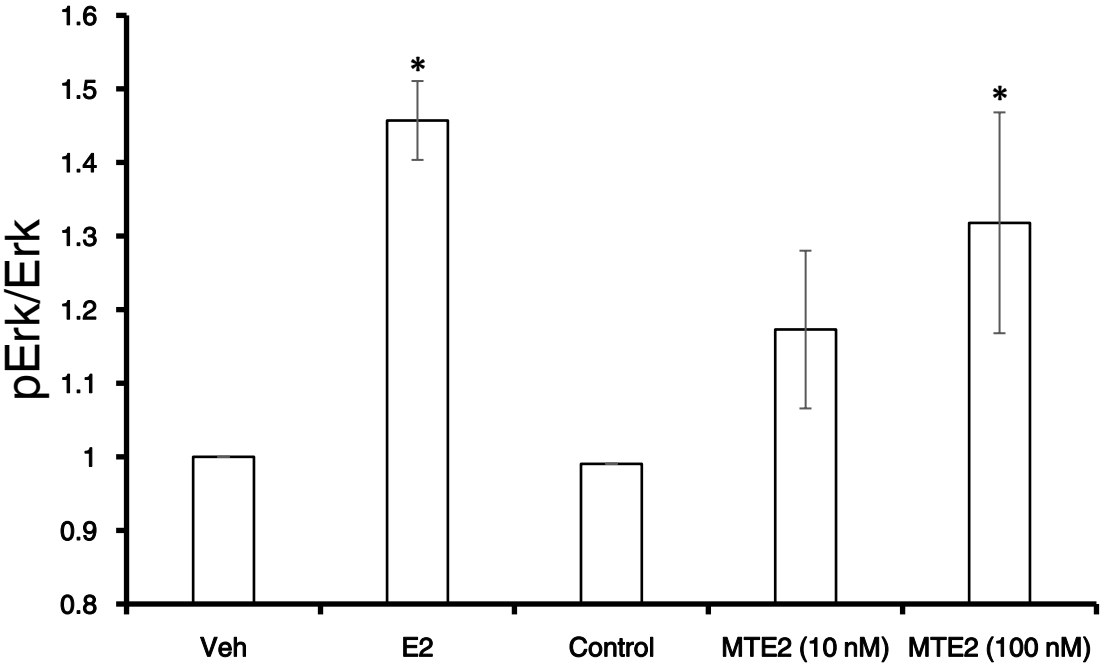

Figure 18. Human endothelial Eahy-296 cells were coincuabed with varying concentrations of MTE2 to determine pAKT phosphorylation and activation. Vehicle is P.B.S. and the control is the lipid tail without E2.

*P<0.05 vs. vehicle.

Appendix

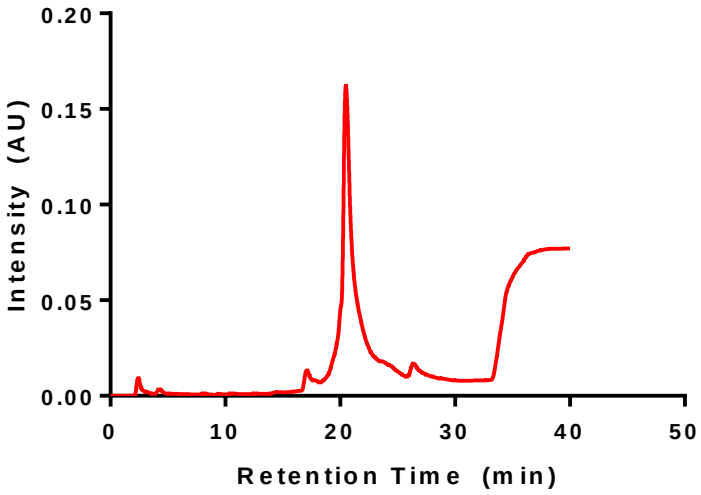

Figure 11. Analytical HPLC of E2-GLP-1 conjugate.

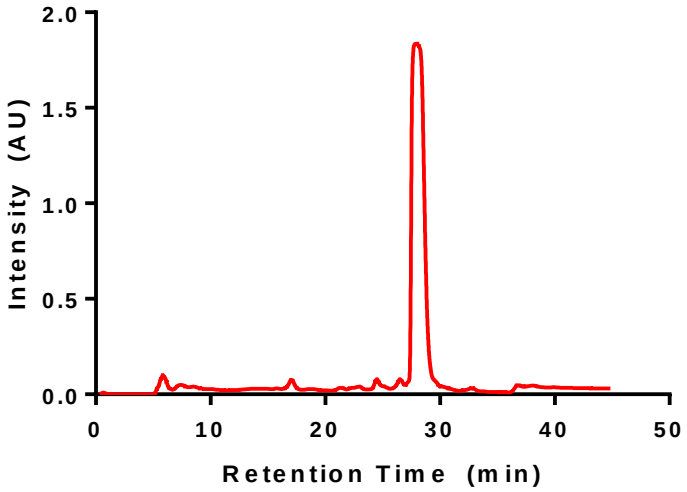

Figure 12. Analytical HPLC of E2-TB conjugate.

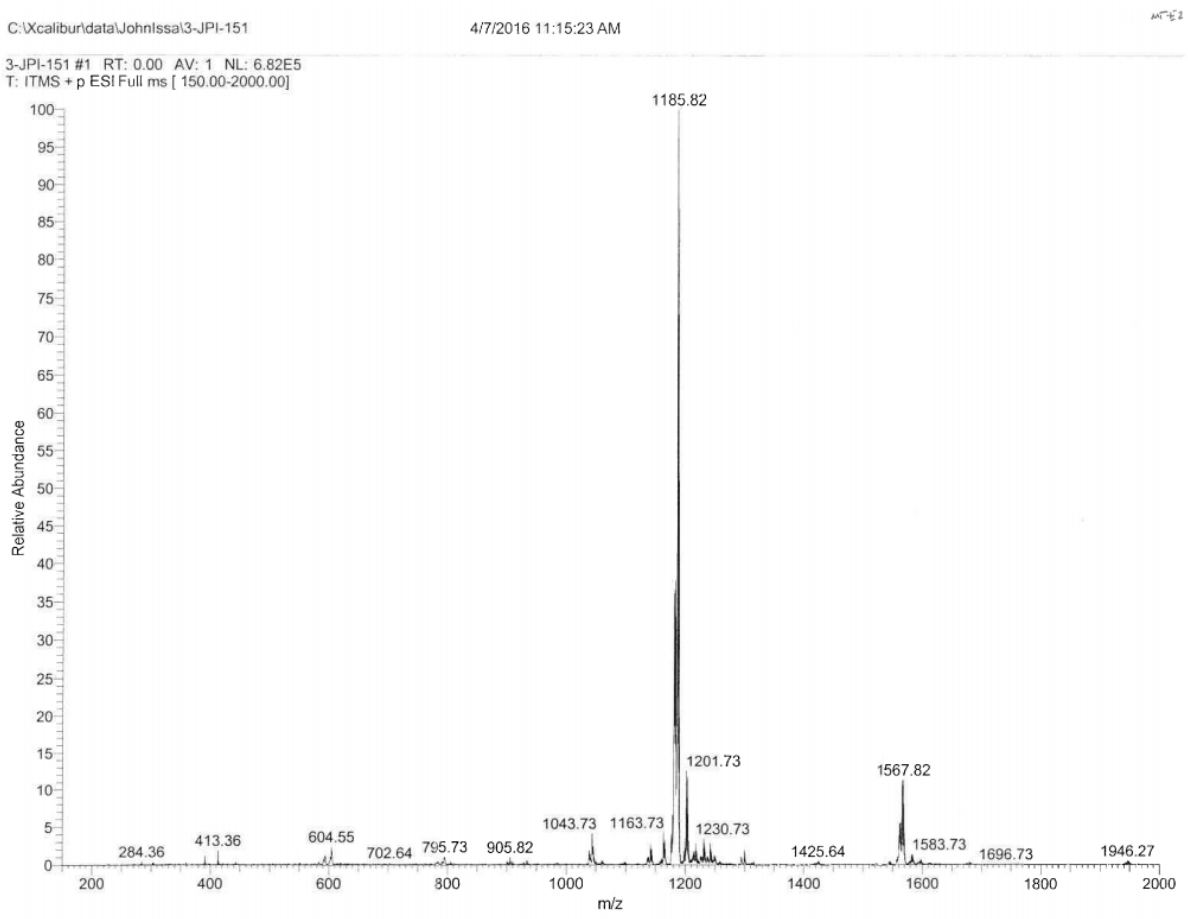

Figure 13. ESI-MS of MT-E2.

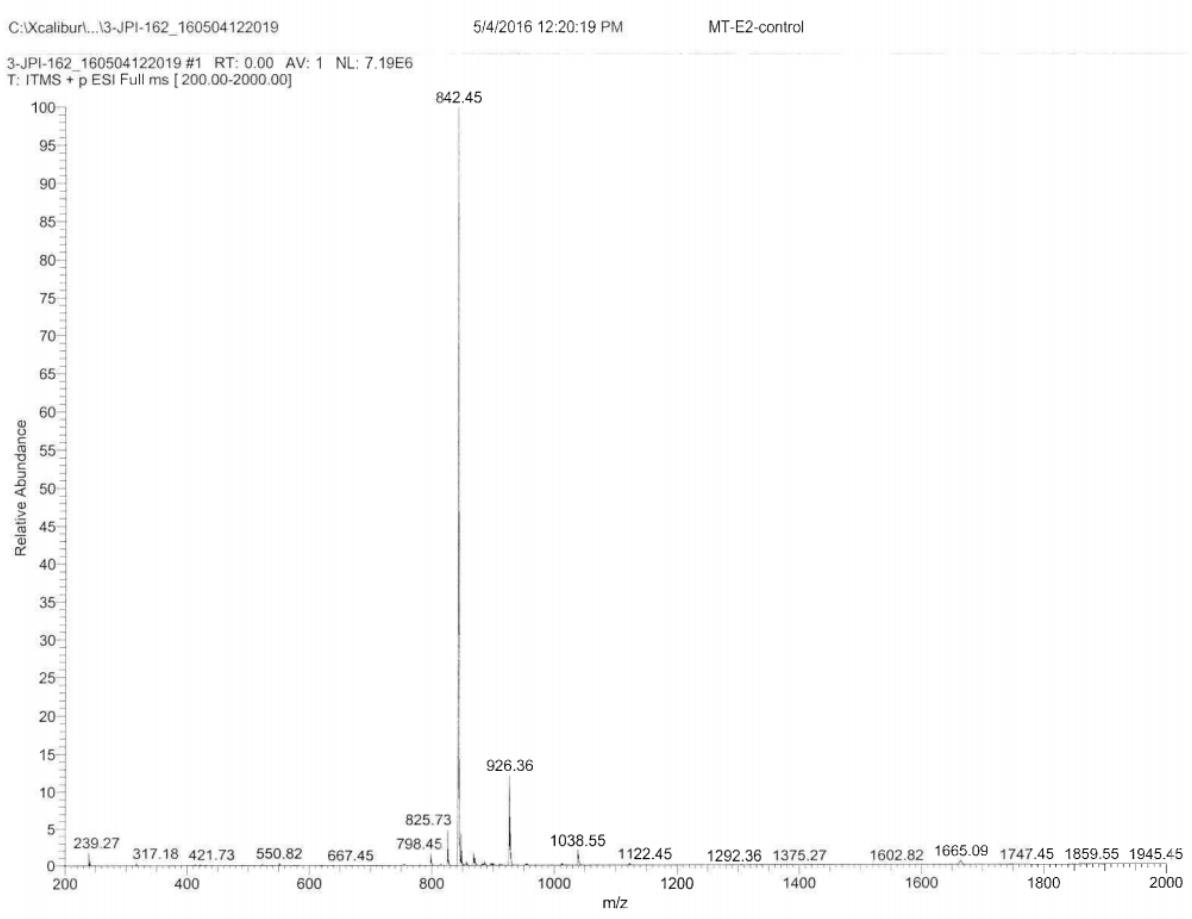

Figure 14. ESI-MS of MT-E2 control.

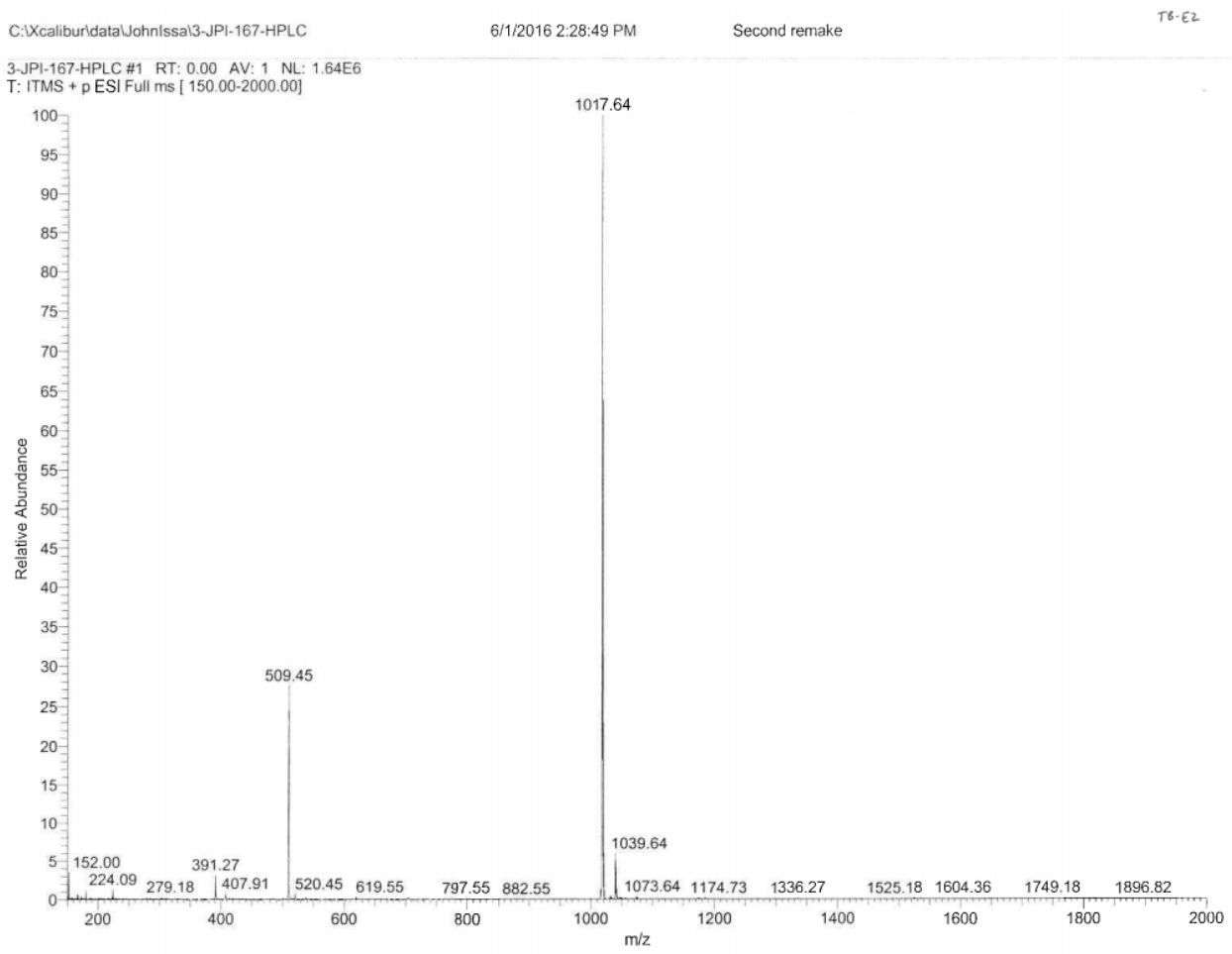

Figure 15. ESI-MS of TB-E2.

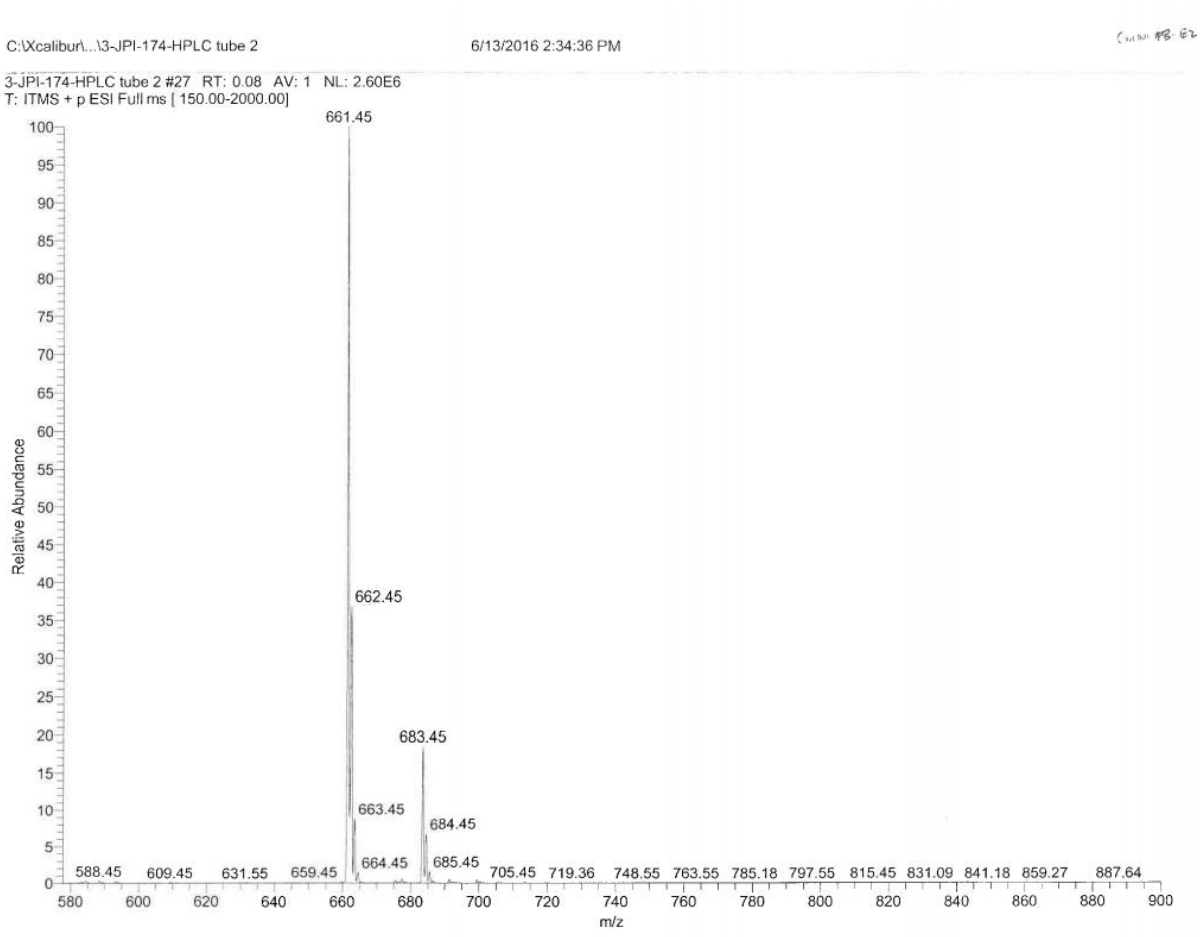

Figure 16. ESI-MS of TB-E2 control.

References

1. WHO. Global status report on noncommunicable diseases 2014. *World Health* 176 (2014). doi:ISBN 9789241564854

2. Libby, P.; Ridker, P. M.; Hansson, G. K. Progress and challenges in translating the biology of atherosclerosis. *Nature* **473,** 317–325 (2011).

3. Cunningham, K. S. & Gotlieb, A. I. The role of shear stress in the pathogenesis of atherosclerosis. *Lab. Investig.* **85,** 9–23 (2004).

4. Malek, A. M., Alper, S. L. & Izumo, S. Hemodynamic Shear Stress and Its Role in Atherosclerosis. *Jama* **282,** 2035–2042 (1999).

5. Bredt, D. S. & Snyder, S. H. Isolation of nitric oxide synthetase, a calmodulin-requiring enzyme. *Proc. Natl. Acad. Sci. U. S. A.* **87,** 682–5 (1990).

6. Deanfield, J. E., Halcox, J. P. & Rabelink, T. J. Endothelial function and dysfunction: Testing and clinical relevance. *Circulation* **115,** 1285–1295 (2007).

7. Denninger, J. W. & Marletta, M. A. Guanylate cyclase and the ·NO/cGMP signaling pathway. *Biochim. Biophys. Acta - Bioenerg.* **1411,** 334–350 (1999).

8. Lohmann, S. M., Vaandrager, A. B., Smolenski, A., Walter, U. & De Jonge, H. R. Distinct and specific functions of cGMP-dependent protein kinases. *Trends Biochem. Sci.* **22,** 307–12 (1997).

9. Kietadisorn, R., Juni, R. P. & Moens, A. L. Tackling endothelial dysfunction by modulating NOS uncoupling: new insights into its pathogenesis and therapeutic possibilities. *AJP Endocrinol. Metab.* **302,** E481–E495 (2012).

10. Mollnau, H. *et al.* Effects of angiotensin II infusion on the expression and function of NAD(P)H oxidase and components of nitric oxide/cGMP signaling. *Circ. Res.* **90,** E58-65 (2002).

11. Li, H. & Förstermann, U. Uncoupling of endothelial NO synthase in atherosclerosis and vascular disease. *Curr. Opin. Pharmacol.* **13,** 161–167 (2013).

12. Mestas, J. & Ley, K. Monocyte-endothelial cell interactions in the development of atherosclerosis. *Trends Cardiovasc. Med.* **18,** 228–32 (2008).

13. Moore, K. J., Sheedy, F. J. & Fisher, E. A. Macrophages in atherosclerosis: a dynamic balance. *Nat. Rev. Immunol.* **13,** 709–721 (2013).

14. Rajamäki, K. *et al.* Cholesterol Crystals Activate the NLRP3 Inflammasome in Human Macrophages: A Novel Link between Cholesterol Metabolism and Inflammation. *PLoS One* **5,** e11765 (2010).

15. Sprague, A. H. & Khalil, R. A. Inflammatory cytokines in vascular dysfunction and vascular disease. *Biochem. Pharmacol.* **78,** 539–552 (2009).

16. Oh, J. *et al.* Endoplasmic Reticulum Stress Controls M2 Macrophage Differentiation and Foam Cell Formation. *J. Biol. Chem.* **287,** 11629–11641 (2012).

17. Rudijanto, A. The role of vascular smooth muscle cells on the pathogenesis of atherosclerosis. *Acta Med. Indones.* **39,** 86–93

18. Tabas, I. Consequences and Therapeutic Implications of Macrophage Apoptosis in Atherosclerosis: The Importance of Lesion Stage and Phagocytic Efficiency. *Arterioscler. Thromb. Vasc. Biol.* **25,** 2255–2264 (2005).

19. Tabas, I. Macrophage death and defective inflammation resolution in atherosclerosis. *Nat. Rev. Immunol.* **10,** 36–46 (2010).

20. Maas, A. H. E. M. & Appelman, Y. E. A. Gender differences in coronary heart disease. *Neth. Heart J.* **18,** 598–602 (2010).

21. Rossi, R. *et al.* Menopause and cardiovascular risk. *Pathophysiol. Haemost. Thromb.* **32,** 325–328 (2003).

22. Kannel & et al. Diabetes and Cardiovascular Disease The Framingham. *Jama* **241,** 2035–2038 (1979).

23. Derby, C. A. *et al.* Lipid Changes During the Menopause Transition in Relation to Age and Weight: The Study of Women's Health Across the Nation. *Am. J. Epidemiol.* **169,** 1352–1361 (2009).

24. Grady, D. Management of Menopausal Symptoms. *N. Engl. J. Med.* **355,** 2338–2347 (2006).

25. Stampfer, M. J. *et al.* Postmenopausal estrogen therapy and cardiovascular disease: Ten-year follow-up from the Nurses' Health Study. *N. Engl. J. Med.* **325,** 756–762 (1991).

26. Stampfer, M. J. *et al.* A Prospective Study of Postmenopausal Estrogen Therapy and Coronary Heart Disease. *N. Engl. J. Med.* **313,** 1044–1049 (1985).

27. Wilson, P. W. F., Garrison, R. J. & Castelli, W. P. Postmenopausal Estrogen Use,

Cigarette Smoking, and Cardiovascular Morbidity in Women over 50. *N. Engl. J. Med.* **313,** 1038–1043 (1985).

28. Writing Group for the Women's Health Initiative Investigators. Risks and Benefits of Estrogen Plus Progestin in Healthy Postmenopausal Women: Principal Results From the Women's Health Initiative Randomized Controlled Trial. *JAMA J. Am. Med. Assoc.* **288,** 321–333 (2002).

29. Deroo, B. J. Estrogen receptors and human disease. *J. Clin. Invest.* **116,** 561–570 (2006).

30. Salpeter, S. R., Walsh, J. M. E., Greyber, E. & Salpeter, E. E. Brief report: Coronary heart disease events associated with hormone therapy in younger and older women. *J. Gen. Intern. Med.* **21,** 363–366 (2006).

31. Rossouw, J. E. *et al.* Postmenopausal Hormone Therapy and Risk of Cardiovascular Disease by Age and Years Since Menopause. *JAMA* **297,** (2007).

32. Haarbo, J. & Christiansen, C. The impact of female sex hormones on secondary prevention of atherosclerosis in ovariectomized cholesterol-fed rabbits. *Atherosclerosis* **123,** 139–44 (1996).

33. Clarkson, T. B. & Appt, S. E. Controversies about HRT—lessons from monkey models. *Maturitas* **51,** 64–74 (2005).

34. Hodis, H. N. & Mack, W. J. The timing hypothesis and hormone replacement therapy: A paradigm shift in the primary prevention of coronary heart disease in women. Part 1: Comparison of therapeutic efficacy. *J. Am. Geriatr. Soc.* **61,** 1005–1010 (2013).

35. Nelson, L. R. & Bulun, S. E. Estrogen production and action. *J. Am. Acad. Dermatol.* **45,** S116-24 (2001).

36. Cui, J., Shen, Y. & Li, R. Estrogen synthesis and signaling pathways during aging: from periphery to brain. *Trends Mol. Med.* **19,** 197–209 (2013).

37. Ascenzi, P., Bocedi, A. & Marino, M. Structure–function relationship of estrogen receptor α and β: Impact on human health. *Mol. Aspects Med.* **27,** 299–402 (2006).

38. Kumar, R. *et al.* The Dynamic Structure of the Estrogen Receptor. *J. Amino Acids* **2011,** 1–7 (2011).

39. Marino, M., Galluzzo, P. & Ascenzi, P. Estrogen signaling multiple pathways to impact gene transcription. *Curr. Genomics* **7,** 497–508 (2006).

40. Webb, P. *et al.* Estrogen Receptor Activation Function 1 Works by Binding p160 Coactivator Proteins. *Mol. Endocrinol.* **12,** 1605–1618 (1998).

41. Warnmark, A., Wikstrom, A., Wright, A. P. H., Gustafsson, J.-A. & Hard, T. The N-terminal Regions of Estrogen Receptor and Are Unstructured in Vitro and Show Different TBP Binding Properties. *J. Biol. Chem.* **276,** 45939–45944 (2001).

42. Brzozowski, A. M. *et al.* Molecular basis of agonism and antagonism in the oestrogen receptor. *Nature* **389,** 753–758 (1997).

43. Maggi, A. Liganded and unliganded activation of estrogen receptor and hormone replacement therapies. *Biochim. Biophys. Acta - Mol. Basis Dis.* **1812,** 1054–1060 (2011).

44. Ruff, M., Gangloff, M., Marie Wurtz, J. & Moras, D. Estrogen receptor transcription and transactivation Structure-function relationship in DNA- and ligand-binding domains of estrogen receptors. *Breast Cancer Res.* **2,** 353 (2000).

45. Tamrazi, A., Carlson, K. E., Daniels, J. R., Hurth, K. M. & Katzenellenbogen, J. A. Estrogen Receptor Dimerization: Ligand Binding Regulates Dimer Affinity and DimerDissociation Rate. *Mol. Endocrinol.* **16,** 2706–2719 (2002).

46. Aranda, A. & Pascual, A. Nuclear hormone receptors and gene expression. *Physiol. Rev.* **81,** 1269–304 (2001).

47. Yuan, Y. Steroid Receptor Coactivator-3 Is Required for Inhibition of Neointima Formation by Estrogen. *Circulation* **105,** 2653–2659 (2002).

48. Mendelsohn, M. E. & Karas, R. H. Estrogen and the blood vessel wall. *Curr. Opin. Cardiol.* **9,** 619–26 (1994).

49. Mendelsohn, M. E. Protective effects of estrogen on the cardiovascular system. *Am. J. Cardiol.* **89,** 12E–17E; discussion 17E–18E (2002).

50. He, H. *et al.* Vascular Endothelial Growth Factor Signals Endothelial Cell Production of Nitric Oxide and Prostacyclin through Flk-1/KDR Activation of c-Src. *J. Biol. Chem.* **274,** 25130–25135 (1999).

51. Wang, C., Qian, X., Sun, X. & Chang, Q. Angiotensin II increases matrix metalloproteinase 2 expression in human aortic smooth muscle cells via AT1R and ERK1/2. *Exp. Biol. Med.* **240,** 1564–1571 (2015).

52. Nguyen, M. *et al.* Vascular expression of E-selectin is increased in estrogen-receptor-negative breast cancer: a role for tumor-cell-secreted interleukin-1 alpha.

Am. J. Pathol. **150,** 1307–14 (1997).

53. Ashcroft, G. S. *et al.* Estrogen accelerates cutaneous wound healing associated with an increase in TGF-beta1 levels. *Nat. Med.* **3,** 1209–15 (1997).

54. Shanker, G., Sorci-Thomas, M. & Adams, M. R. Estrogen modulates the inducible expression of platelet-derived growth factor mRNA by monocyte/macrophages. *Life Sci.* **56,** 499–507 (1995).

55. Kim, C. J., Jang, H. C., Cho, D. H. & Min, Y. K. Effects of hormone replacement therapy on lipoprotein(a) and lipids in postmenopausal women. *Arterioscler. Thromb. a J. Vasc. Biol.* **14,** 275–81 (1994).

56. PIETRAS, R. J. & SZEGO, C. M. Specific binding sites for oestrogen at the outer surfaces of isolated endometrial cells. *Nature* **265,** 69–72 (1977).

57. Chen, Z. *et al.* Estrogen receptor α mediates the nongenomic activation of endothelial nitric oxide synthase by estrogen. *J. Clin. Invest.* **103,** 401–406 (1999).

58. Collins, P. & Webb, C. Estrogen hits the surface. *Nat. Med.* **5,** 1130–1131 (1999).

59. Szego, C. M. & Davis, J. S. Adenosine 3',5'-monophosphate in rat uterus: acute elevation by estrogen. *Proc. Natl. Acad. Sci. U. S. A.* **58,** 1711–8 (1967).

60. Mendelsohn, M. E. & Karas, R. H. Rapid progress for non-nuclear estrogen receptor signaling. *Journal of Clinical Investigation* **120,** 2277–2279 (2010).

61. Muller-Delp, J. M. *et al.* Regulation of nitric oxide-dependent vasodilation in coronary arteries of estrogen receptor-α-deficient mice. *Am. J. Physiol. - Hear. Circ. Physiol.* **285,** H2150–H2157 (2003).

62. Wyckoff, M. H. *et al.* Plasma Membrane Estrogen Receptors Are Coupled to Endothelial Nitric-oxide Synthase through G i. *J. Biol. Chem.* **276,** 27071–27076 (2001).

63. Haynes, M. P. Src Kinase Mediates Phosphatidylinositol 3-Kinase/Akt-dependent Rapid Endothelial Nitric-oxide Synthase Activation by Estrogen. *J. Biol. Chem.* **278,** 2118–2123 (2003).

64. Haynes, M. P. *et al.* Membrane Estrogen Receptor Engagement Activates Endothelial Nitric Oxide Synthase via the PI3-Kinase-Akt Pathway in Human Endothelial Cells. *Circ. Res.* **87,** 677–682 (2000).

65. Sessa, W. C. *et al.* Regulation of endothelium-derived nitric oxide production by

the protein kinase Akt. *Nature* **399,** 597–601 (1999).

66. Paniagua, O. A., Bryant, M. B. & Panza, J. A. Role of Endothelial Nitric Oxide in Shear Stress-Induced Vasodilation of Human Microvasculature : Diminished Activity in Hypertensive and Hypercholesterolemic Patients. *Circulation* **103,** 1752–1758 (2001).

67. NASEEM, K. The role of nitric oxide in cardiovascular diseases. *Mol. Aspects Med.* **26,** 33–65 (2005).

68. Marino, M. Distinct Nongenomic Signal Transduction Pathways Controlled by 17beta -Estradiol Regulate DNA Synthesis and Cyclin D1 Gene Transcription in HepG2 Cells. *Mol. Biol. Cell* **13,** 3720–3729 (2002).

69. Marino, M. Biphasic Estradiol-induced AKT Phosphorylation Is Modulated by PTEN via MAP Kinase in HepG2 Cells. *Mol. Biol. Cell* **14,** 2583–2591 (2003).

70. Thomas, R. S., Sarwar, N., Phoenix, F., Coombes, R. C. & Ali, S. Phosphorylation at serines 104 and 106 by Erk1/2 MAPK is important for estrogen receptor- activity. *J. Mol. Endocrinol.* **40,** 173–184 (2008).

71. Driggers, P. H. & Segars, J. H. Estrogen action and cytoplasmic signaling pathways. Part II: the role of growth factors and phosphorylation in estrogen signaling. *Trends Endocrinol. Metab.* **13,** 422–7 (2002).

72. Campbell, R. A. *et al.* Phosphatidylinositol 3-Kinase/AKT-mediated Activation of Estrogen Receptor α. *J. Biol. Chem.* **276,** 9817–9824 (2001).

73. Filardo, E. J., Quinn, J. A., Bland, K. I. & Frackelton, A. R. Estrogen-Induced Activation of Erk-1 and Erk-2 Requires the G Protein-Coupled Receptor Homolog, GPR30, and Occurs via Trans -Activation of the Epidermal Growth Factor Receptor through Release of HB-EGF. *Mol. Endocrinol.* **14,** 1649–1660 (2000).

74. Filardo, E. J., Quinn, J. A., Frackelton, A. R. & Bland, K. I. Estrogen Action Via the G Protein-Coupled Receptor, GPR30: Stimulation of Adenylyl Cyclase and cAMP-Mediated Attenuation of the Epidermal Growth Factor Receptor-to-MAPK Signaling Axis. *Mol. Endocrinol.* **16,** 70–84 (2002).

75. Chambliss, K. L. *et al.* Non-nuclear estrogen receptor alpha signaling promotes cardiovascular protection but not uterine or breast cancer growth in mice. *J. Clin. Invest.* **120,** 2319–2330 (2010).

76. Wright, J. S. *et al.* A-CD Estrogens. I. Substituent Effects, Hormone Potency, and

Receptor Subtype Selectivity in a New Family of Flexible Estrogenic Compounds. *J. Med. Chem.* **54,** 433–448 (2011).

77. Madak-Erdogan, Z. *et al.* Design of pathway preferential estrogens that provide beneficial metabolic and vascular effects without stimulating reproductive tissues. *Sci. Signal.* **9,** ra53-ra53 (2016).

78. Murray, D., Ben-Tal, N., Honig, B. & McLaughlin, S. Electrostatic interaction of myristoylated proteins with membranes: simple physics, complicated biology. *Structure* **5,** 985–9 (1997).

79. Wu, Y., Vendome, J., Shapiro, L., Ben-Shaul, A. & Honig, B. Transforming binding affinities from three dimensions to two with application to cadherin clustering. *Nature* **475,** 510–513 (2011).

80. Caliceti, P. Pharmacokinetic and biodistribution properties of poly(ethylene glycol)–protein conjugates. *Adv. Drug Deliv. Rev.* **55,** 1261–1277 (2003).

81. Monaco, H. L. The transthyretin-retinol-binding protein complex. *Biochim. Biophys. Acta - Protein Struct. Mol. Enzymol.* **1482,** 65–72 (2000).

82. Penchala, S. C. *et al.* AG10 inhibits amyloidogenesis and cellular toxicity of the familial amyloid cardiomyopathy-associated V122I transthyretin. *Proc. Natl. Acad. Sci.* **110,** 9992–9997 (2013).

83. Ingenbleek, Y. & Young, V. Transthyretin (Prealbumin) in Health and Disease: Nutritional Implications. *Annu. Rev. Nutr.* **14,** 495–533 (1994).

84. Penchala, S. C. *et al.* A biomimetic approach for enhancing the in vivo half-life of peptides. *Nat. Chem. Biol.* **11,** 793–798 (2015).

85. Lorber, D. Importance of cardiovascular disease risk management in patients with type 2 diabetes mellitus. *Diabetes, Metab. Syndr. Obes. Targets Ther.* 169 (2014). doi:10.2147/DMSO.S61438

86. Knudsen, L. B. *et al.* Potent Derivatives of Glucagon-like Peptide-1 with Pharmacokinetic Properties Suitable for Once Daily Administration. *J. Med. Chem.* **43,** 1664–1669 (2000).

87. Marso, S. P. *et al.* Liraglutide and Cardiovascular Outcomes in Type 2 Diabetes. *N. Engl. J. Med.* **375,** 311–322 (2016).

88. Xu, P. *et al.* Estrogen receptor-α in medial amygdala neurons regulates body weight. *J. Clin. Invest.* **125,** 2861–76 (2015).

89. Lindheim, S. R. *et al.* The route of administration influences the effect of estrogen on insulin sensitivity in postmenopausal women**Supported, in part, by the National Institutes of Health National Center for Research Resources of the General Clinical Research Centers grant M0. *Fertil. Steril.* **62,** 1176–1180 (1994).

90. Ferreira, F. *et al.* Endocytosis of G Protein-Coupled Receptors Is Regulated by Clathrin Light Chain Phosphorylation. *Curr. Biol.* **22,** 1361–1370 (2012).

91. Finan, B. *et al.* Targeted estrogen delivery reverses the metabolic syndrome. *Nat. Med.* **18,** 1847–56 (2012).

92. Herzog, H. L., Gnoj, O., Mandell, J., Nathnson, G. G. & Vigevani, A. Wagner-Meerwein rearrangements. IV. Some reassignments of structure. *J. Org. Chem.* **32,** 2906–2910 (1967).

93. Brabandere, V. I. De, Thienpont, L. M., Stockl, D. & Leenheerzy, A. P. De. 13C-NMR and mass spectral data of steroids with a 17 , 17-dialkyl-l8-nor-l3 (14) -ene substructure. **38,** 780–789 (1997).

Part 3

Chapter 1: Introduction

1.1 Recap of Cardiovascular Disease

1.1.1 Cardiovascular Disease Pathophysiology

Cardiovascular diseases are currently the leading cause of death worldwide.[1] The health burden is compounded by the economic cost, and in 2010, the global cost of CVD approximately $863 billion dollars.[2] Most cardiovascular disease are attributed to atherosclerosis, characterized by persistent inflammation in the arterial wall and the formation of atherosclerotic lesions or plaques.[3] Eventually, the plaque enters a vulnerable state. The vulnerable plaque state indicates imminent rupture of the fibrous cap leading to thrombus formation. Thrombus formation can result in coronary occlusion, the culprit behind heart attacks and strokes currently afflicting millions of Americans.

The immune system plays a central role in atherosclerosis from initiation to exacerbation. Indeed, defective resolution of inflammation leads to a chronic inflammatory state within the atherosclerotic plaque, which can lead to rupture of the plaque and subsequent acute coronary events (further elaborated in Part II). Regarding the initiation of atherosclerosis, early inflammatory stages are attributed to low density lipoproteins (LDLs). LDLs aggregate in arterial branches, where blood flow is irregular and shear stress is low (<5 dynes/cm^2) promoting their deposition.[4,5]

1.3 Low Density Lipoproteins Function and Dysfunction

1.2.1 LDL Action and Structure

LDLs are major cholesterol carriers (~70% of all cholesterol) for tissues that rely on cholesterol for important biosynthetic processes such as membrane formation and steroid synthesis.[6] Approximately 45% (by weight) of LDL are free cholesterols and cholesteryl esters, whereas the remaining 55% are protein (23%), phospholipids (20%), and triacylgyclerols 10%).[7] Regarding structure, LDLs have two main regions: the surface and the core. The LDL core consists of cholesteryl esters and triacylglycerols whereas the surface of LDLs contain unesterified cholesterol, phosphatidylcholine, sphingomyelin and apolipoprotein B-100 (apoB-100).[8] The surface is imperative for interaction with LDL receptor (LDLR) for either uptake by various tissues or recycling by hepatocytes.

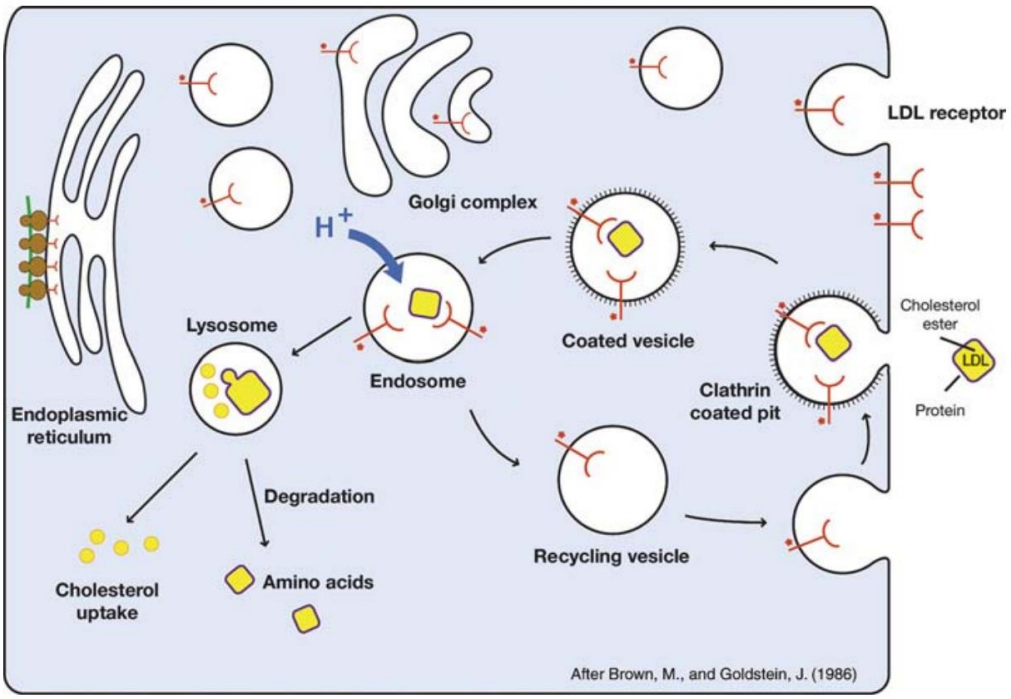

Figure 19. Clathrin mediated endocytosis of LDLs. LDLs in clathrin pits recognize LDLs, and form endosomes. The acidic pH of the endosome triggers release of the LDL for further degradation. Reprinted with permission.[50]

1.2.2 Low Density Lipoprotein Receptor Function

LDLR is a type I transmembrane receptor found in clathrin coated pits on the plasma membrane of cells. It consists of a ligand binding region, an epidermal growth factor (EGF)-precursor homology region, an O-linked glycan region, a transmembrane domain and cytosolic domain.[9] The ligand binding region is composed of seven cysteine-rich repeats oriented into two loops stabilized by the cofactor calcium. The ligand binding region is responsible for binding to apoB-100 in LDLs through cysteine-rich repeats. Upon binding to apoB-100, the adaptor protein, autosomal recessive hypercholesterolemia (ARH), binds to the NPVY motif on the cytosolic domain of LDLR.[10] ARH then binds to the clathrin-

binding AP2 adaptor complex via the β2 subunit to mediate clathrin dependent endocytosis of LDLs. Within the endosome, the acidic pH facilitates a conformational change. The ligand binding domain folds back in order to displace the bound LDL with the β-propeller shaped EGF-precursor homology region, stabilized by Ca^{2+}.[11] The displaced LDL is subsequently digested by lysozymes to release cholesterol. Concerning LDLR, if the enzyme Proprotein convertase subtilisin/kexin type 9 (PCSK9) binds LDLR, it undergoes further catabolism pathways.[12] If unbound, LDLR is recycled and presented on the plasma membrane once more.

1.2.3 Low Density Lipoprotein Oxidation

However, during oxidation LDLs are modified such that LDLR is unable to bind. The oxidation process of LDL is complex with several proposed oxidation mechanisms involving several performers such as lipoxygenase, NADPH oxidase, and peroxidase. The initiation of oxidation can be accomplished by lipoperoxides or reactive oxygen species synthesized and released from endothelial cells or macrophages. Subsequent conglomerate oxidation reactions occur, oxidizing polyunsaturated fatty acids, fragmenting the LDL and generating numerous oxidation products in addition to free radicals. The products of LDL oxidation and fragmentation are many, and include oxidized cholesterols, malondialdehyde, modified phospholipids, and fatty acid peroxides.[13] Further, apoB is degraded and consequently modified, participating in tyrosine cross-

linking, acetylation and other residue modifications. Indeed, conjugation of fragmented apoB to malondialdehyde allows macrophages to uptake oxLDLs through its scavenger receptors.[14] Oxidation can occur at varying degrees within the arterial wall, giving rise to two main subtypes of oxidized LDLs, minimally modified LDLs (MM-LDLs) and fully oxidized LDLs (oxLDL).

1.3 Innate and Adaptive Immune System in Atherosclerosis

1.3.1 Macrophages and their Scavenger Receptors

The drastic changes that LDL undergoes after oxidation allows for the scavenger receptors to mediate uptake of MM-LDLs and oxLDLs.[15] Scavenger receptor AI (SR-AI), and scavenger receptor AII (SR-AII) are class A scavenger receptors on macrophages capable of recognizing oxLDLs as well as acetylated LDLs (acLDLs) for their eventual uptake.[16] However, recognition of these LDLs is dependent on oxidation, acetylation and succinylation of lysine residues of apoB.[16] Oxidation of at least 16% of lysine residues on apoB is sufficient for uptake by macrophages, whereas acetylation and succinylation of at least 60% of lysine residues of apoB is necessary for uptake.[16] However, acLDLs have a higher affinity for SR-AI and SR-AII on macrophages.[17] Class B scavenger receptors such, as CD36, expressed on both macrophages bind selectively to oxLDLs and at a faster rate than class A scavenger receptors.[18] CD36 mediates oxLDL uptake through binding of

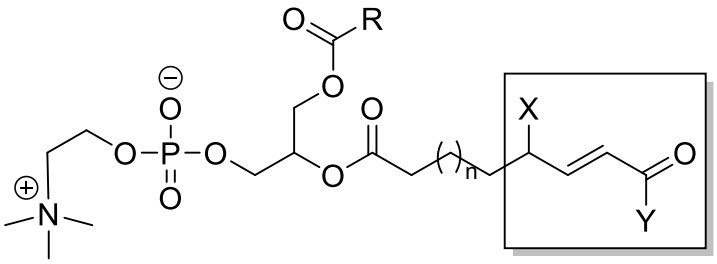

Figure 20. Oxidized phosphatidylcholine is recognized by the α,β-unsaturated γ-hydroxy aldehyde carboxylate moiety shown in the box.

modified phospholipids rather than binding of modified apoB. Indeed, methylation of apoB lysine residues attenuated oxLDL uptake by class A receptors, but not with CD36, implicating the minimal role of apoB in oxLDL uptake by CD36.[18] Instead, in macrophages, CD36 recognizes oxidized phospholipids via an α,β-unsaturated γ-hydroxy aldehyde/carboxylate moiety (Fig. 2).[19] Further, class E receptors on macrophages have been shown to preferentially bind MM-LDLs. Interestingly, MM-LDL binding to class E receptors is contingent on apoB, as modifications to apoB can impact MM-LDL binding, implicating the tethering of MM-LDLs to apoB.[15,20] MM-LDLs also stimulate Toll-like Receptor 4 (TLR-4) as well as increase uptake of oxLDL implicating the role of MM-LDL and perhaps TLR-4 in increasing scavenger receptors for the uptake of oxLDL.

In addition to macrophages, dendritic cells express scavenger receptors that participate in the uptake of oxLDL. Both class B scavenger receptor CD-36 and class E scavenger receptor LOX-1 are revealed to have a role in oxLDL uptake as inhibition of

these receptors reduced such uptake.[21] Further, DCs have been shown to uptake acLDLs in a SR-A dependent manner, exhibiting similarities to macrophage function.[22]

1.3.2 Bridging the Innate and Adaptive Immune Systems

Although the uptake of oxLDLs can elicit foam cell formation and progression of atherosclerosis, the innate immune response is essential for the adaptive immune response. Dendritic cells process oxLDLs and present antigens such as phosphorylcholine or peptides of apoB-100, and migrate to the draining lymph node.[23] In the draining lymph node, dendritic cells present these processed antigens to naïve $CD4^+$ T-cells, activating them to adopt a T-helper 1 (T_H1) or T_H2 phenotype. The development of T-cells into T-helper cells hinges on the interaction between the class II MHC (with processed antigen) and the T-cell receptor of the $CD4^+$ T-cell, several co-stimulatory molecule interactions and paracrine signaling.[24] DC-T-cell activation stimulates T_H2 differentiation through OX40-OX40L co-stimulatory interaction as well as IL-6 and IL-13 paracrine signaling.[24]

1.3.3 T-Cell and B-Cell Responses

T-cell differentiation into a T_H2 phenotype is essential for atheroprotective effects. Daughtery et al. discovered that upon immunization with malondialdehyde conjugated LDL, a large T_H2 response was observed.[25] More importantly, these T_H2 cells were responsible for the secretion of the cytokine IL-5, which stimulated B-1 cells to produce

IgM antibody. Indeed, IL-5$^{-/-}$ mice were unable to recapitulate the same antibody response. IgM is critical and reduces the progression of atherosclerotic lesions. In IgM deficient mice, lesion progression was accelerate, resulting in significant larger plaques.[26] When treated with polyclonal IgM antibodies, lesion size and atherosclerosis was attenuated.[27] The atheroprotective effects of IgM can be attributed to general anti-inflammatory effects. In the same study, Cesena et al. revealed that treatment with polyclonal IgM antibodies were able to reduce $CD4^{+}CD28^{+}$ cells, responsible for exacerbation of atherosclerotic lesions.[27] IgM in coordination with complement activation, also elicits efferocytosis, or the clearance of apoptotic cells, implicating its role in the resolution of inflammation in atherosclerosis.[28] In early atherogenesis, monoclonal IgM antibodies bind to and sequester oxidized phosphatidylcholine, namely POVPC, precluding uptake by macrophages and subsequent foam cell formation. Yet B-1 cell activation does not rely exclusively on T_H2 T-cells, but can participate in T-cell independent signaling. In some cases, B-cell receptors (BCR) on naïve B-cells can directly bind to antigen, initiating antigen cross-linking.[29] The activated plasma cell now can directly produce IgM. Further, BCRs after binding to antigen can coordinate with TLRs for activation. This relies on a second signal, such as lipopolysaccharide (LPS), to produce a large, robust, antibody response. However, all three B-cell activation pathways eventually lead to class-switching from IgM to IgG.

1.3.4 Antibody Class-Switching

This phenomenon, initiated by activation-induced cytosine deaminase (AID) can deplete IgM production while enhancing IgG production.[30] During active transcription of the antibody gene, AID binds to unwound single stranded DNA and deaminates cytosine, mutating it to uracil. Uracil-DNA glycosylase subsequently removes the pyrimidine ring of uracil leaving behind an apurinic/apyrimidinic (AP) site. AP endonuclease 1 mediates the excision of the leftover deoxyribose and phosphate to form a single stranded nick. Interestingly, single stranded nicks are converted to double-stranded breaks (mechanism unknown). With the involvement of Ku proteins, the Artemis:DNA-PKcs complex and DNA ligase IV/XRCC4, non-homologous end joining occurs. Overall, the excision and rejoining of regions within the gene results in class-switching of the antibody.

The role of IgG in atherosclerosis is unclear, but there are studies that implicate its role in atherogenesis. In humans, oxLDL-specific IgG is positively correlated with atherosclerotic lesion progression.[31] Klimov et al. utilized immunocomplexes consisting of LDL and anti-apoB IgG in rabbits to determine atherogenicity.[32] The rate of macropinocytosis for these immunocomplexes were much faster than free LDL due to IgG binding to its respective Fcγ receptor. This uptake resulted in increased inflammatory cytokine secretion by macrophages, a likely result due to the pro-inflammatory nature of LDLs.

1.4 Vaccines for Atherosclerosis

1.4.1 Vaccinating with Streptococcus pneumoniae

The previously mentioned study elucidating the sequestering ability of phosphorylcholine binding monoclonal IgM antibodies prompted the further investigation of phosphorylcholine. Sequence analysis of the genes encoding these "EO" monoclonal IgM antibodies revealed 100% homology to the T(EPC)15 monoclonal IgA anti-PC antibody (T15), an antibody that is naturally produced after immunization with *Streptococcus pneumoniae.*[33] The T15 antibody normally binds to the phosphorylcholine moiety of lipoteichoic acid found on the peptidoglycan cell wall of gram-positive bacteria. Interestingly, the T15 antibody can bind to oxidized phosphatidylcholine and the EO monoclonal IgM antibodies can bind to phosphorylcholine on pneumococcal cell wall polysaccharides.[33] Thus, Binder et al. explored the use of *S. pneumoniae* explore its potential in an atherosclerosis model (*Ldlr*$^{-/-}$ mice).[34] Mice were immunized with heat killed *S. pneumoniae* potentiated with Freund's adjuvant. Immunizations elicited a significant IgM production response, with minimal IgG. The IgM antibody produced was capable of binding both cell wall polysaccharides and oxLDL as well as reduce atherosclerotic lesion progression. Further, Freund's adjuvant was not required to mediate atheroprotective effects, as within the aortic origin, atherosclerosis was 21% less in the immunized group than in the control (PBS) group.

This study points to the importance of phosphorylcholine in mediating an IgM response for atheroprotective effects. Thus, we hypothesize that instead of using bacterium, phosphorylcholine bearing phospholipids in the form of liposomes could be utilized for a more direct provision of antigen to T-cells and B-cells.

1.4.2 Liposome Design Considerations

Liposomes are composed of amphiphilic lipids that spontaneously organize into micelle-like structures in aqueous solution. Indeed, phospholipids have been most commonly employed to synthesize liposomes and to elicit immune responses. However, there are many design parameters that must be assessed for the synthesis of liposomes including size, lamellarity, charge, and membrane fluidity.[35] Size can be determined by the technique used to prepare the liposomes. Sonication either using a bath or probe sonicator can be utilized to generate vesicles that range from 15-50 nm. However, sonicated liposomes are metastable, and often fuse to form larger vesicles, generating a heterogenous pool of liposomes with a high polydispersity index (PDI).[36] High PDI and heterogeneity renders each batch irreproducible.

Extrusion is accomplished by an extruder (hence the name) consisting of two syringes that pass a heterogenous liposome mixture through a polycarbonate membrane with nM sized pores, generating vesicles that are slightly larger than the membrane size.

These liposomes are mostly homogenous with low PDI and are reproducible from batch to batch.[37] Size can also impact entrance into the lymph. It has been shown that molecules <200 nm readily diffuse into the lymph, whereas molecules larger than 200 nm rely on dendritic cells to access the lymph.[38] Since B-cell maturation occurs at germinal centers located in the lymph node, delivery of antigen to the B-cell would require a liposome size <200 nm.

Lamellarity can be controlled and either unilamellar or multilamellar liposomes can be generated. Multilamellar liposomes can elicit a larger immune response, particularly with IgG production, though mutilamellarity is not homogenous among liposomes.[39] As such, unilamellar liposomes are mostly utilized in liposome formulations.

Liposome charge can be regulated by lipid composition. In OVA encapsulated liposomes, positively charged liposomes generated larger antibody (IgG) responses than negatively charged liposomes.[40–42] Neutral liposomes were unable to produce comparable IgG responses to either positively or negatively charged liposomes, implicating the importance of non-neutral liposomes for immunogenicity.[40–42]

Lastly, membrane fluidity, as determined by the gel-liquid crystal transition temperature, plays a role in antibody response. Typically, the higher the transition temperature, the greater the antibody response. Further, it has been shown that out of several phosphatidylcholine (PC) lipid formulations, 1,2-distearoyl-*sn*-glycero-3-

phosphocholine (DSPC) containing lipids produced the highest response. Indeed, DSPC had the highest transition temperatures of all the PC lipid formulations tested.[43] A study performed by Bakouche et al., revealed that in gross cell surface antigen encapsulated liposomes, the optimal formulation for antibody response was 7:2:1 phosphatidylcholine (PC):Cholesterol (Chol):dicetylphosphate.[43,44]

Considering these parameters, two liposome formulations to be synthesized by extrusion are proposed. The first is a 9:1 DSPC:Chol liposome (PC), as phosphorylcholine, the headgroup of PC is the primary antigen for eliciting IgM responses. The second is a 7:2:1 DSPC: Phosphatidylserine (PS):Chol liposome (PS), similar to that utilized by Bakouche et al. DCP is utilized for the negative charge it conferred for the liposome, and replacing DCP with PS will accomplish likewise. Addition of PS to liposomes also attenuates the development of atherosclerotic lesions warranting its use in our liposome formulations. Further, a 2:1 PS:Chol ratio rather than a 1:2 PS:Chol ratio was used due to these atheroprotective effects. Preliminary experiments (data not shown) necessitated the inclusion of cholesterol for homogeneous liposome formation, and was thus included in each of the formulations. Since liposomes that are >200 nm are incapable of independently penetrating into the lymph, a membrane pore size of 100 nm was chosen. Thus, liposomes formed after extrusion will be slightly larger than 100 nm. The liposomes were chosen to be unilamellar as introducing multilamellarity also introduces variability from batch to

batch. After an initial proof of concept that these liposomes can induce anti-PC IgM production, formulations that encapsulate inhibitors of cytidine deaminase (e.g. valproic acid) will be synthesized to prevent class switching from IgM to IgG.

Chapter 2: Experimental Section

All chemicals were purchased at the highest possible purity from Sigma-Aldrich. The lipid extruder, membrane, filter supports, Hamilton GASTIGHT® syringes, and lipids were purchased from Avanti®. Size distribution of liposomes was determined by dynamic light scattering from a Malvern Zetasizer (courtesy of Professor Sam Thomas).

Sonication of liposomes was carried out according to the "Morrissey Lab Protocol for Preparing Phospholipid Vesicles (SUV) by Sonication."[45] DSPC (2.1 mg, 2.0 µmol) was dissolved in 2.6 mL HEPES buffer (140 mM NaCl, 20 mM HEPES buffer, pH 7.5, 0.02% (w/v) sodium azide). The lipids were suspended and hydrated for one hour at >55°C (transition temperature of DSPC[46]) with intermittent vortexing. The heterogeneous liposome mixture was sonicated with a Branson 2800 Ultrasonic Bath for one hour above the DSPC transition temperature.

The extruder was prepared as per Avanti manufacturing instructions. Two filter supports were pre-wet in 0.01 M phosphate buffered saline (P.B.S.) and placed on top of the membrane support. A pre-wet 0.1 µm membrane was placed on the membrane support and an identical membrane support with filter supports was placed atop the membrane, essentially "sandwiched."

Extrusion of liposomes was carried out according to the "Morrissey Lab Protocol for Preparing Phospholipid Vesicles by Extrusion."[47] The PC formulation consisted of DSPC (9.5 mg, 12.0 µmol) and Chol (0.5 mg, 1.3 µmol). The PS formulation consisted of DSPC (8.27 mg, 10.5 µmol) PS (1.15 mg, 3.0 µmol) and Chol (0.58 mg, 1.49 µmol). Stock chloroform solutions of each phospholipid were utilized for each formulation. Chloroform was dried with a gentle stream of Ar to obtain thin lipid films. The film was dried *in vacuo* for at least 3 hrs. The lipid films were hydrated with 4 mL -0.01 M P.B.S. in a water bath heated to >55°C (transition temperature) for one hour with intermittent vortexing. The hydrated films were freeze-thawed (5x) using a dry ice-acetone bath and a water bath with a temperature >55°C. The prepared extruder was heated above the transition temperature and syringes were pre-heated. The heterogenous liposome mixtures was passed through the membrane for a total of 21 passes. Extruded liposomes were stored at 4°C and Size distribution of liposomes was determined by dynamic light scattering from a Malvern Zetasizer (courtesy of Professor Sam Thomas).

Immunizations in mice were completed by Dr. Henry Wortis from the Tufts Medical Center. Six C57BL/6 mice (7-8 weeks old) were split into three groups: Control (received P.B.S.), PC, and PS. Mice were immunized with 0.2 mL of the liposome suspension or P.B.S. every two weeks. Mice tails were bled weekly and subsequently centrifuged to obtain blood serum. IgM and IgG antibody production was detected by enzyme-linked immunosorbent assay (ELISA) with PC-BSA as the antigen.

Chapter 3: Results and Discussion

3.1 Liposome Characterization

Liposomes composed solely of DSPC were initially generated by sonication to investigate the size distribution of liposomes. However, the PDI was very high (0.647) indicating a broad range of liposomal sizes, confirming that sonication produces a heterogenous mixture of liposomes (Fig 3.). Generally, a polydispersity less than <0.1 indicates a monodispersity.[48,49] Therefore, it was concluded that sonication would not be appropriate for liposomal preparations.

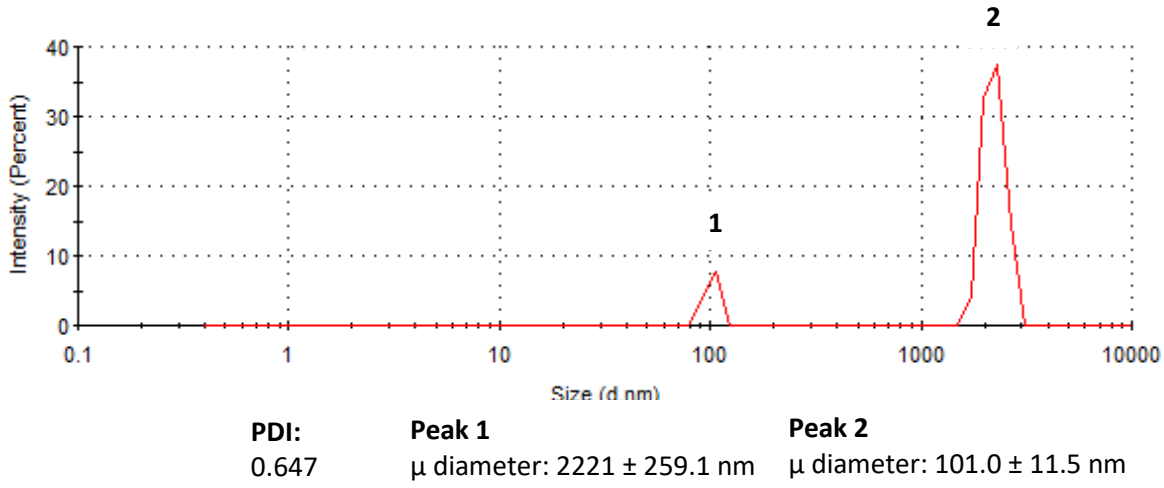

Figure 21. Sonicated liposomes were analyzed by dynamic light scattering. A heterogeneous mixture is shown above with two major populations indicated by the two peaks.

Liposomes generated by extrusion instead had a PDI much lower than those produced by sonication. Although mean diameter and PDI can vary slightly from batch to batch, PS liposomes the two parameter values ranged from ~110-150 nm and 0.03-0.11, respectively (Fig. 4). PC liposomes were slightly larger and ranged from ~130-170 nm and 0.15-0.20 for the two parameters, respectively (Fig. 5). The PC liposomes were not monodisperse, but had substantially reduced dispersity in comparison to extruded liposomes. In addition, the PDI remained stable after 24 h storage in 4°C (Fig. 6).

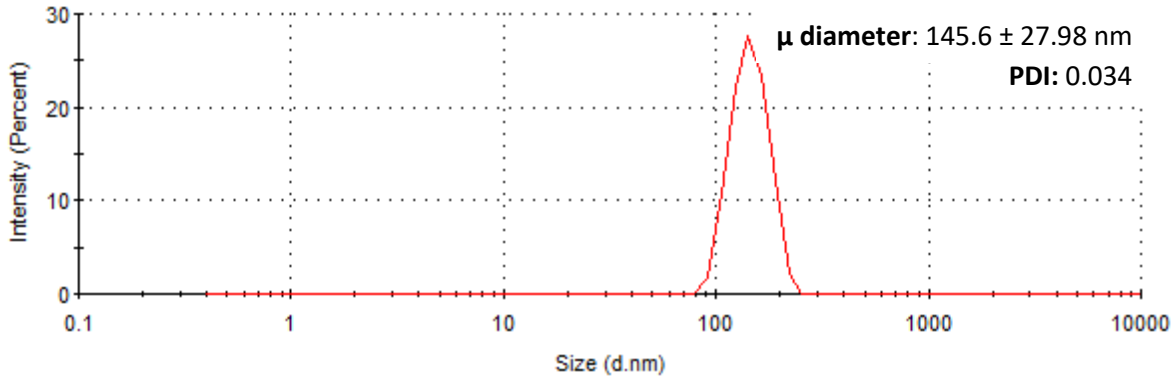

Figure 4. Extruded PS liposomes were analyzed by dynamic light scattering. A monodisperse liposome solution was observed.

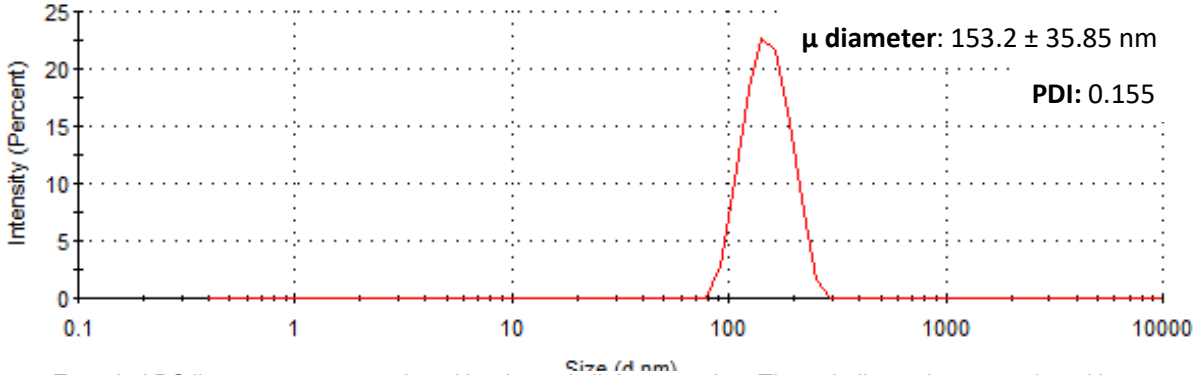

Figure 5. Extruded PC liposomes were analyzed by dynamic light scattering. The polydispersity was reduced in comparison with the PS liposomes.

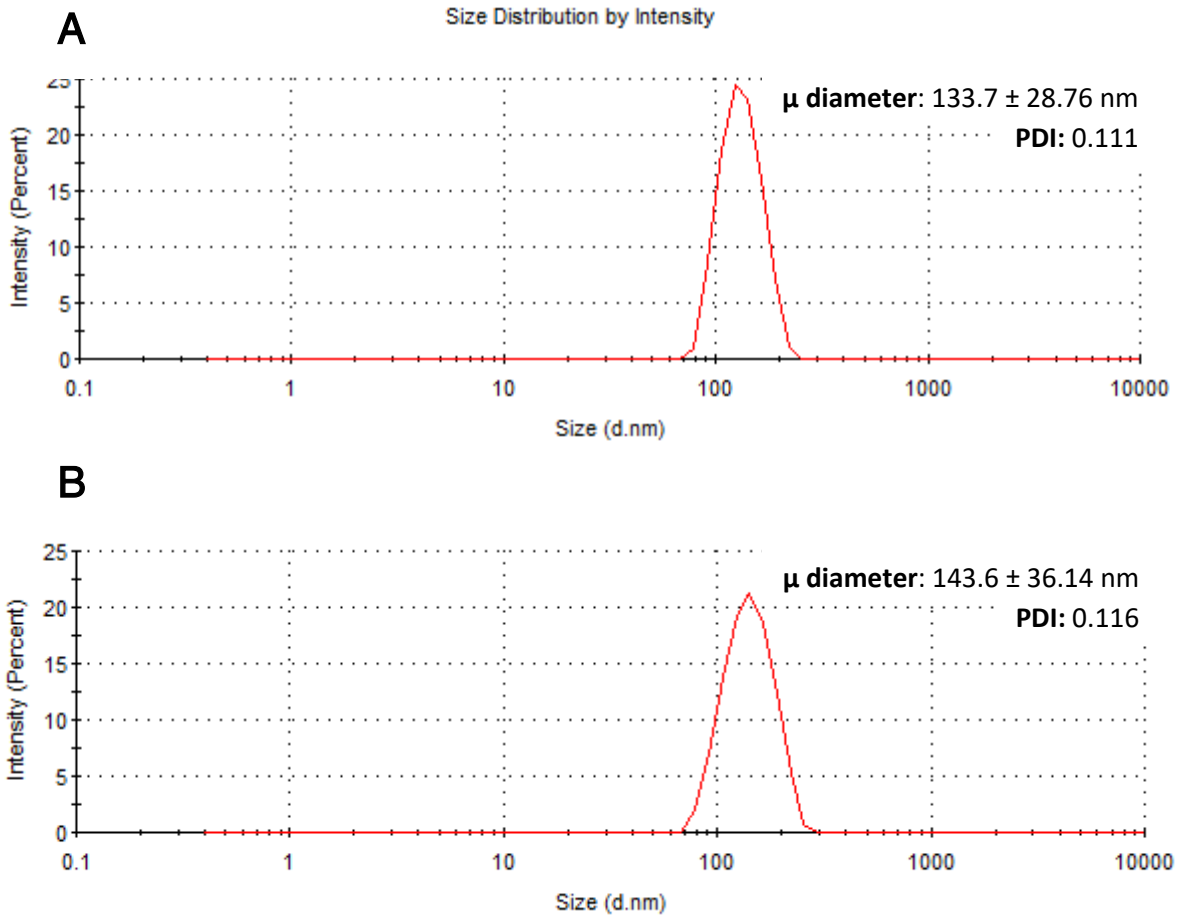

Figure 6. Extruded PC liposomes were assessed for stability by dynamic light scattering. **A** shows the mean diameter and PDI at the 1 hr timepoint whereas **B** shows the mean diameter and PDI at the 24 hr timepoint.

3.2 Immunization *in vivo* and Future Directions

Mice were immunized for six weeks with injections of liposomes occurring biweekly. Vaccination with both liposomal formulations elicited IgM antibody production against PC. PS was observed to stimulate an IgM response more rapidly than PC liposomes, with an increase of IgM titers at week 4. Both treatment groups produced the greatest IgM response, up to 3-fold, at week 6 compared to pre-treatment levels. Interestingly, IgG titers were undetected in these mice (data not shown), indicating that class-switching did not occur. These initial promising results call for investigation of these liposomes in atherosclerotic mice such as $Apoe^{-/-}$ or $Ldlr^{-/-}$ that are fed a Western diet to investigate both IgM production and class-switching. Further, liposomes with lyso-PC, the oxidized form of PC may prove to stimulate production of IgM antibodies that can sequester oxLDLs in mice models of atherosclerosis. In addition, if class-switching is observed, encapsulation of AID inhibitors such as valproic acid may be useful to restrict antibody production to the atheroprotective IgM.

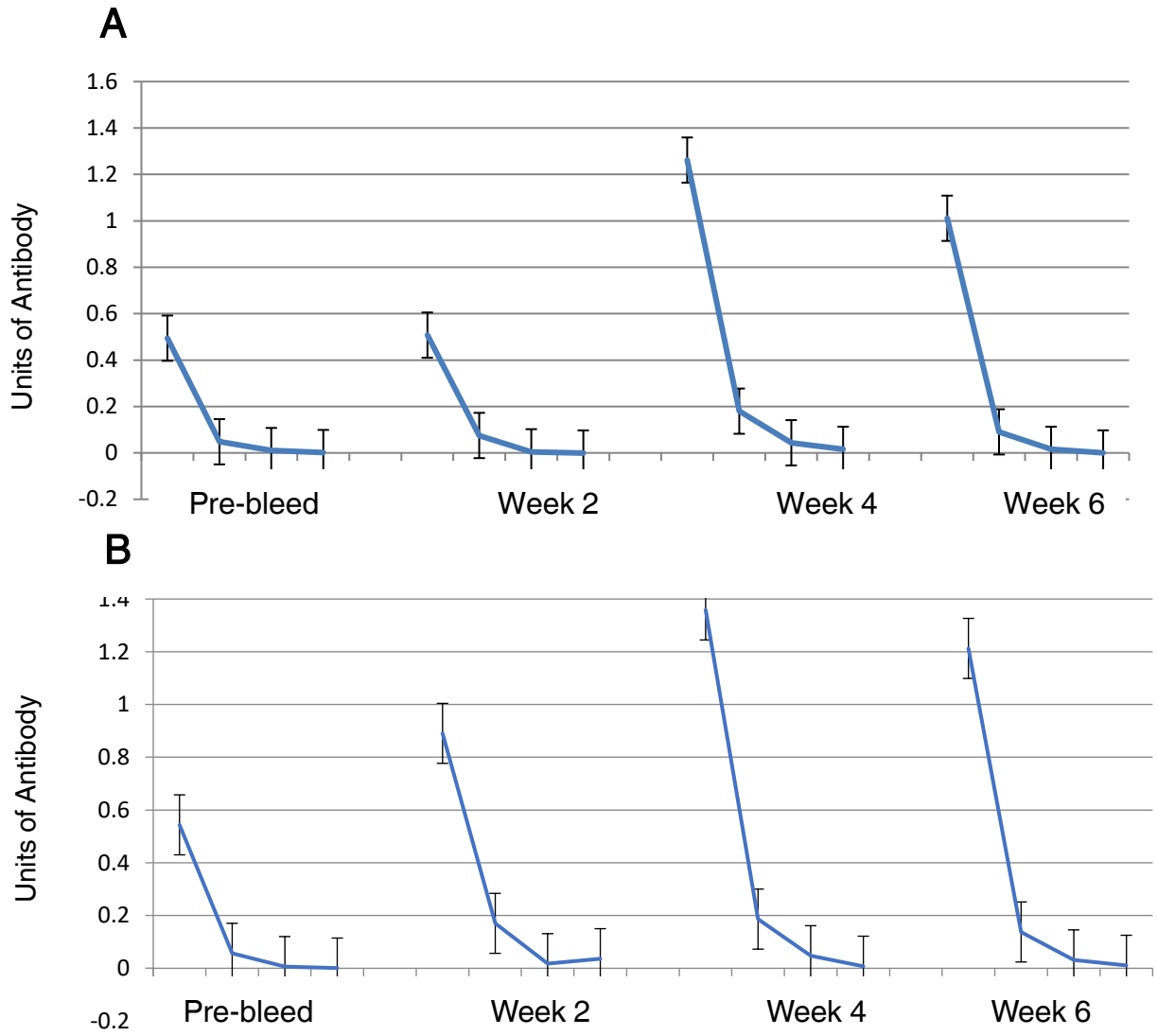

Figure 7. Mice were immunized with liposomes biweekly for 6 weeks. Each point for each week represents a serial dilution of the serum (1:30, 1:300, 1:3000, and 1:30000). A) Immunization with PC liposomes were carried out in two mice. B) Immunization with PS liposomes were carried out in 2 mice.

References

1. WHO. Global status report on noncommunicable diseases 2014. *World Health* 176 (2014). doi:ISBN 9789241564854

2. Bloom, D. E. *et al.* The Global Economic Burden of Noncommunicable Diseases. *World Econ. Forum* 1–46 (2011). doi:10.1192/bjp.184.5.393

3. World Health Organisation. Global Atlas on cardiovascular disease prevention and control. *Geneva* (2011). doi:NLM classification: WG 120

4. Chatzizisis, Y. S. *et al.* Role of Endothelial Shear Stress in the Natural History of Coronary Atherosclerosis and Vascular Remodeling. *J. Am. Coll. Cardiol.* **49,** 2379–2393 (2007).

5. Cunningham, K. S. & Gotlieb, A. I. The role of shear stress in the pathogenesis of atherosclerosis. *Lab. Investig.* **85,** 9–23 (2004).

6. National Cholesterol Education Program (NCEP) Expert Panel on Detection, Evaluation, and T. of H. B. C. in A. (Adult T. P. I. Third Report of the National Cholesterol Education Program (NCEP) Expert Panel on Detection, Evaluation, and Treatment of High Blood Cholesterol in Adults (Adult Treatment Panel III) final report. *Circulation* **106,** 3143–421 (2002).

7. Nelson, D. & Cox, M. *Lehninger Principles of Biochemistry*. (Freeman, W. H. & Company, 2008).

8. Hevonoja, T., Pentikäinen, M. O., Hyvönen, M. T., Kovanen, P. T. & Ala-Korpela, M. Structure of low density lipoprotein (LDL) particles: Basis for understanding molecular changes in modified LDL. *Biochim. Biophys. Acta - Mol. Cell Biol. Lipids* **1488,** 189–210 (2000).

9. Gent, J. & Braakman, I. Low-density lipoprotein receptor structure and folding. *Cell. Mol. Life Sci.* **61,** 2461–2470 (2004).

10. He, G. *et al.* ARH Is a Modular Adaptor Protein That Interacts with the LDL Receptor, Clathrin, and AP-2. *J. Biol. Chem.* **277,** 44044–44049 (2002).

11. Rudenko, G. Structure of the LDL Receptor Extracellular Domain at Endosomal pH. *Science (80-.).* **298,** 2353–2358 (2002).

12. Zhang, D.-W. *et al.* Binding of Proprotein Convertase Subtilisin/Kexin Type 9 to Epidermal Growth Factor-like Repeat A of Low Density Lipoprotein Receptor Decreases Receptor Recycling and Increases Degradation. *J. Biol. Chem.* **282,** 18602–18612 (2007).

13. Parthasarathy, S., Raghavamenon, A., Garelnabi, M. O. & Santanam, N. in 403–417

(2010). doi:10.1007/978-1-60327-029-8_24

14. Haberland, M. E., Fogelman, A. M. & Edwards, P. A. Specificity of receptor-mediated recognition of malondialdehyde-modified low density lipoproteins. *Proc. Natl. Acad. Sci. U. S. A.* **79,** 1712–6 (1982).

15. Levitan, I., Volkov, S. & Subbaiah, P. V. Oxidized LDL: Diversity, Patterns of Recognition, and Pathophysiology. *Antioxid. Redox Signal.* **13,** 39–75 (2010).

16. Haberland, M. E., Olch, C. L. & Folgelman, A. M. Role of lysines in mediating interaction of modified low density lipoproteins with the scavenger receptor of human monocyte macrophages. *J. Biol. Chem.* **259,** 11305–11 (1984).

17. Freeman, M. *et al.* Expression of type I and type II bovine scavenger receptors in Chinese hamster ovary cells: lipid droplet accumulation and nonreciprocal cross competition by acetylated and oxidized low density lipoprotein. *Proc. Natl. Acad. Sci. U. S. A.* **88,** 4931–5 (1991).

18. Podrez, E. A., Hoppe, G., O'Neil, J. & Hoff, H. F. Phospholipids in oxidized LDL not adducted to apoB are recognized by the CD36 scavenger receptor. *Free Radic. Biol. Med.* **34,** 356–364 (2003).

19. Podrez, E. A. Identification of a Novel Family of Oxidized Phospholipids That Serve as Ligands for the Macrophage Scavenger Receptor CD36. *J. Biol. Chem.* **277,** 38503–38516 (2002).

20. Kakutani, M., Ueda, M., Naruko, T., Masaki, T. & Sawamura, T. Accumulation of LOX-1 Ligand in Plasma and Atherosclerotic Lesions of Watanabe Heritable Hyperlipidemic Rabbits: Identification by a Novel Enzyme Immunoassay. *Biochem. Biophys. Res. Commun.* **282,** 180–185 (2001).

21. Nickel, T. *et al.* oxLDL uptake by dendritic cells induces upregulation of scavenger-receptors, maturation and differentiation. *Atherosclerosis* **205,** 442–450 (2009).

22. Harshyne, L. A., Zimmer, M. I., Watkins, S. C. & Barratt-Boyes, S. M. A Role for Class A Scavenger Receptor in Dendritic Cell Nibbling from Live Cells. *J. Immunol.* **170,** 2302–2309 (2003).

23. Hansson, G. K. & Hermansson, A. The immune system in atherosclerosis. *Nat. Immunol.* **12,** 204–212 (2011).

24. Okoye, I. S. & Wilson, M. S. CD4+ T helper 2 cells - microbial triggers, differentiation requirements and effector functions. *Immunology* **134,** 368–377 (2011).

25. Daugherty, A. IL-5 links adaptive and natural immunity in reducing atherosclerotic disease. *J. Clin. Invest.* **114,** 317–319 (2004).

26. Lewis, M. J. *et al.* Immunoglobulin M Is Required for Protection Against Atherosclerosis in Low-Density Lipoprotein Receptor-Deficient Mice. *Circulation* **120,** 417–426 (2009).

27. Cesena, F. H. Y. *et al.* Immune-modulation by polyclonal IgM treatment reduces atherosclerosis in hypercholesterolemic apoE–/– mice. *Atherosclerosis* **220,** 59–65 (2012).

28. Quartier, P., Potter, P., Ehrenstein, M., Walport, M. & Botto, M. Predominant role of IgM-dependent activation of the classical pathway in the clearance of dying cells by murine bone marrow-derived macrophagesin vitro. *Eur. J. Immunol.* **35,** 252–260 (2005).

29. Kuwahara, K. *et al.* Cross-linking of B cell antigen receptor-related structure of pre-B cell lines induces tyrosine phosphorylation of p85 and p110 subunits and activation of phosphatidylinositol 3-kinase. *Int. Immunol.* **8,** 1273–85 (1996).

30. Murphy, K. & Weaver, C. *Janeway's Immunobiology: Ninth Edition*. (2016).

31. Ravandi, A. *et al.* Relationship of IgG and IgM autoantibodies and immune complexes to oxidized LDL with markers of oxidation and inflammation and cardiovascular events: results from the EPIC-Norfolk Study. *J. Lipid Res.* **52,** 1829–1836 (2011).

32. Lopes-Virella, M. F. & Virella, G. Pathogenic Role of Modified LDL Antibodies and Immune Complexes in Atherosclerosis. *J. Atheroscler. Thromb.* **20,** 743–754 (2013).

33. Shaw, P. X. *et al.* Natural antibodies with the T15 idiotype may act in atherosclerosis, apoptotic clearance, and protective immunity. *J. Clin. Invest.* **105,** 1731–1740 (2000).

34. Binder, C. J. *et al.* Pneumococcal vaccination decreases atherosclerotic lesion formation: molecular mimicry between Streptococcus pneumoniae and oxidized LDL. *Nat. Med.* **9,** 736–743 (2003).

35. Watson, D. S., Endsley, A. N. & Huang, L. Design considerations for liposomal vaccines: Influence of formulation parameters on antibody and cell-mediated immune responses to liposome associated antigens. *Vaccine* **30,** 2256–2272 (2012).

36. Torchilin, V. & Weissig, V. *Liposomes: A Practical Approach (Practical Approach Series)*. (Oxford University Press, 2003).

37. Olson, F., Hunt, C. A., Szoka, F. C., Vail, W. J. & Papahadjopoulos, D. Preparation of liposomes of defined size distribution by extrusion through polycarbonate membranes. *Biochim. Biophys. Acta - Biomembr.* **557,** 9–23 (1979).

38. Bachmann, M. F. & Jennings, G. T. Vaccine delivery: a matter of size, geometry, kinetics and molecular patterns. *Nat. Rev. Immunol.* **10,** 787–796 (2010).

39. Moon, J. J. *et al.* Interbilayer-crosslinked multilamellar vesicles as synthetic vaccines for potent humoral and cellular immune responses. *Nat. Mater.* **10,** 243–251 (2011).

40. Kraaijeveld, C. A. *et al.* The effect of liposomal charge on the neutralizing antibody response against inactivated encephalomyocarditis and Semliki Forest viruses. *Clin Exp Immunol* **56,** 509–514 (1984).

41. Nakanishi, T. *et al.* Positively charged liposome functions as an efficient immunoadjuvant in inducing cell-mediated immune response to soluble proteins. *J. Control. Release* **61,** 233–240 (1999).

42. Badiee, A. *et al.* The role of liposome charge on immune response generated in BALB/c mice immunized with recombinant major surface glycoprotein of Leishmania (rgp63). *Exp. Parasitol.* **121,** 362–369 (2009).

43. Bakouche, O. & Gerlier, D. Enhancement of immunogenicity of tumour virus antigen by liposomes: the effect of lipid composition. *Immunology* **58,** 507–13 (1986).

44. Allison, A. C. & Gregoriadis, G. Liposomes as immunological adjuvants. *Nature* **252,** 252 (1974).

45. Morrissey, J. H. Summary of Methods to Prepare Lipid Vesicles. *Methods Enzymol.* 1–3 (2005).

46. Kučerka, N., Nieh, M.-P. & Katsaras, J. Fluid phase lipid areas and bilayer thicknesses of commonly used phosphatidylcholines as a function of temperature. *Biochim. Biophys. Acta - Biomembr.* **1808,** 2761–2771 (2011).

47. Morrissey, J. H. Morrissey Lab Protocol for Preparing Phospholipid Vesicles by Extrusion. *Methods Enzymol.* 1–3 (2005).

48. Cabral, E. C. M., Zollner, R. L. & Santana, M. H. A. Preparation and characterization of liposomes entrapping allergenic proteins. *Brazilian J. Chem. Eng.* **21,** 137–146 (2004).

49. Instruments, M. Inform White Paper Dynamic Light Scattering. *Malvern Guid.* 1–6 (2011).

50. Jeon, H. & Blacklow, S. C. STRUCTURE AND PHYSIOLOGIC FUNCTION OF THE LOW-DENSITY LIPOPROTEIN RECEPTOR. *Annu. Rev. Biochem.* **74,** 535–562 (2005).